Mechanisms of Translation in Cellular Dynamics and Molecular Regulation of Advanced Prostate Cancer

Alexandre A. Germanos

A dissertation

submitted in partial fulfillment of the

requirements for the degree of

Doctor of Philosophy

University of Washington

2023

Reading Committee:

Andrew Hsieh, Chair

Steve Hahn

Manu Setty

Program Authorized to Offer Degree:

Molecular and Cellular Biology

University of Washington

Abstract

Mechanisms of Translation in Cellular Dynamics and Molecular Regulation of Advanced Prostate Cancer

Alexandre A. Germanos

Chair of the Supervisory Committee:
Andrew C. Hsieh, Associate Professor
Human Biology, Fred Hutch Cancer Center

Prostate cancer is one of the most common cancers in men, and advanced prostate cancer is largely incurable and lethal. Mainstream treatment options for advanced prostate cancer all target the androgen hormone signaling pathway. The androgen receptor (AR) is a ligand-activated nuclear receptor that mediates widespread transcriptional changes in response to hormone signaling. AR-low prostate cancer is a rising concern as this subtype is incurable and lethal. Understanding how cellular populations respond to hormone independence can help us define essential characteristics of AR-low proliferation/survival. By scRNAseq of mouse prostates, we find that an intermediate epithelial cell type expands in cancer and AR loss. This cell state is castration resistant and has multiple potential cellular origins which create a highly heterogeneous epithelial compartment. Cellular subsets in human metastatic cancers exhibit striking similarities to these intermediate cells, suggesting a conserved role in mediating cancer aggressiveness and treatment resistance. We also find a highly pro-tumorigenic immune environment, likely recruited via a signaling cascade involving epithelial cells and tumor-associated macrophages. In addition, we characterize the dependence of AR-low castration-resistant prostate cancer (CRPC) on high translation initiation and find that inhibiting eIF4F function results in cell cycle arrest and apoptosis. To investigate molecular mechanisms of translation regulation in this system, we examined transcripts upregulated by eIF4F activity in AR-low mouse prostates. We find a

guanine-rich translational element (GRTE) enriched in the 5’ UTRs of these mRNAs. We test the role of the GRTE in regulating translation of the candidate gene KFL5 and find it is required to maintain high eIF4F-dependent translation. We also find a similar G-rich functional element in 5’ UTRs of mRNAs translationally regulated by an HRAS oncogenic variant and eIF2B5 in murine skin cancer. We then confirm that the GRTE is functional in human cells and conduct a genome-wide analysis to characterize its conservation. Finally, we generate stable reporter cell lines to facilitate future high-throughput experiments.

Table of Contents

List of Figures

Acknowledgments

I have many people to thank for helping me get to this point in my life and career. To start at the beginning of my journey, I have to thank the people who fostered my interest in research and biology so thoroughly that I've known my career path since before I could vote. Thank you to Phil Allen, who taught me freshman biology in high school and kickstarted my love of genetics then and there. Thank you to Dr. Matthew Hardwick, who was kind enough to provide me with my first lab experience as a high schooler and whose lab environment I still remember for its cheerfulness and energy. Thank you to Dr. Bassem Haddad for welcoming me into his lab, for his kind mentorship, and for going above and beyond by giving me the opportunity to earn my first authorship on a scientific paper. And of course, special thanks to Dr. Dan Vernon, who was my undergraduate advisor and mentored me through my first independent research project, my undergraduate degree, and the writing of a (much shorter than this one) thesis. I would not be here without all of these people sharing their love of biology with me and encouraging me to continue on this path.

Of course, I must thank my PhD mentor Dr. Andrew Hsieh. I joined Andrew's lab during a challenging time for me, and it took me some time to fully embrace his style and his research. Nevertheless, Andrew did his utmost to give me projects that fit my interests and would challenge me in all the right ways. He took a chance on a wet lab scientist who wanted to learn how to code by giving me the opportunity to analyze a pilot single-cell RNAseq dataset. Four years later, I have published a first-author paper entirely based on computational analysis. Andrew is an exceedingly careful scientist and repeatedly taught me the value of organization, proper controls, and working in parallel. He also consistently emphasized the importance of collaborative science and helped me work with many wonderful scientists during my time in his lab. Finally, I have greatly enjoyed building a closer working relationship with him and becoming a more effective mentor-mentee pair. His willingness to evolve alongside me and match the style of guidance I needed was essential to everything I did during my PhD, and I'm deeply thankful for his commitment to progressing my research and my career.

I also need to thank the members of the Hsieh lab past and present for creating a wonderful working environment. Yuzhen Liu, Jessie Horn, Yiting Lim, Sujata Jana, Samantha Schuster, Bill Hardin, and Sonali Arora all welcomed me with open arms when I first joined the lab and helped me learn the ropes. Later additions to the team including Yeon Soo Kim, Cindy Wladyka, Rashmi Mishra, Patrick Hoang, Steve Blinka, Pushpa Itagi, and Kristi Schurman only added more enthusiasm to our lab environment. Thank you all for helping, listening, socializing, and celebrating milestones together over the past 5 years.

I am extremely grateful to all my mentors and collaborators who have helped shape me into the scientist I am today, and who have helped drive my projects forward. Thank you to my committee members Drs. Christine Queitsch, Steve Hahn, Rasi Subramaniam, Raphael Gottardo, and Manu Setty for advising me since the very beginning of my thesis work. Your suggestions and comments have helped me tremendously in thinking critically about science and how best to approach my projects. Thank you also to members of the Sowalsky, Ghajar, Beronja, Gottardo, Setty, Subramaniam, Huang, and Rickman labs for the extremely enjoyable collaborations we shared. It has been a joyful experience to perform such collaborative science with them, and I owe many aspects of my research to their expertise and willingness to take time out of their own projects to contribute to mine.

I also want to thank all the friends who have made my life outside the lab so much fun over the course of my PhD and before. Thank you to my friends in MCB for taking this journey with me, talking about science when we needed to vent, and doing so many other things when we didn't want to think about lab. Thanks to Jeet Patel and Samantha Schuster for being great friends and roommates, for organizing game nights, for making dinner or going out together, and for helping me stay sane during the pandemic lockdowns. Thanks to Amy Spens, Vanessa Montoya, Hannah Lewis, Ami Yamamoto, Andrew Smith, Caelan Radford, and the rest of the 2017 cohort for providing an instant community and a source of humor, commiseration, and motivation from the very start. Thank you to other MCB students including Cara Chao, Jessie Kulsuptrakul, Sam Hart, Ricky Padilla Del Valle, Lews Caro, Terry Hafer, Ellen Paatela, Violet Sorrentino, and so many others for playing volleyball, frisbee, and DnD and helping me keep some balance between lab and life. Thank you to the Just Saiyan frisbee team, whose infectious energy and happiness helped see me through a lot of tough times over the past 7 years. Traveling to tournaments with this amazing group of people has created some of my happiest (and sometimes fuzziest) memories. Thank you to the D^2 suite: Jack Armitage, Jessica Van Horne, Hannah Seger, Marci Parra, and Adrienne Beebe for making life during and after college so much more fun and interesting. And special thanks to Tristan Henry for being my oldest friend and not letting distance get in the way of friendship. We've now lived on opposite ends of the world for more time than we lived in the same city, and yet it's always a joy to see each other whenever we are able.

Finally, I need to thank my family for supporting me from the beginning. Thank you to my parents, who encouraged me to be curious by trying to answer every question I ever had as a child. I vividly remember asking my father how helicopters work on the way to school one morning. I do not remember the answer, but I remember that there was one, and that was the important part. Thank you to my brother Nicolas, with whom I've shared so much in my life. You are my best friend and one of the best people I know. Thank you to my aunt Carine, who introduced me to the world of research by putting me in contact with Drs. Hardwick and Haddad. Thank you to all my cousins, whom I do not see nearly as often as I would like, but who are all wonderful and loving people.

In short, thank you to all the wonderful people in my life, without whom I would not be who I am today. I love you all immensely.

Dedication

To my mom, who has always been my biggest fan
and my biggest help in everything.

Chapter 1. Introduction

1.1.1 Prostate Cancer: Diversity of Etiology and Hormone Dependence

The prostate is an important male sexual organ responsible for producing key components of the seminal fluid (Frick et al., 1991). Prostate cancer is the most diagnosed and second leading cause of cancer death in men in the US (Siegel et al., 2021). Incidence rates of prostate cancer rose dramatically in the early 1990s mainly due to more widespread use of prostate-specific antigen (PSA) testing to detect asymptomatic disease (Potosky et al., 1995). This partially explains the relatively low lethality of this disease: the 5-year survival rate is 98%, highest of all cancers in 2021. This is also reflected in the gap between diagnosis rate (26% of all male cancers) and death rate (11% of all male cancers) in 2021. Accordingly, prostate cancer is largely lethal in older men with more advanced disease. In fact, prostate cancer is the second most lethal cancer for men aged 60 or older but is outside of the top five most lethal cancers for men under 60 (Siegel et al., 2021).

Additionally, mortality due to prostate cancer has decreased 52% since 1993 thanks to earlier detection and advances in treatment (Etzioni et al., 2008). Mainstream treatment modalities are largely centered around interrupting androgen hormone signaling, a critical pathway for prostate development and homeostasis as well as prostate cancer progression. Androgen hormones influence gene expression programs in male sexual organs via the androgen receptor (AR), a ligand-dependent nuclear transcription factor. Unbound AR resides in the cytoplasm and requires binding by androgen hormones such as testosterone or its more active form dihydrotestosterone (DHT) to localize to the nucleus, where it binds DNA elements dubbed Androgen Response Elements (AREs). These specific binding sites allow the activated AR to enact a host of transcriptional changes in developing and adult tissues (Davey et al., 2016). AR function is essential for prostate cancer growth and survival: inhibition of testosterone production, known as androgen deprivation therapy (ADT) interrupts AR activity and significantly halts cancer progression (Huggins and Hodges, 1941; Grossmann et al., 2013). More recently, drugs directly targeting the AR have come into mainstream use and complemented ADT in the clinic, leading to stronger repression of androgen signaling (de Bono et al., 2011; Schur et al., 2012). These treatments significantly extend patient survival in the context of advanced disease.

However, advanced prostate cancer commonly recurs despite androgen deprivation, and full remission is rare (Beltran et al., 2011). Surprisingly, most recurrent cancers remain androgen-dependent, demonstrating the ability of this disease to overcome ADT and AR inhibitors (ARIs) to maintain robust hormone signaling. Drug-resistant cancer is commonly called castration-resistant prostate cancer (CRPC) and is largely incurable and lethal (Beltran et al., 2011). Genetic and genomic characterization of CRPC samples has revealed multiple mechanisms by which androgen signaling is

maintained. These include AR amplification or overexpression, mutations in its ligand-binding domain, aberrant post-transcriptional AR activation, and intratumor androgen production (Knudsen et al., 2009). However, androgen independent CRPC exists, and constitutes a rising proportion of cases in the past decade, potentially due to evolutionary pressure caused by more effective therapeutic suppression of androgen signaling (Bluemn et al., 2017). While neuroendocrine CRPC (NEPC) is a known variant etiology that resembles other small cell cancers and is androgen independent, the observed increase consists largely of non-NE, non-AR cancer phenotypes also called double-negative prostate cancer (DNPC). These CRPC subtypes are both incurable and poorly understood, highlighting the need for further characterization of the molecular pathways involved in prostate cancer maintenance and progression.

1.2 Cellular Heterogeneity in Healthy and Malignant Prostate

Prostate development and physiology is complex. This organ is composed of a series of glands, or acini, which generate seminal fluid (Frick et al., 1991). Interestingly, the prostate is physiologically distinct in humans compared to other mammals. While the human prostate sports a tubuloalveolar morphology extending from the urethra, mouse prostates are compact and composed of anterior, ventral, dorsal, and lateral lobes. These significant deviations in tissue architecture must invite caution in drawing concrete conclusions about human prostate cancer from mouse models of the disease. In fact, only about 5% of all cancer drugs tested in mice have shown promise in human clinical trials (Hutchinson and Kirk, 2011). Of course, differences in prostate physiology do not fully account for this high failure rate. Most drug trials in mice are conducted on xenografts, where tumors lack the proper cellular and molecular context of their original tissue and are artificially homogeneous across samples compared to the diversity of human disease. Other factors such as genomic differences lead to significant limitations of mouse models overall (Valkenburg and Pienta, 2015). However, many of the most effective tools at our disposal to study the cellular and molecular basis of prostate cancer, from genetically engineered models to lineage tracing methods, are naturally unavailable in human contexts. While some experiments may be conducted in human cells via tissue culture methods, including three-dimensional models such as organoids and spheroids, a full view of prostate development, cellular composition, and homeostasis is impossible outside model organisms.

Lineage tracing experiments are a primary example of highly useful methods that are only feasible in model organisms. Lineage tracing studies in the mouse prostate have precisely outlined the cellular origins of each epithelial cell type present in the prostate. The principal prostate cell types are basal cells, which compose the basement membrane of prostate acini and exhibit stemlike features, and luminal cells, which line these acini and perform secretory functions (Oliveira et al., 2016). Recent studies have shown that basal cells are not progenitors of luminal cells, but that they each represent

distinct self-renewing lineages (Choi et al., 2012). Other less-abundant epithelial lineages exist and contribute to prostate homeostasis, such as neuroendocrine cells and rare “luminal progenitors,” so called because they express luminal biomarkers and high stemness rather than because they are progenitors to canonical luminal cells (Xin et al., 2005; Kwon et al., 2016; Kwon et al., 2020). These findings are of particular relevance in the context of cancer, as the question of which prostatic cell types are responsible for tumor initiation is a long-standing one in the field (Shen and Abate-Shen, 2010). For instance, while common consensus holds that luminal cells are the main agents of tumorigenesis, there is evidence in mice that basal cells can initiate cancer, but only by first transdifferentiating into luminal cells (Goldstein et al., 2010; Choi et al., 2012; Lu et al., 2013). Again, due to experimental limitations, this phenomenon has not been shown in human prostate cancer. Neuroendocrine cells are also implicated both in rare AR-low prostate cancers similar to other small-cell tumors and in promoting adenocarcinoma proliferation (Salido et al., 2000; Patrawala et al., 2006; Simon et al., 2009; Puca et al., 2019). Finally, luminal progenitor cells are castration-resistant and participate in tissue regeneration post androgen deprivation, making them a potential source of treatment resistance in advanced CRPC (Karthaus et al., 2020; Mevel et al., 2020; Guo et al., 2020; Kwon et al., 2021). Overall, the prostate is a morphologically complex organ that exhibits significant cellular plasticity in both normal and cancer contexts. While mouse models remain the most tractable organismal systems to study this disease, care must be taken not to over-interpret how findings might translate to the clinic.

1.3 Prostate Cancer Responds Poorly to Immunotherapy Approaches

Immune surveillance is a major mechanism against malignant transformation and growth (Lv et al., 2020). This is generally mediated via recognition of neoantigens on cancer cells by CD8+ T cells, which infiltrate tumors and perform cytotoxic functions to help clear out malignant cells (Pages et al., 2005; Galon et al., 2006). There is growing evidence that high tumor mutational burden increases neoantigen presentation and therefore antitumor immune response (Snyder et al., 2014; Rizvi et al., 2015; McGranahan et al., 2016). However, cancer frequently evades the immune response by inhibiting or co-opting immune signaling (Gajewski et al., 2013). This can occur via inhibiting CD8+ cytotoxic T cells through direct signaling towards receptors that mediate exhaustion signals or by recruitment of regulatory CD4+ T cells which restrict CD8+ T cell function (Mortarini et al., 2003; Gajewski, 2007). In these cases, inhibiting the immune checkpoint receptors CTLA4 and PDCD1 has proven an effective form of tumor immunotherapy by reactivating CD8+ cytotoxic activity (Hodi et al., 2010; Zou et al., 2016). More recently, the advent of chimeric antigen receptor T (CAR-T) cells has revolutionized the cancer immunotherapy field (Lin et al., 2021). CAR-T cells are T cells isolated from patients and engineered to target cancer-specific neoantigens, stimulating antitumor immunity without generating

autoimmune side effects (Labanieh et al., 2018). Overall, targeting cytotoxic T cell activity has proven a highly successful therapeutic approach to several cancers.

However, tumor immune signaling is not limited to inhibiting CD8+ T cell function. Cancers also express chemokines and cytokines that can recruit immunosuppressive cells to build a favorable tumor microenvironment (TME) (Mukaida et al., 2014; Ozga et al., 2021). These cell types include both myeloid cells such as tumor-associated macrophages (TAMs) and myeloid-derived suppressor cells (MDSCs) and lymphoid cells in the form of regulatory T cells (Treg) (Coussens et al., 2013; Hua and Bergers, 2019; Ozga et al., 2021). These cells create a pro-tumorigenic microenvironment around the tumor, protecting it from acute anticancer immune responses. Interestingly, tumors exhibit highly heterogeneous levels of CD8+ T cell infiltration, which is partly due to differences in tumor-secreted chemokines (Harlin et al., 2009; Gajewski et al., 2013; Olga et al., 2021). Thus, the recruitment of immunosuppressive immune cells to the TME may significantly contribute to protecting cancer cells from antitumor immune responses.

Prostate cancer responds poorly to immunotherapy. Checkpoint inhibitors have had limited effects in clinical trials, leading this disease to be considered an “immune cold” cancer (Cham et al., 2020; Stultz and Fong, 2021). Even the most successful immunotherapy approach against prostate cancer only shows a 22% decrease in mortality risk, and no improvement in halting disease progression, demonstrating the difficulty of decreasing prostate tumor burden via immunotherapy (Kantoff et al., 2010). Additionally, the prostate cancer TME contains multiple immunosuppressive cell types including MDSCs (Garcia et al., 2014). This may cause exhaustion or exclusion of CD8+ cytotoxic T cells, thus inhibiting antitumor immunity. Strikingly, AR loss in CRPC models increases MDSC abundance, implying AR independent prostate cancer may more strongly resist immunotherapy approaches (Lopez-Bujanda et al., 2021). More complete characterization of the prostate immune landscape and its changes in the context of tumorigenesis and hormone loss may enable further advances in designing effective immunotherapies for this disease.

1.4 Translation Initiation: Functions in Disease

Changes in genomic DNA sequence or mRNA expression have been deeply studied in normal and disease contexts. It is commonly accepted that these processes can drive tumorigenesis. However, protein synthesis was assumed to be automatic and unregulated until relatively recently, and as a result its roles in cancer have not been studied extensively (Fabbri et al., 2021). However, recent technological advances have enabled much closer examination of protein synthesis processes (Ingolia et al., 2009; Floor and Doudna, 2016). In fact, translation is highly heterogeneous and can vary between cell and tissue types, leading to context-specific regulation (Buszczak et al., 2014). Each

phase of translation is a tightly regulated process, from initiation to elongation, termination, and recycling of ribosomes and other factors (Song et al., 2021). mRNA sequence can act in *cis* to modulate translation levels via regulatory motifs in untranslated regions (UTRs) or codon usage in the coding sequence (CDS) (Schuster et al., 2019; Liu et al., 2021). In addition, many external factors including RNA-binding proteins (RBPs) or noncoding RNAs (ncRNAs) act in *trans* to regulate ribosome binding, scanning, elongation, and recycling (Djuranovic et al., 2012; Meijer et al., 2013; Dassi, 2017; Hentze et al., 2018). Recent studies have even found that translation machinery can impact translation rates, in the form of tRNA abundance or heterogeneous ribosomes (Shi et al., 2017; Torrent et al., 2018). In short, translation regulation is multifaceted, complex, and can drastically impacts gene expression, often causing protein levels to deviate significantly from mRNA levels (Franks et al., 2017).

Translation initiation is a particularly complex process as it involves ribosomal recruitment, loading and scanning towards the translation start site (Ho et al., 2021). Initiation is canonically mediated by the eIF4F translation initiation complex, which consists of the 5' cap-binding subunit eIF4E, the scaffolding subunit eIF4G, and the helicase eIF4A (Silvera et al., 2010). The eIF4F complex provides a platform for ribosomal loading and helicase activity to unwind structured mRNA and allow scanning (Jackson et al., 2010). This complex is itself heavily regulated, as eIF4E can be phosphorylated to enhance its activity and eIF4E binding proteins (4EBPs) compete with eIF4G to prevent complex formation (Uttam et al., 2018; Hao et al., 2020). 4EBP1 is itself regulated by mTORC1, linking translation initiation to a major oncogenic pathway (Peter et al., 2015). mRNA 5' UTR regions are also a major source of regulation and can provide binding sites for RBPs as well as complex RNA structures (Schuster et al., 2019). Given this highly granular, multifaceted regulation of initiation rates, it is unsurprising that translation initiation is implicated in multiple cancer contexts (Biffo et al., 2018). In breast cancer, MYC oncogenic activation triggers increased translation initiation of SF3A3 via an eIF3-dependent mechanism and modulates tumor stemness and recurrence phenotypes (Ciesla et al., 2021). A mouse model of melanoma showed HRAS-dependent increases in translation initiation increase proliferation (Cai et al., 2020). Finally, multiple studies implicate eIF4F function in prostate cancer. Aberrant mTOR signaling regulates eIF4F via 4EBP1 phosphorylation and promotes prostate cancer progression (Hsieh et al., 2012; Hsieh et al., 2015). Interestingly, a separate mechanism also associates eIF4F hyperactivity with increased proliferation of AR-low disease. Indeed, AR directly activates 4EBP1 transcription, androgen loss results in increased eIF4F complex assembly and function, and hyperproliferation can be rescued by re-expression of 4EBP1 (Liu et al., 2019). The finding that translation initiation is crucial for AR-low CRPC progression offers a new avenue for therapeutic approaches against this cancer subtype, but we still lack a full understanding of how proliferation and other processes are mediated by eIF4F. A more complete mechanistic picture of the role of initiation would likely benefit patients with this currently incurable disease.

In this dissertation I will address two main questions:

1. **How do cellular populations in mouse prostates respond to cancer initiation and hormone-independent progression?**

In Chapter 2, I describe a single-cell RNA sequencing atlas of mouse prostates. This atlas includes WT mice as well as a prostate cancer model based on prostate-specific deletion of *Pten* under normal and castrated conditions, as well as a castrated *Pten;4ebp1*^{M} double mutant with inhibited translation initiation activity. I detail the changes in cellular populations under these conditions, finding epithelial and immune cell states that expand in cancer, mediate castration resistance and AR-low proliferation, and suppress antitumor immune responses, and characterize the role of translation rates in this system. Finally, we present our dataset as a resource to the field via an interactive website.

2. **How does eIF4F hyperactivity in AR-low prostate cancer regulate a subset of mRNAs to maintain high proliferation?**

In Chapter 3, I examine the molecular mechanisms of translation regulation in AR-low prostate cancer. I discover a novel sequence element in the 5' UTRs of mRNAs affected by eIF4F hyperactivity and use a series of reporter assays to establish its functionality in several candidate genes. I also evaluate the conservation of this motif in candidate genes and genome-wide, investigate possible mechanisms of action, and generate a stable reporter system for future high-throughput experiments.

Chapter 2. Defining cellular population dynamics at single-cell resolution during prostate cancer progression

This work was originally published in *ELIFE*. Germanos AA, Arora S, Zheng Y, Goddard ET, Coleman IM, Ku AT, Wilkinson S, Song H, Brady NJ, Amezquita RA, Zager M, Long A, Yang YC, Bielas JH, Gottardo R, Rickman DS, Huang FW, Ghajar CM, Nelson PS, Sowalsky AG, Setty M, Hsieh AC. 2022. Defining cellular population dynamics at single-cell resolution during prostate cancer progression. *Elife* **11**. doi:10.7554/elife.79076

2.1 Abstract

Advanced prostate malignancies are a leading cause of cancer-related deaths in men, in large part due to our incomplete understanding of cellular drivers of disease progression. We investigate prostate cancer cell dynamics at single-cell resolution from disease onset to the development of androgen independence in an in vivo murine model. We observe an expansion of a castration-resistant intermediate luminal cell type that correlates with treatment resistance and poor prognosis in human patients. Moreover, transformed epithelial cells and associated fibroblasts create a microenvironment conducive to pro-tumorigenic immune infiltration, which is partially androgen responsive. Androgen-independent prostate cancer leads to significant diversification of intermediate luminal cell populations characterized by a range of androgen signaling activity, which is inversely correlated with proliferation and mRNA translation. Accordingly, distinct epithelial populations are exquisitely sensitive to translation inhibition, which leads to epithelial cell death, loss of pro-tumorigenic signaling, and decreased tumor heterogeneity. Our findings reveal a complex tumor environment largely dominated by castration-resistant luminal cells and immunosuppressive infiltrates.

2.2 Introduction

Prostate cancer is the most diagnosed malignancy and second leading cause of cancer-related death in men in the United States (Siegel et al., 2021). This is largely due to the development of treatment resistant disease termed castration resistant prostate cancer (CRPC). Historically, CRPC has been considered a singular disease entity. However, this viewpoint has significantly evolved with the advent of next generation sequencing and the characterization of many distinct etiologies (Watson et al., 2015; Bluemn et al., 2017; Labrecque et al., 2019). Intratumoral heterogeneity is also common in prostate cancer, as several studies have highlighted both the complex cellular architecture of the prostate and multiple potential cell-of-origin models (Goldstein et al., 2010; Shen and Abate-Shen, 2010). For instance, while prostate epithelial cells canonically present as either basal cells or highly differentiated luminal cells, a distinct, more stemlike luminal population (*Psca+/Krt4+/Tacstd2+*) that

primarily resides in the proximal prostate has previously been described (Xin et al., 2005; Wang et al., 2006; Korsten et al., 2009; Kwon et al., 2016; Sackmann Sala et al., 2017; McAuley et al., 2019). While the nomenclature for this cell type has varied, most studies have observed a similar set of biomarkers and characteristics, including increased stemlike and inflammatory/immunogenic signatures (Liu et al., 2016). These cells also appear to be castration-resistant; indeed, some studies show canonical prostatic luminal cells may undergo phenotype switching towards a more stemlike *Krt4*+ cell state in castrate conditions, reverting and helping repopulate the prostate during castration and regeneration cycles (Karthaus et al., 2020; Mevel et al., 2020; Guo et al., 2020; Kwon et al., 2021).

This novel cell type was further verified using lineage tracing and single-cell technologies (Liu et al., 2016; Crowley et al., 2020; Joseph et al., 2020; Karthaus et al., 2020; Kwon et al., 2020; Mevel et al., 2020; Guo et al., 2020). *Krt4*+ cells are also found more rarely in the distal prostate, where they localize to invagination tips (Guo et al., 2020). These cell types remain incompletely characterized, including in their origin; some studies point to proximal luminal cells originating from the urethra, and therefore not being prostatic in nature (Joseph et al., 2020). Others recognize the presence of urethral cells but draw a distinction between them and prostatic *Krt4*+ proximal cells (Crowley et al., 2020).

There is evidence that *Krt4* + cells may contribute to tumor initiation in the prostate (Xin et al., 2005; Wang et al., 2006; Korsten et al., 2009; Kwon et al., 2016; Sackmann Sala et al., 2017; Guo et al., 2020). For instance, several studies find these cells enriched in precancerous lesions upon genetic perturbations in murine models (Wang et al., 2006; Korsten et al., 2009). Additionally, proximal cells appear less able to contribute to tumor initiation than those residing in distal prostate lobes (Korsten et al., 2009; Guo et al., 2020). These findings, combined with studies characterizing the role of *Krt4*+ cells in castration and regeneration, suggest they may contribute to treatment resistance in advanced cancer. However, this has yet to be established in CRPC models.

While tumor heterogeneity contributes to treatment resistance, another source of poor clinical outcomes can be found in the consistent lack of response of CRPCs to immunotherapy. Prostate cancer has generally been described as ‘immune-cold’ due to the presence of multiple immunosuppressive cell types (Stultz and Fong, 2021). For example, tumor infiltration by myeloid-derived suppressor cells (MDSCs) has been implicated as an immunosuppressive phenotype (Garcia et al., 2014; Lopez-Bujanda et al., 2021). Metastatic CRPC also responds poorly to immune checkpoint inhibition and other immunotherapies (Cham et al., 2020). This has been confirmed clinically with autologous active cellular immunotherapy which only demonstrated a small (~4 month) improvement in survival in patients (Kantoff et al., 2010). Therefore, characterizing the immune microenvironment in advanced prostate cancer may be crucial to better understand this disease and inform potential therapeutic vulnerabilities or combinatorial strategies.

Here, we have created an atlas of prostate cellular composition and phenotypic evolution through tumor initiation, progression, and hormone independence using a *Pten* loss murine model as an archetype. We observe a dramatic expansion of an intermediate luminal cell type in cancer and link this epithelial population to treatment resistance in multiple human cohorts. We also characterize increased pro-tumorigenic immune cell recruitment and define cell-cell signaling patterns that contribute to lymphoid and myeloid cell expansion. In addition, using a tissue-specific transgenic model, we demonstrate that cell type specific protein synthesis is essential for the maintenance of tumor heterogeneity in both basal and intermediate cells in the context of AR-low prostate cancer. Finally, we make our data available for further study through an interactive portal, with the aim of providing a broad resource for the cancer research community. Together, our findings highlight the cell type-specific and patient relevant features of prostate cancer progression and demonstrate the utility of single-cell technologies to uncover novel cell-specific paradigms of treatment resistance.

2.3 Results

2.3.1 Characterization of WT and Pten$^{fl/fl}$ *ventral prostates at single cell resolution*

To determine the cellular architecture of prostate cancer initiation, we conducted single-cell RNA sequencing (scRNAseq) of the ventral prostates of 6-month-old wild-type (WT) and PB-Cre4;Pten$^{fl/fl}$;ROSA26-rtTA-IRES-eGFP (herein referred to as Pten$^{fl/fl}$, see Methods) prostate cancer mice (Figure 2.3.1A). We chose the ventral lobe because it has been well-characterized throughout prostate cancer progression at a deep molecular level and for the abundance of cellular populations (Hsieh et al., 2012; Hsieh et al., 2015; Liu et al., 2019). In the Pten$^{fl/fl}$ model, exon 5 of the tumor suppressor Pten is deleted within basal and luminal epithelial cells of the prostate and mice uniformly develop prostate cancer (Wang et al., 2003). PTEN is a negative regulator of the oncogenic PI3K-AKT-mTOR signaling pathway, which is deregulated in nearly all advanced prostate cancer patients (Taylor et al., 2010).

Quality control and filtering (read count thresholds and excluding cells with high mitochondrial content) resulted in transcriptomes from 24,079 total cells across five samples. Using SingleR, we identified epithelial, stromal, and immune cell types (Aran et al., 2019; Fig. 2.3.S1A). To confirm that the epithelial cells in the *Pten$^{fl/fl}$* model underwent Cre-mediated recombination, we measured the frequency of *rtTA-eGFP* fusion mRNA in WT and *Pten$^{fl/fl}$* mice. The *rtTA-eGFP* transcript was present in 14.5% of *Pten$^{fl/fl}$* epithelial cells (Fig 2.3.S1B). Given that on average ~1200 genes/cell were detected and ~24,000 genes were identified overall, we expect the average transcript to be found in ~5% of cells in the dataset. Therefore, our finding suggests widespread recombination, and therefore loss of *Pten*,

within the epithelial compartment. Importantly, recombination was not observed in WT mice or non-epithelial cell types (Fig 2.3.S1B).

We further defined the epithelial population in WT mice via signatures and biomarkers obtained from the Strand (Basal, Urethral, and VP), Sawyers (Basal, L1, and L2), and Xin (Sca-1+) groups (Joseph et al., 2020; Karthaus et al., 2020; Liu et al., 2016). We found canonical basal (*Krt5+/Sox4+*) and luminal (*Nkx3-1+/Sbp+*) cells, as well as two distinct clusters expressing luminal progenitor markers (*Psca+/Tactsd2+/Krt4+*) (Fig 2.3.S1C–D). These clusters were mainly distinguished by different basal, L2, and luminal (VP/L1) signature scores. In addition, one cluster clearly expressed previously identified urethral markers *Aqp3* and *Ly6d*, and was negative for other progenitor markers (*Ppp1r1b, Clu;* Fig. 2.3.S1C; Crowley et al., 2020). Accordingly, we designated this cluster as urethral. The other *Krt4+* cluster likely represents progenitor prostatic cells, either from the proximal or distal prostate (Crowley et al., 2020; Guo et al., 2020). Therefore, we refer to this cluster as luminal progenitor hereafter (Fig 2.3.S1D).

We then examined epithelial cell subtypes in $Pten^{fl/fl}$ mice. We identified basal, urethral, and canonical luminal cells, as well as a large cluster of cells similar to WT luminal progenitor cells, characterized by expression of *Krt4/Tacstd2/Ppp1r1b* but not *Psca* (Fig. 2.3.S1E-F). Clustering urethral cells with luminal progenitor and this new $Pten^{fl/fl}$ cluster, we find that the urethral cells cluster apart from the other cell types and express significantly lower levels of prostate luminal or pan-epithelial markers (*Krt8, Krt18, Epcam*) (Fig. 2.3.S1G–H). This supports the hypothesis that we have identified both urethral and prostate cells, and likely indicates a prostatic origin for the $Pten^{fl/fl}$ cluster. We designated *Krt4+/Tacstd2+/Ppp1r1b+* cells in $Pten^{fl/fl}$ mice as 'intermediate' cells (Fig. 2.3.S1E).

2.3.2 Pten *loss generates differentially proliferating populations and a dominance of intermediate luminal cell states from multiple cellular origins*

Next, we sought to determine how the epithelial compartment is remodeled in the context of tumor initiation. We excluded the urethral cluster because it is not prostatic in origin and therefore is less likely to significantly impact cellular dynamics in prostate cancer. We observed a dramatic increase in the proportion of intermediate cells in $Pten^{fl/fl}$ mice compared to luminal progenitor abundance in the WT setting (Fig. 2.3.1B–C). To investigate potential mechanisms of this expansion of the intermediate population, we identified differentially expressed genes (DEG) and performed gene set enrichment analysis (GSEA) on each epithelial subtype, comparing the WT and $Pten^{fl/fl}$ epithelial compartments ($Pten^{fl/fl}$ basal:WT basal, $Pten^{fl/fl}$ intermediate:WT luminal progenitor, $Pten^{fl/fl}$ luminal:WT luminal). We noted enrichment of oncogene and tumor suppressor pathways in the $Pten^{fl/fl}$ mice, including upregulation of AKT and mTOR, which are expected in this model. We also observed

increased *Wnt* signaling and metabolic processes across all epithelial cell types. Interestingly, both epithelial cell migration and proliferation were enriched in most epithelial cells (Fig. 2.3.1D). These findings suggest that intermediate cell expansion could be mediated by increased proliferation of luminal progenitors, or by increased transdifferentiation of other cell types, which has been widely characterized in WT settings (Karthaus et al., 2020; Mevel et al., 2020; Kwon et al., 2021).

To evaluate the possibility of increased proliferation of different epithelial cell types, we used the Cell Cycle Progression (CCP) score, a proliferation gene signature developed and validated in human prostate cancer patients (Cuzick et al., 2011), and generated a composite score (see Materials and methods) in our dataset. Surprisingly, while there was a significant increase in CCP score in basal cells in *Pten*$^{fl/fl}$ mice compared to WT, we observed no significant change in intermediate cells compared to luminal progenitor cells (Fig. 2.3.1E). To further characterize epithelial proliferation, we performed cell cycle scoring, assigning one of three phases (G1, G2/M, or S) to each cell in the dataset, and found a striking split in the basal compartment of *Pten*$^{fl/fl}$ mice, but not WT mice. In *Pten*$^{fl/fl}$ mouse prostates, 18.6% of basal cells were hyper-proliferative, with 99.7% of these cells in a proliferative phase (G2/M or S phases). The rest of the basal compartment only had 52.2% of cells in a G2/M or S phase, lower than WT basal cells (68.5%) (Fig. 2.3.1F, Fig. 2.3.S2A). We also verified that the increase in basal cell CCP score was specifically due to this hyper-proliferative cluster (Fig. 2.3.S2B). One possibility for this differential increase in basal cell proliferation is higher Cre-mediated recombination efficiency in some clusters over others. We analyzed transgene abundance in our basal subclusters and found that in the *Pten*$^{fl/fl}$ mouse, 13.6% (12.0%–15.7%) of hypo-proliferating and 19.6% (19.1%–20.3%) of hyper-proliferating basal cells express the *rtTA-eGFP* transgene. This <1.5-fold difference does not account for the >twofold increase in cycling cells, or the ~threefold increase in CCP score observed between the subclusters. As such, we conclude that *Pten* loss in the murine prostate promotes a dual phenotype in basal cells, with most cells displaying decreased proliferation while a subset becomes hyper-proliferative.

We further characterized the basal subclusters in *Pten*$^{fl/fl}$ mice by performing DEG analysis followed by GSEA. As expected, we observed several cell-cycle-related pathways enriched in the hyper-proliferative cluster. However, the hypo-proliferative basal cluster was enriched for several migration, development, and differentiation signatures (Fig. 2.3.1G). Transdifferentiation of basal cells to luminal cells in the context of malignant transformation has previously been reported in prostate cancer (Goldstein et al., 2010; Choi et al., 2012; Lu et al., 2013; Wang et al., 2013). As such, we hypothesized that the hypo-proliferative basal subcluster might transition into intermediate luminal cells, thus providing one potential mechanism for the expansion of this cell type in the absence of increased proliferation. To verify this, we generated pseudotime trajectories using Monocle3 (Cao et al., 2019),

which confirmed a direct path from hypo-proliferative basal cells to intermediate luminal cells (Fig. 2.3.S2C). We also performed RNA velocity, a technique to visualize differentiation dynamics on a per cell basis (La Manno et al., 2018). This analysis revealed significant movement from hypo-proliferative, but not hyper-proliferative basal cells to intermediate cells (Fig. 2.3.1H). Finally, we used a pseudotime algorithm (Setty et al., 2019) to identify two potential trajectories starting from the hypo-proliferative basal cells and ending either in the hyper-proliferative basal cluster or in the intermediate luminal cell compartment (Fig. 2.3.1I). We generated clusters of genes with similar expression patterns across these pseudotime axes (Fig. 2.3.S2D) and performed GSEA on the clusters. We found that several genes involved in cell fate decisions including *Pdgfb*, *Trp63*, and *Shh* are highly expressed early but rapidly decrease over the trajectories. Conversely, genes implicated in differentiation such as *Notch1* increased over the basal-intermediate path, but not the basal-basal path (Fig. 2.3.1J). This suggests that hypo-proliferating basal cells strongly express development markers associated with cell fate choice, but these genes are not expressed in hyper-proliferative basal cells or intermediate cells. Moreover, intermediate cells express higher levels of differentiation-associated genes than either basal subcluster. Together, these findings support the idea that hypo-proliferative basal cells transdifferentiate into intermediate luminal cells during tumorigenesis, while the basal compartment may be replenished by a hyper-proliferative, non-differentiating population.

Multiple studies have suggested that prostate luminal cells can phenotype switch to intermediate-like states under conditions such as castration (Karthaus et al., 2020; Guo et al., 2020). To verify whether luminal populations may contribute to the intermediate cell state, we plotted the expression of genes canonically expressed in prostate luminal cells and found that while luminal cells did express these genes most strongly, there was overlap with a population of intermediate cells immediately adjacent to the luminal cells in *Pten*$^{fl/fl}$ mice (Fig. 2.3.S2E). This suggests that luminal cells may phenotype switch into an intermediate state and retain some identity markers in the context of *Pten* loss. It is also possible that luminal progenitor cells contribute to the intermediate population, as *Krt4*+ cells within the proximal and distal prostate have been described as tumor initiating cells after *Pten* loss (Guo et al., 2020). Overall, our findings support multiple cells of origin for *Krt4*+ intermediate cells in *Pten*$^{fl/fl}$ mice, including phenotype switching of basal and luminal cells, as well as potential expansion of luminal progenitor cells. In vivo lineage tracing studies using highly precise Cre-drivers will likely be necessary to fully disentangle the cellular origins of intermediate cell states in the *Pten*$^{fl/fl}$ prostate cancer model.

2.3.3 Immune infiltration increases in Pten$^{fl/fl}$ *mice and is pro-tumorigenic*

Our GSEA of all three epithelial cell types showed an enrichment for immune-related pathways in *Pten*$^{fl/fl}$ mice, suggesting increased immunogenic signaling relative to WT mice (Fig. 2.3.2A). To

determine the impact of epithelial *Pten* loss on immune cells, we calculated the relative abundance of immune cells in WT and *Pten*$^{fl/fl}$ mice. We found that T cells, macrophages, neutrophils, and dendritic cells were all significantly expanded in the *Pten*$^{fl/fl}$ mouse; in fact, only B cells were not expanded compared to WT (Fig. 2.3.S3A–B). Immune infiltration has previously been characterized as immunosuppressive in PTEN null prostate tumors (Garcia et al., 2014). Therefore, we expected these expanding immune populations to be immunosuppressive and therefore pro-tumorigenic. To test this hypothesis, we assigned activation states or subtypes to immune cells based on known biomarkers (Fig. 2.3.2B, Fig. 2.3.S3C–E). First, we characterized the neutrophil population as myeloid-derived suppressor cells (MDSCs) based on published biomarkers (Alshetaiwi et al., 2020; Fig. 2.3.S3C). We also found three macrophage cell states: tumor-associated macrophages (TAMs), M2-activated macrophages, and M1-activated macrophages. Interestingly, the M1 cells expressed the AR-dependent markers *Sbp* and *Defb50* and as a result, we termed them tissue-resident macrophages (TRM, Fig. 2.3.S3D). Finally, we characterized three T cell subtypes: $CD8^+$ T cells, gamma-delta T cells, and natural killer T (NKT) cells. $CD8^+$ and gamma-delta T cells expressed the markers of exhaustion and immunosuppression *Pdcd1* and *Ctla4*, suggesting their cytotoxic activity may be dampened in the context of *Pten* loss (Fig. 2.3.S3E). All these cell types except for NKT cells and TRMs are expanded in *Pten*$^{fl/fl}$ mice, implying a potential role for these immune cells in establishing or maintaining a pro-tumorigenic prostate tumor microenvironment (Fig. 2.3.2C).

M2 macrophages, TAMs, and MDSCs are generally pro-tumorigenic (Zaynagetdinov et al., 2011; Chanmee et al., 2014; Garcia et al., 2014). Together with exhausted $CD8^+$ T cells, this suggests a broadly pro-tumorigenic immune environment. We hypothesized that cell-cell signaling originating from tumor epithelial cells may play an important role in recruiting immune cells to the prostate. To probe cell-cell interactions in our system, we used a ligand-receptor database and interaction algorithm that classifies the strength of specific ligand-receptor interactions between cell groups (Efremova et a., 2020). We found key interactions between epithelial subtypes and M2 macrophages and TAMs, such as interactions targeting the *Cd74* receptor, that point to active recruitment (Fig. 2.3.2D). Ligands in the epithelial basal, intermediate, and differentiated cell populations were more highly expressed in *Pten*$^{fl/fl}$ mice than in WT mice, which corresponds to the increased macrophage abundance in *Pten*$^{fl/fl}$ mice (Fig. 2.3.2E).

Additionally, we observed increased *Ccl2/7/11-Ccr2* interactions between fibroblasts and M2/TAMs upon *Pten* loss, suggesting that fibroblasts in prostate cancer may also play an active role in macrophage recruitment (Fig. 2.3.S3F). *Ccl2/7/11* are all significantly upregulated in *Pten*$^{fl/fl}$ fibroblasts (Fig. 2.3.S3G). Interestingly, *Ccr2* is expressed highly in M2 and TAMs in cancer, but not in TRMs (Fig. 2.3.S3H). The lack of fibroblast signaling to TRMs provides a possible cellular explanation for the lower

abundance of this macrophage subtype in *Pten*$^{fl/fl}$ mice compared to WT. Another possibility is that TRMs polarize and transition into M2/TAM macrophages, potentially in response to epithelial signaling. Overall, these findings highlight a role for epithelial cells and fibroblasts in recruiting pro-tumorigenic macrophages to the prostate in the context of *Pten* loss.

While we observed significant epithelial to macrophage signaling, the top interactions between epithelial cells and MDSCs were characterized by receptors expressed in epithelial cells and ligands expressed in MDSCs. As such, it is unlikely that epithelial cells are responsible for the expansion of MDSCs in the prostate (Fig. 2.3.S3I). Instead, we noted increased expression of the *Ccr1* receptor in MDSCs, and a concomitant increase in *Ccl6/7/8/9* expression in M2 macrophages. These genes are known *Ccr1* ligands (Korbecki et al., 2020), which suggests that MDSCs are recruited by M2-activated macrophages (Fig. 2.3.2F). Interestingly, *Ccl6/7/8/9* are not expressed in TRMs or TAMs, highlighting the specificity of M2-MDSC signaling.

Finally, we examined interactions between epithelial cells and T cells. We found both attractive (*Cxcr6*-*Cxcl16*) and pro-exhaustion (*Pdcd1*-*Fam3c*) interactions between CD8$^+$ T cells and epithelial cells. We found these same interactions between macrophages and CD8$^+$ cells, as well as *Cd86*-*Ctla4*/*Cd28* interactions (Fig. 2.3.2G). *Ctla4* and *Cd28* belong to the same family of T cell co-stimulator receptors. *Ctla4* has a suppressive effect while *Cd28* is activating, and both receptors are targeted by the *Cd86* ligand (Gmünder and Lesslauer, 1984; Salomon and Bluestone, 2001; Boesteanu and Katsikis, 2009). These findings imply a synergistic signaling pattern with both tumor epithelia and macrophages recruiting and mitigating the cytotoxicity of T cells. We noted that TAMs exhibited particularly robust expression of *Cxcl16* and *Cd86*, suggesting that similar to M2-mediated MDSC recruitment, TAMs may specifically be responsible for modulating T-cell abundance and function (Fig. 2.3.2H).

Overall, our data suggests that pro-tumorigenic macrophages are recruited by epithelial and fibroblast signaling in *Pten* null tumors. These macrophages then assist tumor signaling in remodeling the immune environment, including recruiting and exhausting cytotoxic CD8$^+$ T cells and attracting pro-tumorigenic MDSCs. Given ligand expression data, M2 macrophages may be mainly responsible for MDSC recruitment and TAMs for CD8$^+$ T cell recruitment. These findings reveal a complex signaling system with multiple coordinated sources of ligand expression working in tandem to build a microenvironment favorable to tumor escape from immunological suppression.

2.3.4 Castration-induced intermediate cell heterogeneity drives resistance to androgen deprivation

Having examined epithelial and immune populations in prostate cancer initiation, we sought to determine how these cells reorganize over the course of castration resistance. It has been shown that

castration of *Pten*$^{fl/fl}$ mice leads to the emergence of AR-low tumors (Liu et al., 2019). As such, we conducted scRNAseq in 6 months old *Pten*$^{fl/fl}$ mice with and without castration at 4 months of age and evaluated the changes that occurred in the epithelial compartment (Fig 2.3.3A). Castration caused the intermediate luminal cell population to expand while the differentiated luminal cells disappeared entirely (Fig. 2.3.3B–C). We hypothesized that androgen deprivation may differentially affect epithelial subtypes. To investigate this, we generated an AR activity score using a 20-gene signature (Hieronymus et al., 2006) and found that WT luminal progenitor cells had high AR activity, but *Pten*$^{fl/fl}$ intermediate cells exhibited very low AR activity in both intact and castrated *Pten*-null conditions. On the contrary, differentiated luminal cells retained high AR activity in *Pten*$^{fl/fl}$ mice (Fig. 2.3.3D). This suggests that loss of *Pten* in intermediate luminal cells decreases their reliance on AR signaling and induces expansion of this compartment upon castration. While it is possible that castration is lethal to differentiated luminal cells, previous studies have shown that they are able to phenotype switch into an intermediate state in AR-low conditions (Karthaus et al., 2020). Therefore, it is likely that this increase in intermediate cell abundance in *Pten*$^{fl/fl}$ castrate mice is due to lineage plasticity in luminal cells. Notably, there were no significant changes in proliferation between the intact and castrate conditions in basal or intermediate cells (Fig. 2.3.S4A).

Given the increase in intermediate cells associated with castration resistant tumor growth, we next asked how castration modulates phenotypic diversity in this population. We isolated and re-clustered intermediate cells from *Pten*$^{fl/fl}$ intact and castrated mice and found six distinct clusters (Fig. 2.3.3E). The majority of intact *Pten*$^{fl/fl}$ intermediate cells (62.8%) congregated in a single cluster (cluster 3), while castrated *Pten*$^{fl/fl}$ intermediate cells were widely distributed over four unique groups (clusters 0, 1, 2, and 4) (Fig. 2.3.3F). DEG analysis showed high expression of AR-dependent genes *Sbp*, *Defb50*, and *Spink1* in cluster 3, suggesting this cell population may have high AR signaling activity relative to other intermediate cells (Fig. 2.3.S4B). This cluster represents cells close to differentiated luminal cells on the epithelial UMAP (Fig. 2.3.3B) and may indicate a luminal origin that could explain retaining high AR activity. Similarly, we observed high expression of the basal cell markers *Krt5* and *Krt15* in cluster 1 (Fig. 2.3.S4B; this cluster corresponds to the intermediate cells proximal to basal cells on the epithelial UMAP (Fig. 2.3.3B)). This supports our hypothesis that some intermediate cells are derived from basal transdifferentiation in the context of cancer, while others may have luminal origins. We also noted multiple ribosomal genes upregulated in clusters 1 and 4, suggesting increased translational signatures in these clusters (Fig. 2.3.S4B). GSEA confirmed enrichment of multiple translation pathways in clusters 1 and 4 (Fig. 2.3.S4C). We also investigated whether castration leads to increased translational signatures in basal cells. We found that several genes encoding ribosomal proteins were overexpressed in castrated basal cells compared to intact *Pten*$^{fl/fl}$ mice (Fig. 2.3.S4D). Together, these findings demonstrate that castration promotes increased heterogeneity of the intermediate cell

populations and potentially diversifies cell-type-specific translation dependence in both basal and intermediate cells in the context of *Pten* loss.

To further characterize the functional differences in castration resistant intermediate cells, we generated AR activity, proliferation, and translation scores for each intermediate cell cluster. We found a gradient of residual AR signaling activity, with cluster 3 having the highest score (Fig. 2.3.3G). Importantly, proliferation and translation activity scores were inversely correlated with AR signaling, with clusters 1 and 4 exhibiting high proliferation and translation scores and low AR scores (Fig. 2.3.3G). We designated the clusters as AR-high, -medium, or -low and noted that intact $Pten^{fl/fl}$ mouse prostates contain mostly AR-high intermediate cells (Fig. 2.3.S4E–F). Upon castration the number of AR-medium and -low cells increase substantially (Fig. 2.3.S4E–F). These findings suggest that castration may select for lower AR expressing cell types with high proliferation, but also conserve some 'intact-like' regions with relatively high AR activity and low proliferation. We also conclude that AR activity in intermediate cells may be correlated with cell of origin, as clusters expressing basal markers (clusters 1 and 4) exhibit low AR activity while cluster 3, which expresses luminal markers, has AR activity comparable to differentiated luminal cells (Fig. 2.3.3G, Fig. 2.3.S4B). Given these correlations, an alternate hypothesis might be that increased basal transdifferentiation, rather than a selection event, is responsible for the increased abundance of AR-low intermediate cells. Lineage-tracing experiments evaluating proliferation and transdifferentiation differences between intact and castrated $Pten^{fl/fl}$ mice will be necessary to fully establish a mechanism for increasing AR-low intermediate cell populations.

Our findings raise the question of what aspects of intermediate cell heterogeneity are driven by castration versus loss of *Pten*? To address this question, we performed single-cell RNA sequencing on 9 WT castrated mouse prostates, which we binned into three replicates to overcome small tissue yields due to atrophy in castrated WT prostates. We found that non-basal cells in WT castrate mice aggregate into one clustered region separate from both WT intact luminal cells and $Pten^{fl/fl}$ intermediate cells, but interestingly were closest to WT luminal progenitor cells (Fig. 2.3.S4G). We evaluated the changes in AR activity, translation, and proliferation in basal and luminal cells between WT intact and castrated cells. We found that similar to $Pten^{fl/fl}$ intermediate cells, lower AR activity was associated with an increase in a translation signature. However, unlike the $Pten^{fl/fl}$ intermediate cells we observed a decrease in the proliferation signature (Fig. 2.3.3H). These findings demonstrate that castration plays an important role in translational heterogeneity in intermediate cells. However, the change in proliferation is likely related to loss of *Pten*.

2.3.5 Castrate intermediate cell signature correlates with advanced prostate cancer and worse patient outcomes

Given the widespread use of the *Pten*$^{fl/fl}$ model (Ding et al., 2011; Svensson et al., 2011; Hsieh et al., 2012; Garcia et al., 2014; Hsieh et al., 2015; Ku et al., 2017; Allott et al., 2018; Antoch et al., 2020; Morel et al., 2021; Quaglia et al., 2021) and our new understanding of cellular dynamics in the context of disease progression, we sought to determine which cell type and context most closely correlated with human prostate cancers that went on to resist androgen deprivation therapy (ADT). To this end, we used a gene signature of ADT resistance derived from human prostate tumors prior to treatment with ADT plus the AR inhibitor enzalutamide, in a neoadjuvant setting (Fig. 2.3.4A) (NCT02430480) (Karzai et al., 2021; Wilkinson et al., 2021; Ku et al., 2021). We generated DEG lists for each epithelial cell type (basal, intermediate, luminal) comparing WT and *Pten*$^{fl/fl}$ or *Pten*$^{fl/fl}$ intact and castrated prostates and performed enrichment analysis using the ADT resistance signature. Out of all the cell types, castrated intermediate cells compared to intact intermediate cells exhibited the most enrichment for the resistance signature (Fig. 2.3.4B). The top five genes from the resistance signature that were upregulated in castrated intermediate cells were *ATP1B1*, *BST2*, *CP*, *IGFBP3*, and *PTTG1*. Importantly, these genes were downregulated in cluster 3 of our intact intermediate cells compared to castrate clusters, demonstrating specificity for aggressive disease (Fig. 2.3.S5A). Furthermore, all five genes were upregulated in human tumors that exhibited pathologic resistance to ADT (Fig. 2.3.S5B). Lastly, we sought to investigate whether these genes were associated with worse outcomes for prostate cancer patients. We examined disease-free survival (DFS) of patients stratified by high or low expression of the five top genes across two major prostate cancer cohorts (Network, 2015; Taylor et al., 2010). We found that patients whose tumor samples expressed high levels of any of these five enriched genes experienced significantly shorter disease-free survival (Fig. 2.3.4C, Fig. 2.3.S5C). We also analyzed patients with *PTEN* loss or PI3K/AKT pathway dysregulation from the TCGA dataset and found the same trend (Fig. 2.3.S5D). These results suggest that the castrate intermediate cell state in the *Pten*$^{fl/fl}$ may correlate with poor patient outcomes.

Given our finding that a 5-gene signature derived from castrate intermediate cells correlates to human clinical phenotypes, we investigated if this signature is enriched in metastatic disease. We integrated single-cell RNA sequencing data from primary prostate cancers (n=11) (Song et al., 2022) and metastatic prostate cancers (n=6) (Dong et al., 2020) and found that primary and metastatic cells clustered separately (Fig. 2.3.4D). We generated a composite score of our 5-gene signature on a per-cell basis and visualized it on the UMAP. We observed an enrichment of the signature only in metastatic patients (Fig. 2.3.4E). Importantly, the cluster containing this signature was composed of cells from five out of the six metastatic samples. These findings show that our 5-gene signature is enriched in human metastatic prostate cancer.

Finally, a possible confounding factor in this model is that physical castration of the *Pten*$^{fl/fl}$ model alone could be driving the expression of the 5-gene signature. To investigate this, we examined single-cell sequencing data from an orthogonal non-castrated mouse model of cancer progression (Brady et al., 2021). This study used prostate specific autochthonous models including a double knockout *Pten*$^{-/-}$*/Rb1*$^{-/-}$ mouse (PR) and a triple mutant *Pten*$^{-/-}$*/Rb1*$^{-/-}$*/Nmyc*$^{+}$ mouse (PRN). PRN mice generate prostate tumors with significantly stronger castration resistance compared to PR mice (Brady et al., 2021). Single-cell RNA sequencing data in this study was produced without castration in both PR and PRN mice, resulting in a model of cancer progression outside of physical castration. We overlaid our 5-gene resistance signature on UMAPs of both mouse models and found strong enrichment of the signature in PRN mice compared to PR mice (Fig. 2.3.4F–G). These results reveal that the 5-gene signature is likely not driven by castration alone. Together, our findings demonstrate that a gene signature generated through a specific cell-type within murine prostate cancer closely correlates with human CRPC and worse outcomes in patients.

2.3.6 Androgen deprivation decreases immune cell abundance but activates Tnf *signaling*

Androgen deprivation induces a host of physiological changes in the prostate, including modulations of immune signaling (Sha et al., 2015; Lopez-Bujanda et al., 2021). Having observed significant epithelial changes in castrated *Pten*$^{fl/fl}$ mice, we next investigated the consequences of castration on the immune environment. We observed a significant decline in the abundance of all 3 macrophage subtypes, as well as CD8^{+} T cells, relative to intact *Pten*$^{fl/fl}$ mice (Fig. 2.3.5A–B). We performed ligand-receptor interaction analysis to understand how androgen deprivation disrupts cell-cell signaling patterns. We found that epithelial signaling to macrophage cells was still intact, with relatively little change in ligand or receptor expression (Fig. 2.3.S6A–B). However, the *Ccl2/7/11-Ccr2* signaling axis from fibroblasts to M2 macrophages and TAMs was entirely ablated in castrated *Pten*$^{fl/fl}$ mice (Fig. 2.3.5C). *Ccr2* expression was significantly decreased in macrophages, and *Ccl2/7/11* were all dramatically decreased in fibroblasts (Fig. 2.3.5D). This suggests that fibroblast-mediated macrophage recruitment is interrupted by androgen deprivation. Indeed, androgen signaling is known to promote pro-tumorigenic macrophage function as well as macrophage recruitment via *Ccr2* expression, lending credence to this hypothesis (Lai et al., 2009; Cioni et al., 2020; Becerra-Diaz et al., 2020). TRMs also decreased in abundance, but they were not targeted by fibroblast signaling and epithelial signaling was uninterrupted. Given the expression of AR-dependent genes in this macrophage subtype (Fig. 2.3.S3D), we speculated that loss of androgen signaling could be deleterious to this population. Indeed, in intact *Pten* $^{fl/fl}$ mice TRMs had high AR activity relative to other macrophage subtypes, and this activity was decreased by castration (Fig. 2.3.S6C). This suggests that castration interrupts fibroblast-mediated pro-tumorigenic M2 and TAM recruitment and depletes the

androgen-dependent tissue-resident macrophage reservoir, leading to decreased macrophage abundance in the prostate.

Macrophages likely contribute to $CD8^+$ T cell recruitment in intact *Pten*$^{fl/fl}$ mice (Fig. 2.3.2G–H); we speculated that macrophage-mediated signaling might be interrupted in the context of castration and cause a decrease in $CD8^+$ T cell abundance. Indeed, while epithelial-$CD8^+$ interactions were mostly intact, *Cd86-Cd28/Ctla4* signaling from M2 macrophages and TAMs was disrupted, and *Cd86* expression was greatly reduced in both M2s and TAMs (Fig. 2.3.5E). In addition, receptor expression was decreased in $CD8^+$ T-cells, including suppressive markers *Ctla4* and *Pdcd1* (Fig. 2.3.5F). These findings suggest that depletion of the macrophage population causes a decrease in both $CD8^+$ T cell recruitment and suppression, possibly leading to more cytotoxic but less abundant $CD8^+$ T cells in castrated *Pten*$^{fl/fl}$ mice.

Finally, *Tnf* signaling has previously been implicated as a pro-tumorigenic factor in AR low prostate cancer (Mizokami et al., 2000; Sha et al., 2015). Accordingly, we examined *Tnf* interactions in our ligand-receptor analysis and found a striking enrichment of *Tnf* pathway activity in castrated mice. Specifically, pro-tumorigenic myeloid cells (M2 macrophages, TAMs, and MDSCs) expressing *Tnf* interact with multiple receptors in epithelial cells and fibroblasts (Fig. 2.3.5G). To investigate whether this association held true in human prostate cancer, we correlated a 200 gene signature of *Tnf* activity (Griss et al., 2020) with AR signaling activity in the prostate cancer TCGA dataset (Network, 2015). We found a significant inverse correlation between TNF and AR activity in human patients, validating our finding that TNF signaling is induced in prostate cancer upon castration (Fig. 2.3.5H). This correlation also held true when only considering patients with PTEN loss (Fig. 2.3.S6D). We conclude that castration in the *Pten*$^{fl/fl}$ mouse provokes several large-scale cellular signaling changes that result in decreased macrophage and $CD8^+$ T cell populations and increased *Tnf* signaling.

2.3.7 Translation inhibition in AR-low prostate cancer is lethal to basal and intermediate cells and disrupts pro-tumorigenic signaling

Deregulated mRNA translation rates have previously been implicated in aberrant gene expression and aggressive AR-low prostate cancer in the *Pten*$^{fl/fl}$ mouse (Liu et al., 2019; Lim et al., 2021). However, understanding how the per cell requirement for aberrant translation enables tumor heterogeneity has been technically challenging. Therefore, it remains to be determined which prostate cancer epithelial cell types require increased translation for androgen independent growth. Given the strong correlation between proliferation and translation observed in both basal and intermediate cells (Fig. 2.3.3, Fig. 2.3.S4D), we hypothesized that inhibiting translation in the *Pten*$^{fl/fl}$ mouse could be

deleterious to both cell types. To investigate this possibility, we used the *PB-Cre4;Pten*$^{fl/fl}$*;ROSA26-rtTA-IRES-eGFP;TetO*-4ebp1^{M} mouse model (herein referred to as *Pten*$^{fl/fl}$*;*4ebp1^{M}). In this model, Cre-mediated recombination leads to *Pten* loss and expression of the rtTA protein in both basal and intermediate cells (Fig. 2.3.S1B). When mice are treated with doxycycline, a mutant *Eif4ebp1* transgene (4ebp1^{M}) is expressed (Hsieh et al., 2015). eIF4EBP1 is a negative regulator of translation initiation and functions via inhibition of eIF4F complex assembly (Schuster and Hsieh, 2019). This mutant allele cannot be inactivated via mTOR-mediated phosphorylation and its expression robustly inhibits eIF4F complex formation and translation initiation in prostate epithelia (Fig. 2.3.6A). Using this model, we sought to determine the epithelial cell type specific dependencies of castration resistant prostate cancer. Here, doxycycline was administered starting at 4 months of age, simultaneously with castration, and prostates were collected at 6 months of age.

Initially, no major differences were observed in the UMAP comparing all epithelial cells in castrated *Pten* $^{fl/fl}$ mice with or without 4ebp1^{M} (Fig. 2.3.6B). However, we noted a striking (~10-fold) depletion of the *rtTA-eGFP* transgene which is required for 4ebp1^{M} induction in *Pten*$^{fl/fl}$*;*4ebp1^{M} basal and intermediate epithelial cells compared to the *Pten*$^{fl/fl}$ model (Fig. 2.3.6C, Table 1). We hypothesized that translation inhibition in AR-low prostate cancer might be lethal or confer a competitive disadvantage to AR low epithelial cells, and that the bulk of the remaining epithelia did not express the 4ebp1^{M} and were simply castrate cells that did not express the transgene. To test this hypothesis, we performed DEG analysis only on transgene-positive cells, comparing castrated cells with or without 4ebp1^{M}. We found many more differentially expressed genes between these groups in basal cells (465 differentially expressed genes) than in the non-filtered analysis (56 DEGs). We did not observe a significant change in the number of DEGs between castrated *Pten*$^{fl/fl}$ and *Pten*$^{fl/fl}$*;*4ebp1^{M} intermediate cells when filtering for *rtTA-eGFP*+ cells. This may be due to the high phenotypic diversity in this compartment and the very low proportion of transgene-positive intermediate cells after 4ebp1^{M} induction (<1%, Table 1) causing a lack of robustness in the DEG analysis.

Interestingly, upon performing pathway analysis on basal cell DEGs we found enrichment of pathways relating to translation, cell cycle arrest, and apoptosis, and observed downregulation of mitochondrial function and mTORC1 signaling pathways (Fig. 2.3.6D). These findings suggest that remaining transgene-positive basal cells in the *Pten*$^{fl/fl}$*;*4ebp1^{M} mice may be undergoing cell cycle arrest, interruption of growth processes such as inhibition of the mTOR pathway, and apoptosis. We also noted that in the basal compartment, the proportion of hyperproliferative cells had decreased drastically (Table 2). This suggests that highly proliferative basal cells are more dependent upon high translation than less proliferative basal cells.

Given the large-scale changes in epithelial populations caused by 4ebp1^{M} induction in castrated *Pten*$^{fl/fl}$ mice, we next asked how cell-cell signaling between the remaining epithelial cells and other compartments were affected by the loss of basal and intermediate cell populations through translation inhibition. We found that *Tnf* signaling was greatly decreased between myeloid and epithelial cells (Fig. 2.3.6E–F). In addition, epithelial-fibroblast and inter-epithelial *Egfr* signaling also decreased significantly (Fig. 2.3.6G–H). *Egfr* activity is associated with worse cancer prognosis, and inhibition of *Egfr* signaling has been proposed as a therapeutic approach in advanced prostate cancer (Kim et al., 2006; Guérin et al., 2010; Xiong et al., 2020). Overall, these findings show that both basal and intermediate cancer cell types require increased translation initiation to maintain castration resistance and that aberrant mRNA translation is required for tumor heterogeneity. Furthermore, translation inhibition of distinct epithelial populations can impact the local tumor microenvironment.

2.4 Discussion

Here, we demonstrated that *Pten* deletion in mouse prostate epithelial cells results in the generation of an intermediate luminal subtype, which is phenotypically similar to but likely distinct from the *Psca*+/*Krt4*+/*Tacstd2*+ luminal progenitor populations in the WT prostate. In this model, the *Pten*$^{fl/fl}$ intermediate cells likely derive from three cellular pools: basal cells, luminal progenitor cells, and differentiated luminal cells. Our findings support the idea that basal cells can transdifferentiate into intermediate cells upon loss of *Pten*. This corresponds well with lineage tracing studies (Choi et al., 2012; Wang et al., 2013; Lu et al., 2013) that showed that basal cells can be cells of origin for prostate cancer and transition to luminal phenotypes during transformation in mice. We also identify common luminal markers expressed in some intermediate cells, suggesting luminal cells may also phenotype switch to an intermediate state upon *Pten* loss. Lastly, the close proximity of luminal progenitor cells to intermediate cells and the fact they can express AR and form neoplasia in the context of *Pten* loss (Guo et al., 2020) reveal another potential source of intermediate cells. Our study is limited by the fact that the Cre driver is active in all epithelial subtypes. To observe transdifferentiation or phenotype switching, cell type specific lineage tracing will be required. New techniques such as DNA Typewriter may offer flexible multiplexed platforms to track multiple cell lineages in the same system simultaneously (Choi et al., 2022).

We observed that intermediate cells undergo significant cell state changes upon castration which increases their heterogeneity. This heterogeneity is characterized by a spectrum of AR signaling inversely correlated with both proliferation and translation activity. Within this spectrum, clusters with high AR activity and low proliferation and translation express some luminal markers, while low AR, high proliferation, high translation clusters express basal markers. This finding supports the hypothesis that both basal and luminal cells can transdifferentiate to intermediate cells in cancer and suggests that

basal-originating intermediate cells may represent more aggressive cancer phenotypes. These specific intermediate clusters may be responsible for the increased tumor growth previously observed at the whole-prostate level in castrated *Pten*$^{fl/fl}$ mice (Liu et al., 2019). This lends importance to the question of whether increased AR-low intermediate populations in *Pten*$^{fl/fl}$ castrate mice are due to the expansion of an existing cell state, or renewed lineage plasticity events from basal cells. Comparative lineage tracing experiments measuring basal transdifferentiation and proliferation dynamics in intact and castrated *Pten*$^{fl/fl}$ mice will be necessary to fully address this question. Overall, we speculate that the intermediate cell compartment is highly heterogeneous in *Pten*$^{fl/fl}$ mice partly due to multiple cellular origins converging on a common phenotype.

We further characterize the effects of intermediate cell expansion by showing that a 5-gene signature enriched in this cell type correlates with poor patient outcomes, advanced human CRPC, and castration resistance in an orthogonal mouse model. Specifically, we observe that upregulation of these 5 genes significantly correlates with shorter disease-free survival in two datasets of bulk RNA-seq from patients. We also find that the 5-gene signature is specifically enriched in a subset of metastatic, but not primary, human prostate cancer cells (Song et al., 2022; Dong et al., 2020). Finally, we demonstrate the enrichment of the signature in an orthogonal murine model of prostate cancer progression and castration resistance (Brady et al., 2021). Our findings suggest that intermediate cells are enriched for a gene signature of treatment resistance in human tumors and pose the intriguing question of whether detection of this population in patients can provide a useful prognostic tool. Further in vivo studies will be necessary to validate the role of intermediate cell states in human disease and their potential implications in clinical medicine.

The prostate tumor environment is typically described as immunosuppressive and does not readily respond to immunotherapies (Kantoff et al., 2010; Cham et al., 2020; Dong et al., 2020). Correspondingly, we show that the immune environment of the *Pten*$^{fl/fl}$ mouse prostate is highly enriched for pro-tumorigenic immune cells, specifically immunosuppressive myeloid cells and exhausted $CD8^+$ T cells. We carefully delineated cell-cell signaling patterns and found that epithelial cells, fibroblasts, and macrophages contribute to immune recruitment. Since M2 and tumor-associated macrophages most significantly contribute to recruitment of other immune cells, macrophages are likely activated and recruited first during tumorigenesis, and subsequently emit chemokines and other ligands that help attract and exhaust $CD8^+$ T cells as well as pro-tumorigenic MDSCs. Interestingly, specific macrophage subtypes seem differentially responsible for distinct recruitment patterns: M2 macrophages express very high levels of MDSC-associated chemokines, while TAMs recruit $CD8^+$ T cells via high expression of *Cxcl16* and *Cd86*. Given these results, interrupting the recruitment of tumor-associated macrophages may be a valid strategy for depleting pro-tumorigenic immune populations

and overcoming immunotherapy resistance in prostate cancer. In vitro studies utilizing co-cultures of epithelial and immune cells will be required to validate these in silico results and confirm whether the epithelia-macrophage signaling axis is an appropriate therapeutic target.

Androgen deprivation in the *Pten*$^{fl/fl}$ mouse leads to a decrease in macrophage and CD8^{+} T cell abundance, likely due to ablation of fibroblast-mediated chemokine signaling. Androgen signaling is active in tissue-resident macrophages and can induce pro-tumorigenic behaviors including increased migration and proliferation in prostate cancer cells (Cioni et al., 2020). In addition, AR can promote *Ccr2* expression and facilitate macrophage activity and recruitment (Lai et al., 2009). This corresponds well to our finding that fibroblast-mediated signaling towards *Ccr2* contributes to macrophage recruitment and is interrupted upon castration, and suggests that androgen deprivation decreases macrophage abundance in the prostate tumor environment. Conversely, castration increased *Tnf* signaling from myeloid cells to epithelial cells and fibroblasts. TNF signaling has been described as pro-tumorigenic in AR-low prostate cancer (Mizokami et al., 2000; Sha et al., 2015), and we confirmed that TNF activity was inversely associated with AR activity in human patients. This paradigm supports the role of macrophages and neutrophils in maintaining a favorable tumor environment even in the context of androgen loss and suggests a mechanistic relationship between castration and pro-tumorigenic immune signaling.

Finally, we tested the hypothesis that high translation rates were important to maintain AR-low prostate cancer heterogeneity using the *Pten*$^{fl/fl}$*;*4ebp1^{M} mouse model. We discovered that 4ebp1^{M} induction severely depleted both basal and intermediate cells. Interestingly, hyper-proliferative basal cells were preferentially depleted, leading to a decrease in overall basal cell proliferation. In addition, *Egfr* and *Tnf* signaling were decreased in the tumor microenvironment. We conclude that high translation rates are essential to maintain tumor heterogeneity in AR-low prostate cancer and may play a role in pro-tumorigenic cell-cell communication pathways. Based on these findings, we speculate that translation inhibitors may represent a therapeutic modality to decrease tumor heterogeneity, and that additional studies may uncover further druggable targets. Overall, our work highlights multiple epithelial and immune cell types crucial to prostate cancer initiation and progression and elucidates interactions between specific cell populations that may facilitate castration resistance. Lastly, this work aims to provide a broad, searchable resource to the cancer research community. To this end, we have developed a publicly accessible and interactive website (available at https://atlas.fredhutch.org/hsieh-prostate/) that allows for cell- and gene-specific queries through all 50,780 cells analyzed in this study (Fig. 2.3.S7).

2.5 Figures and Legends

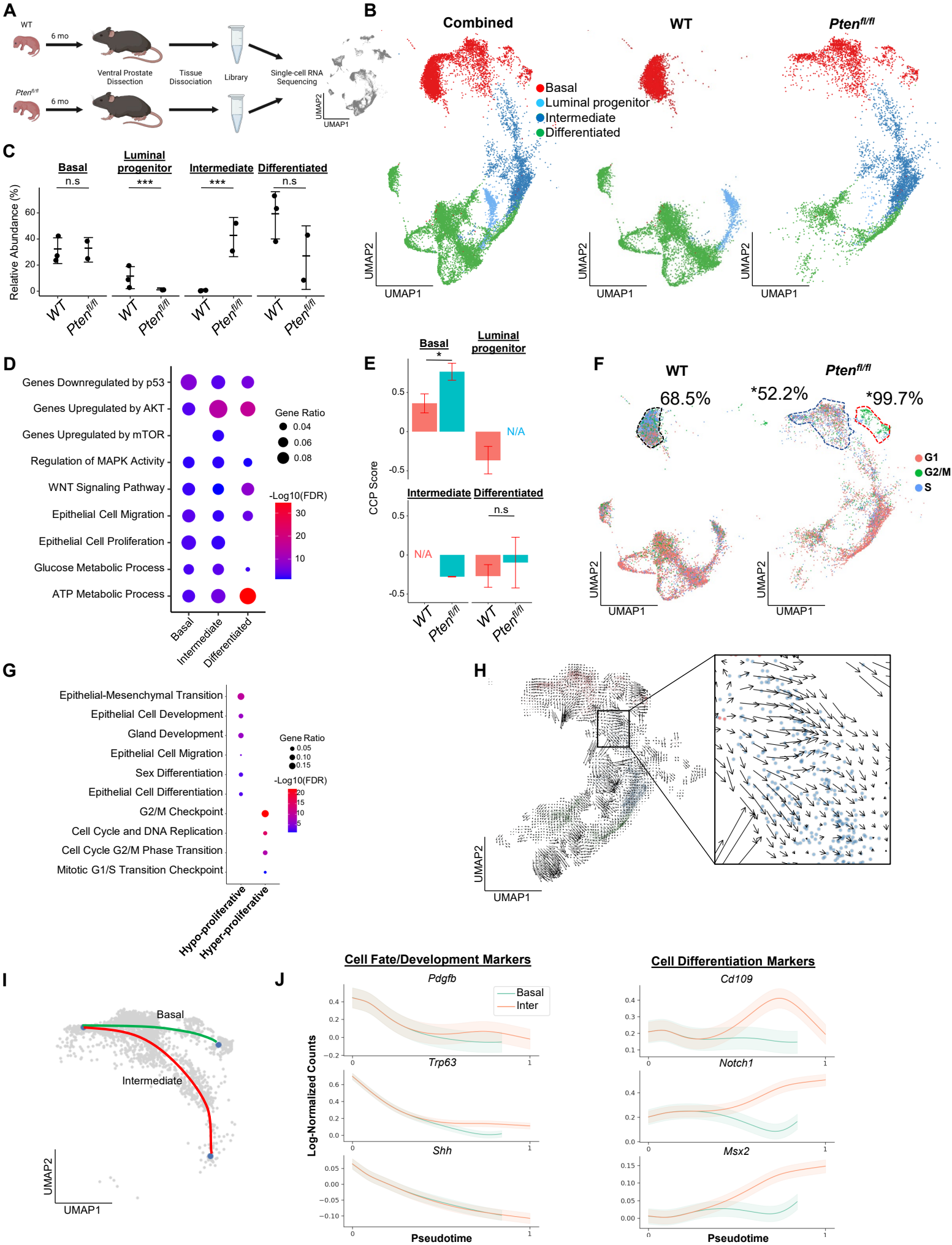
A
WT
6 mo
Ptenfl/fl
6 mo
Ventral Prostate Dissection
Tissue Dissociation
Library
Single-cell RNA Sequencing
UMAP2
UMAP1
B
Combined
WT
Ptenfl/fl
Basal
Luminal progenitor
Intermediate
Differentiated
UMAP2
UMAP1
C
Basal
Luminal progenitor
Intermediate
Differentiated
n.s
***
***
n.s
Relative Abundance (%)
0
20
40
60
WT
Ptenfl/fl
D
Genes Downregulated by p53
Genes Upregulated by AKT
Genes Upregulated by mTOR
Regulation of MAPK Activity
WNT Signaling Pathway
Epithelial Cell Migration
Epithelial Cell Proliferation
Glucose Metabolic Process
ATP Metabolic Process
Gene Ratio
0.04
0.06
0.08
-Log10(FDR)
30
20
10
Basal
Intermediate
Differentiated
E
Basal
Luminal progenitor
*
CCP Score
0.5
0
-0.5
N/A
Intermediate
Differentiated
n.s
N/A
WT
Ptenfl/fl
F
WT
Ptenfl/fl
68.5%
*52.2%
*99.7%
G1
G2/M
S
UMAP2
UMAP1
G
Epithelial-Mesenchymal Transition
Epithelial Cell Development
Gland Development
Epithelial Cell Migration
Sex Differentiation
Epithelial Cell Differentiation
G2/M Checkpoint
Cell Cycle and DNA Replication
Cell Cycle G2/M Phase Transition
Mitotic G1/S Transition Checkpoint
Gene Ratio
0.05
0.10
0.15
-Log10(FDR)
20
15
10
5
Hypo-proliferative
Hyper-proliferative
H
UMAP2
UMAP1
I
Basal
Intermediate
UMAP2
UMAP1
J
Cell Fate/Development Markers
Cell Differentiation Markers
Pdgfb
Cd109
Basal
Inter
Trp63
Notch1
Shh
Msx2
Log-Normalized Counts
Pseudotime
Pseudotime

Figure 2.3.1: Proliferative Split in Basal Cancer Cells Enables Expansion of Intermediate Cells

A) Simplified schematic of single-cell RNA sequencing of WT and *Pten*$^{fl/fl}$ ventral prostates. **B)** UMAP of WT and *Pten*$^{fl/fl}$ epithelial cells. Left, both conditions superposed; middle, WT only; right, *Pten*$^{fl/fl}$ only. Epithelial cell types are demarcated by color (red = basal, light blue = luminal progenitor, dark blue = intermediate, green = differentiated). **C)** Relative abundance of epithelial cells in WT and *Pten*$^{fl/fl}$ mice. Y-axis shows the % composition of each sample by cell type (***p<0.001, negative binomial test). Data presented as +/- SD. **D)** Top GSEA results enriched in *Pten*$^{fl/fl}$ compared to WT for each epithelial subtype. Intermediate cells in *Pten*$^{fl/fl}$ were compared to luminal progenitor cells in WT. All pathways are enriched with FDR < 0.05. **E)** Proliferation signature (CCP) composite score in epithelial cells, clustered by condition (Data presented as +/- SD, *p<0.05, n.s. = not significant, permutation test). N/A indicates missing data due to no cells being present in the condition. **F)** UMAP visualization of cell cycle phase assignment per cell, showing % cells in non-G1 (S or G2/M) (black border = WT basal cells, blue border = hypo-proliferative basal cells in *Pten*$^{fl/fl}$, and red border = hyper-proliferative basal cells in *Pten*$^{fl/fl}$. *p<0.05, chi-square test). **G)** GSEA between hyper- and hypo-proliferative basal clusters in *Pten*$^{fl/fl}$. All pathways are enriched with FDR < 0.05. **H)** RNA velocity analysis of *Pten*$^{fl/fl}$ epithelial cells; highlighted section shows intersection of basal and intermediate cells. **I)** Pseudotime trajectories drawn by Palantir through the basal and intermediate compartments, with hypo-proliferating basal cells as the designated start point. **J)** Expression of important cell fate and differentiation regulators along basal-intermediate trajectory.

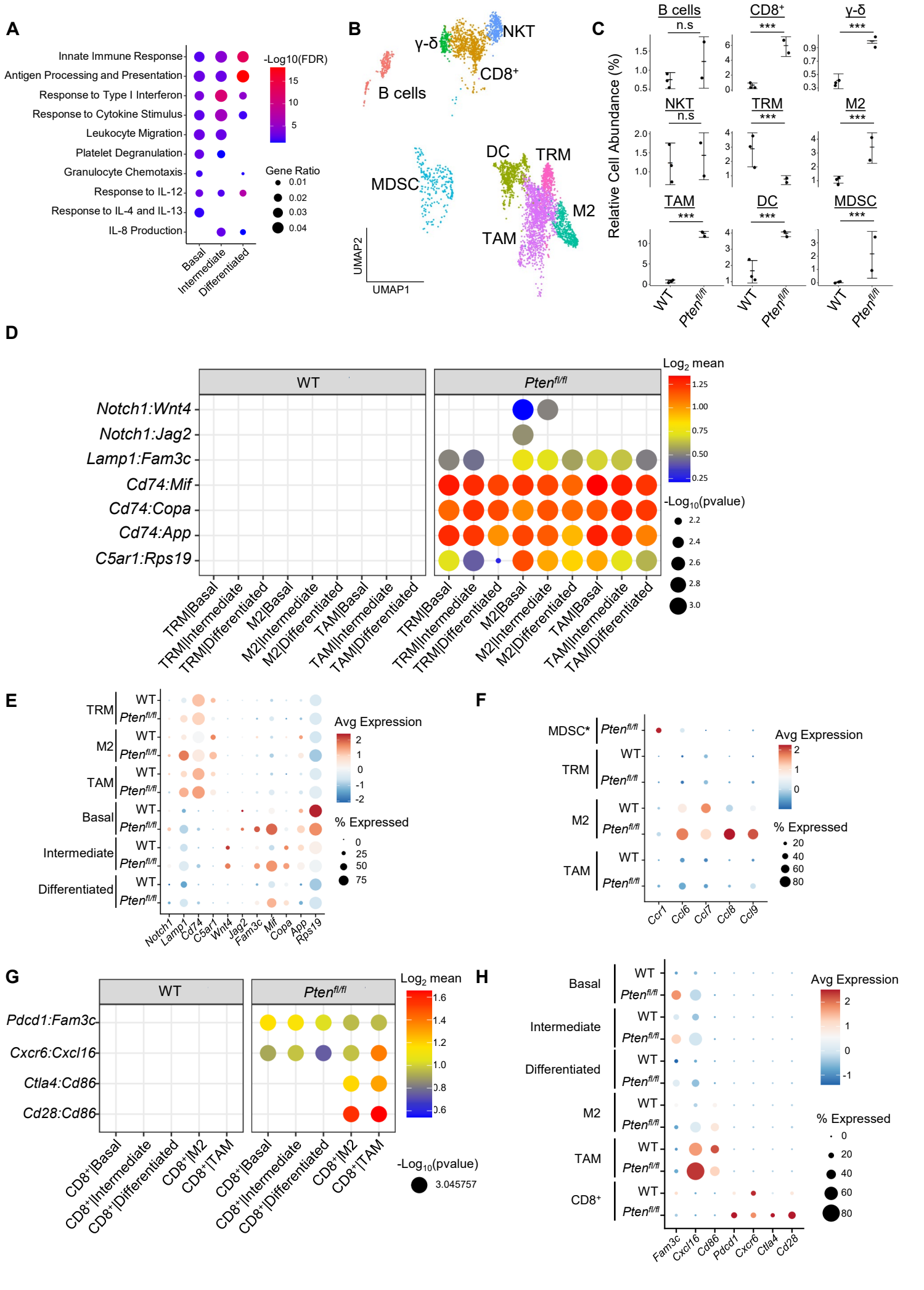
A
Innate Immune Response
Antigen Processing and Presentation
Response to Type I Interferon
Response to Cytokine Stimulus
Leukocyte Migration
Platelet Degranulation
Granulocyte Chemotaxis
Response to IL-12
Response to IL-4 and IL-13
IL-8 Production
Basal
Intermediate
Differentiated
-Log10(FDR)
15
10
5
Gene Ratio
0.01
0.02
0.03
0.04
B
γ-δ
NKT
CD8+
B cells
MDSC
DC
TRM
M2
TAM
UMAP2
UMAP1
C
B cells
n.s
CD8+
***
γ-δ
***
NKT
n.s
TRM
***
M2
***
TAM
***
DC
***
MDSC
***
Relative Cell Abundance (%)
WT
Pten fl/fl
D
WT
Pten fl/fl
Log2 mean
1.25
1.00
0.75
0.50
0.25
-Log10(pvalue)
2.2
2.4
2.6
2.8
3.0
Notch1:Wnt4
Notch1:Jag2
Lamp1:Fam3c
Cd74:Mif
Cd74:Copa
Cd74:App
C5ar1:Rps19
TRM|Basal
TRM|Intermediate
TRM|Differentiated
M2|Basal
M2|Intermediate
M2|Differentiated
TAM|Basal
TAM|Intermediate
TAM|Differentiated
E
TRM
M2
TAM
Basal
Intermediate
Differentiated
WT
Pten fl/fl
Avg Expression
2
1
0
-1
-2
% Expressed
0
25
50
75
Notch1
Lamp1
Cd74
C5ar1
Wnt4
Jag2
Fam3c
Mif
Copa
App
Rps19
F
MDSC*
TRM
M2
TAM
WT
Pten fl/fl
Avg Expression
2
1
0
% Expressed
20
40
60
80
Ccr1
Ccl6
Ccl7
Ccl8
Ccl9
G
WT
Pten fl/fl
Log2 mean
1.6
1.4
1.2
1.0
0.8
0.6
-Log10(pvalue)
3.045757
Pdcd1:Fam3c
Cxcr6:Cxcl16
Ctla4:Cd86
Cd28:Cd86
CD8+|Basal
CD8+|Intermediate
CD8+|Differentiated
CD8+|M2
CD8+|TAM
H
Basal
Intermediate
Differentiated
M2
TAM
CD8+
WT
Pten fl/fl
Avg Expression
2
1
0
-1
% Expressed
0
20
40
60
80
Fam3c
Cxcl16
Cd86
Pdcd1
Cxcr6
Ctla4
Cd28

Figure 2.3.2: Immune Recruitment in *Pten*$^{fl/fl}$ Prostates is Mediated by both Epithelial and Immune Cell Signaling

A) Top immune-related GSEA results enriched in *Pten*$^{fl/fl}$ compared to WT mice for each epithelial subtype. All pathways are enriched with FDR < 0.05. **B)** UMAP visualization of immune cells labeled by cell subtype or state. **C)** Relative abundance of immune cells in WT and *Pten*$^{fl/fl}$ mice. Y-axis shows the % composition of each sample by cell type (Data presented as +/- SD, ***p<0.001, n.s. = not significant, negative binomial test). **D)** Dot plot of signaling interactions between macrophages and epithelial cells. Y-axis, ligand-receptor pairs from CellphoneDB database. X-axis, cell-cell pairings. Interactions are directional: the first gene in a pair is expressed in the first cell in the cell-cell interaction. **E)** Dot plot of epithelial ligand and macrophage receptor gene expression in WT and *Pten*$^{fl/fl}$ mice. **F)** Dot plot of *Ccr1* and *Ccr1* ligand expression in MDSCs and macrophages in WT and *Pten*$^{fl/fl}$ ventral prostates. MDSCs are only present in *Pten*$^{fl/fl}$ and therefore do not have a WT row (denoted by asterisk). **G)** Plot of signaling interactions between CD8+ T cells and epithelial cells and macrophages. **H)** Dot plot of $CD8^+$ T cell receptors and epithelial and macrophage ligand gene expression in WT and *Pten*$^{fl/fl}$ ventral prostates.

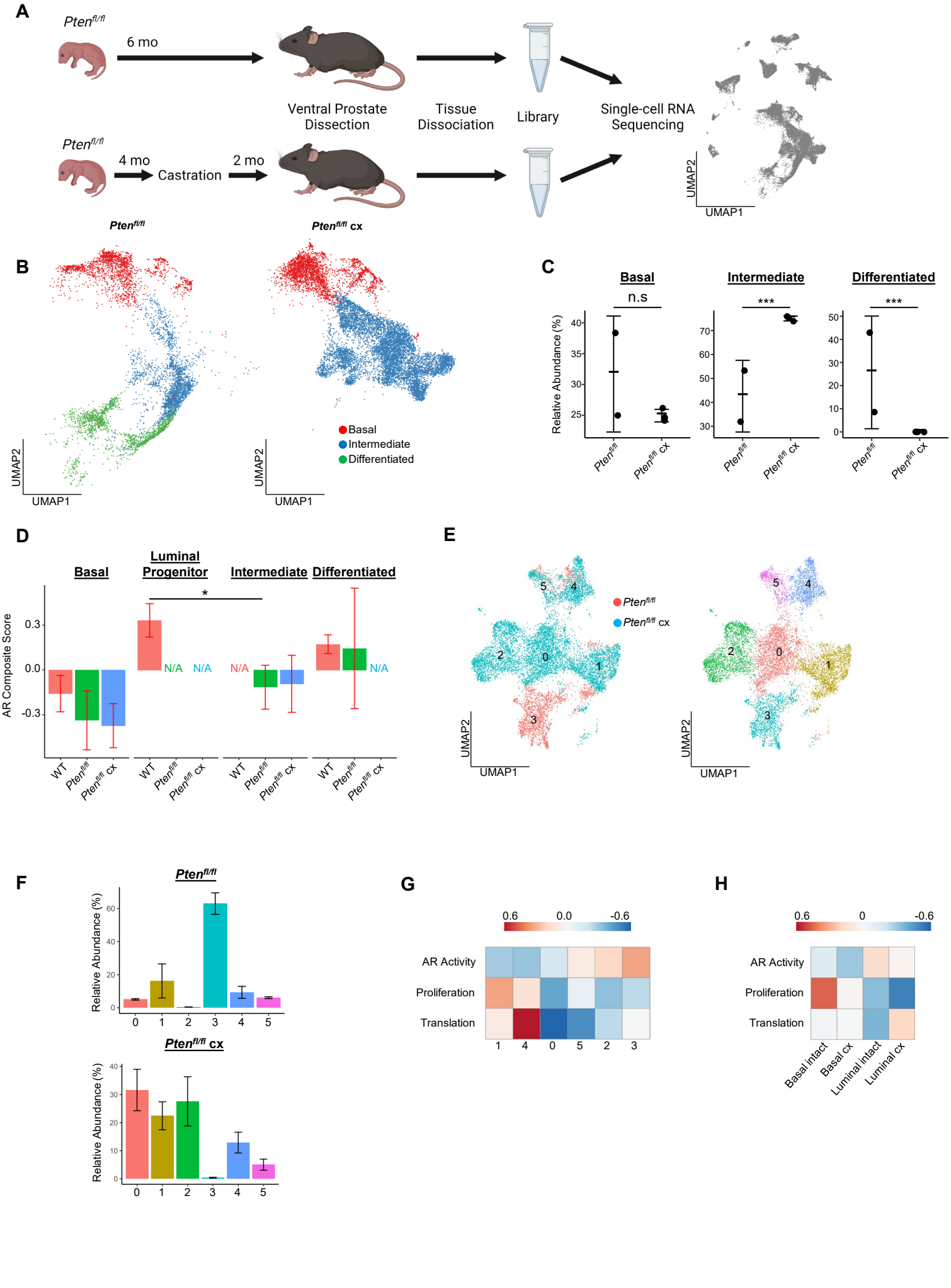
A
Pten fl/fl
6 mo
Ventral Prostate Dissection
Tissue Dissociation
Library
Single-cell RNA Sequencing
Pten fl/fl
4 mo
Castration
2 mo
UMAP2
UMAP1
Pten fl/fl
Pten fl/fl cx
B
Basal
Intermediate
Differentiated
C
Basal
Intermediate
Differentiated
n.s
***
***
Relative Abundance (%)
D
Basal
Luminal Progenitor
Intermediate
Differentiated
*
AR Composite Score
N/A
WT
E
F
Relative Abundance (%)
G
AR Activity
Proliferation
Translation
H
Basal intact
Basal cx
Luminal intact
Luminal cx

Figure 2.3.3: Intermediate Cells are Primed for Survival and Diversification in the Context of Castration

A) Simplified schematic of setup for single-cell sequencing of *Pten*$^{fl/fl}$ intact and *Pten*$^{fl/fl}$ castrated (cx) ventral prostates. **B)** Split UMAP visualizations of *Pten*$^{fl/fl}$ and *Pten*$^{fl/fl}$ cx epithelial cells. **C)** Relative abundance of epithelial cells in *Pten*$^{fl/fl}$ intact and cx prostates. Y-axis shows the % composition of each sample by cell type (Data presented as +/- SD, ***p<0.001, n.s. = not significant, negative binomial test). **D)** Androgen Receptor (AR) gene signature composite score in epithelial cells, clustered by condition (Data presented as +/- SD, *p<0.05, permutation test). N/A indicates missing data due to no cells being present in the condition. **E)** UMAP visualization of intermediate cells in *Pten*$^{fl/fl}$ intact and cx prostates. Left, colored by condition; right, colored by clusters 0-5. **F)** Relative abundance of intermediate clusters. Top, intact *Pten*$^{fl/fl}$; bottom, *Pten*$^{fl/fl}$ cx (Data presented as +/- SD). **G)** Heatmap of composite score for AR, CCP, and Reactome translation gene signatures in intermediate clusters. **H)** Heatmap of composite score for AR, CCP, and Reactome translation gene signatures in WT intact and castrate basal and luminal cells.

Intermediate-Derived Signature Correlates with Poor Prognosis in Human Patients

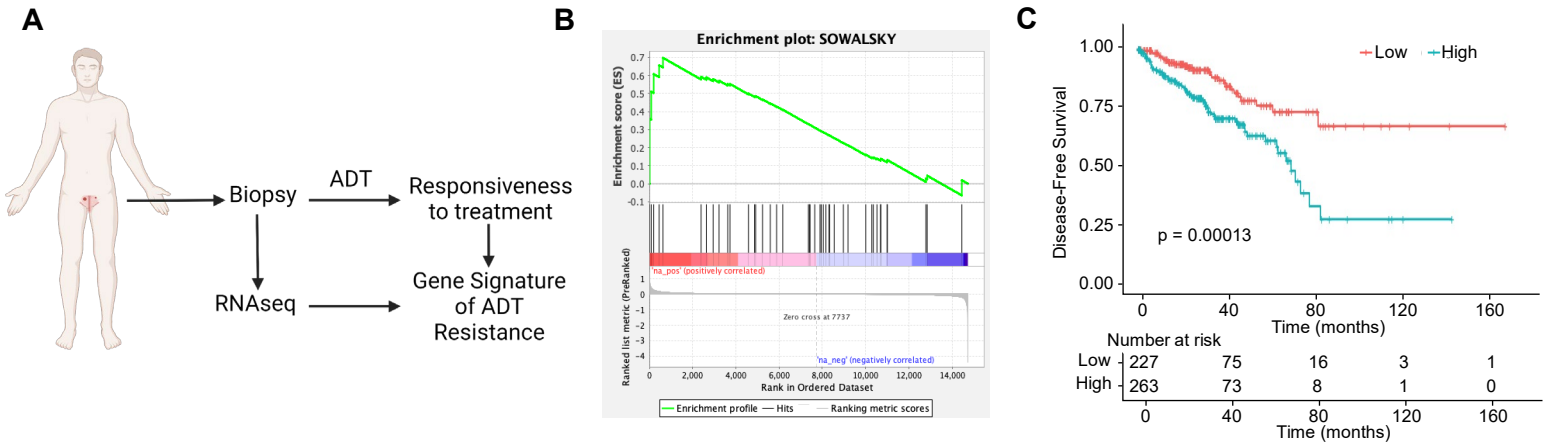

scRNAseq of Patient Samples Shows Enriched Intermediate Signature in Metastasis

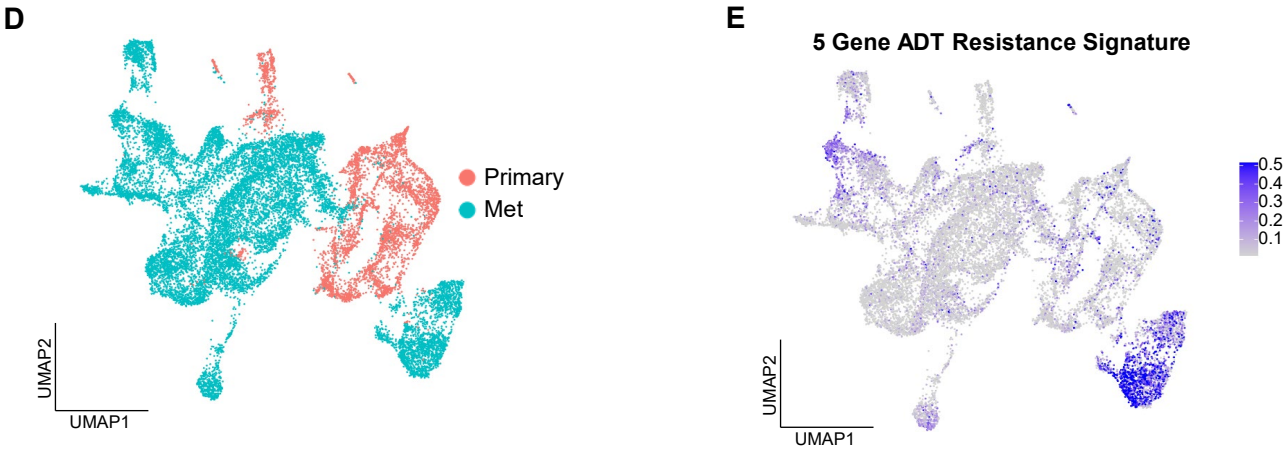

ADT Resistance Signature Correlates with Castration Resistance in Orthogonal Model

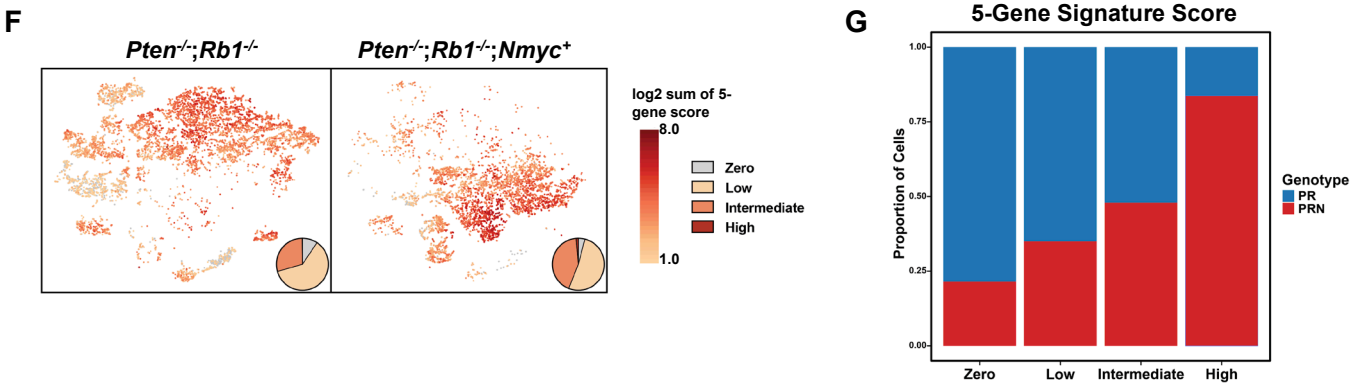

Figure 2.3.4: Intermediate Cells are Enriched for a Signature of Treatment Resistance that Correlates with Advanced Human Disease

A) Diagram of clinical trial used to establish gene signature of androgen deprivation treatment resistance (NCT02430480). **B)** Enrichment plot of ADT resistance gene signature relative to intermediate cell DEGs between *Pten*$^{fl/fl}$ and *Pten*$^{fl/fl}$ cx (adjusted p-value = 0.00381). **C)** Kaplan-Meier curve of disease-free survival for prostate cancer patients in TCGA database with or without high RNA expression of top correlated genes from Figure 4B. Red line, patients with normal expression of all genes; blue line, patients with expression of at least 1 gene with TPM (transcripts per million) in the 80th percentile or above. **D)** UMAP of tumor cells from human patient samples. Red, primary cancer; blue, metastatic cancer. **E)** UMAP visualization of per-cell computed score for 5-gene signature from Figure 4B-C in human cancer samples. **F)** UMAP visualization of per-cell computed score for 5-gene signature from Figure 4B-C in PR and PRN mouse models. Pie charts indicate proportion of cells with zero, low, intermediate, or high signature scores. **G)** Stacked bar chart showing proportion of cells from PR or PRN mice in each scoring category for the 5-gene signature.

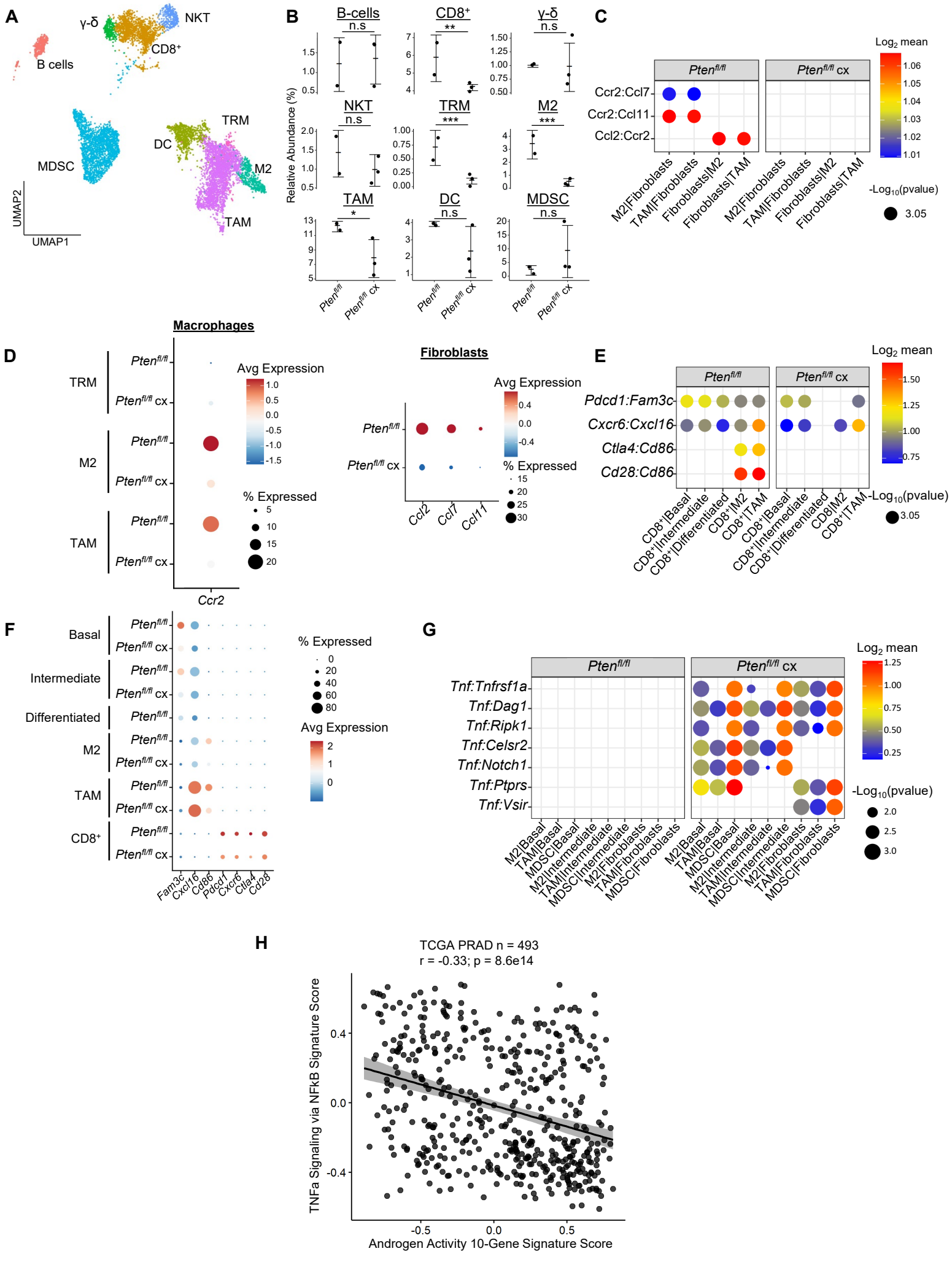
A
γ-δ
NKT
B cells
CD8⁺
MDSC
TRM
DC
M2
TAM
UMAP2
UMAP1
B
B-cells
n.s
CD8⁺
**
γ-δ
n.s
NKT
n.s
TRM
***
M2
***
TAM
*
DC
n.s
MDSC
n.s
Relative Abundance (%)
Pten fl/fl
Pten fl/fl cx
C
Log2 mean
Pten fl/fl
Pten fl/fl cx
Ccr2:Ccl7
Ccr2:Ccl11
Ccl2:Ccr2
M2|Fibroblasts
TAM|Fibroblasts
Fibroblasts|M2
Fibroblasts|TAM
-Log10(pvalue)
3.05
D
Macrophages
TRM
M2
TAM
Pten fl/fl
Pten fl/fl cx
Avg Expression
% Expressed
Ccr2
Fibroblasts
Avg Expression
% Expressed
Ccl2
Ccl7
Ccl11
E
Log2 mean
Pten fl/fl
Pten fl/fl cx
Pdcd1:Fam3c
Cxcr6:Cxcl16
Ctla4:Cd86
Cd28:Cd86
CD8⁺|Basal
CD8⁺|Intermediate
CD8⁺|Differentiated
CD8⁺|M2
CD8⁺|TAM
CD8|M2
CD8⁺|TAM
-Log10(pvalue)
3.05
F
Basal
Intermediate
Differentiated
M2
TAM
CD8⁺
Pten fl/fl
Pten fl/fl cx
% Expressed
Avg Expression
Fam3c
Cxcl16
Cd86
Pdcd1
Cxcr6
Ctla4
Cd28
G
Pten fl/fl
Pten fl/fl cx
Log2 mean
Tnf:Tnfrsf1a
Tnf:Dag1
Tnf:Ripk1
Tnf:Celsr2
Tnf:Notch1
Tnf:Ptprs
Tnf:Vsir
M2|Basal
TAM|Basal
MDSC|Basal
M2|Intermediate
TAM|Intermediate
MDSC|Intermediate
M2|Fibroblasts
TAM|Fibroblasts
MDSC|Fibroblasts
-Log10(pvalue)
H
TCGA PRAD n = 493
r = -0.33; p = 8.6e14
TNFa Signaling via NFkB Signature Score
Androgen Activity 10-Gene Signature Score

Figure 2.3.5: Castration Remodels Immune Environment via Fibroblast Signaling and Increases TNF Pathway Activity

A) Combined UMAP visualization of immune cells in *Pten*$^{fl/fl}$ and *Pten*$^{fl/fl}$ cx ventral prostates. **B)** Relative abundance of immune cells in *Pten*$^{fl/fl}$ intact and cx mice. Y-axis shows the % composition of each sample by cell type (Data presented as +/- SD, *p<0.05, **p<0.01, ***p<0.001, n.s = not significant, negative binomial test). **C)** Dot plot of signaling interactions between macrophages and fibroblasts. **D)** Dot plot of *Ccr2* expression in M2 macrophages and TAMs (left). Dot plot of *Ccr2* ligand expression in fibroblasts in *Pten*$^{fl/fl}$ intact and cx mice (right). **E)** Dot plot of signaling interactions between $CD8^+$ T cells and epithelial and macrophage cells in *Pten*$^{fl/fl}$ intact and cx mice. **F)** Dot plot of epithelial and macrophage ligands and $CD8^+$ T cell receptor gene expression in *Pten*$^{fl/fl}$ intact and cx mice. **G)** Dot plot of *Tnf* signaling interactions between myeloid and epithelial/fibroblast cells in *Pten*$^{fl/fl}$ intact and cx prostates. **H)** Scatter plot of TCGA PRAD study patient signature composite scores. Y-axis, TNF signaling signature score; X-axis, AR signaling signature score (Pearson's correlation).

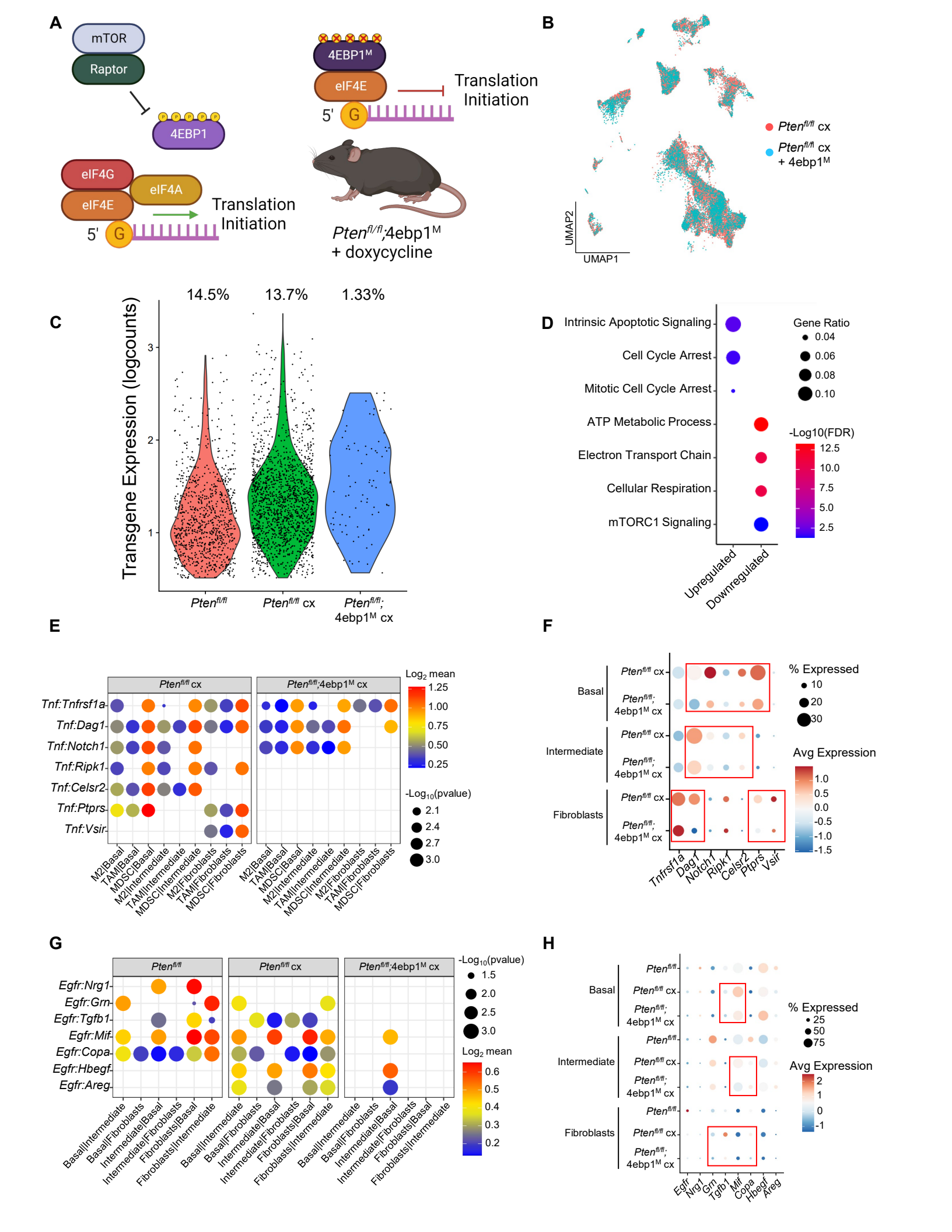
A
mTOR
Raptor
4EBP1
eIF4G
eIF4E
eIF4A
5'
G
Translation Initiation
4EBP1M
eIF4E
5'
G
Translation Initiation
Ptenfl/fl;4ebp1M + doxycycline
B
Ptenfl/fl cx
Ptenfl/fl cx + 4ebp1M
UMAP2
UMAP1
C
14.5%
13.7%
1.33%
Transgene Expression (logcounts)
Ptenfl/fl
Ptenfl/fl cx
Ptenfl/fl; 4ebp1M cx
D
Intrinsic Apoptotic Signaling
Cell Cycle Arrest
Mitotic Cell Cycle Arrest
ATP Metabolic Process
Electron Transport Chain
Cellular Respiration
mTORC1 Signaling
Upregulated
Downregulated
Gene Ratio
0.04
0.06
0.08
0.10
-Log10(FDR)
12.5
10.0
7.5
5.0
2.5
E
Ptenfl/fl cx
Ptenfl/fl;4ebp1M cx
Tnf:Tnfrsf1a
Tnf:Dag1
Tnf:Notch1
Tnf:Ripk1
Tnf:Celsr2
Tnf:Ptprs
Tnf:Vsir
M2|Basal
TAM|Basal
MDSC|Basal
M2|Intermediate
TAM|Intermediate
MDSC|Intermediate
M2|Fibroblasts
TAM|Fibroblasts
MDSC|Fibroblasts
Log2 mean
1.25
1.00
0.75
0.50
0.25
-Log10(pvalue)
2.1
2.4
2.7
3.0
F
Basal
Intermediate
Fibroblasts
Ptenfl/fl cx
Ptenfl/fl; 4ebp1M cx
Tnfrsf1a
Dag1
Notch1
Ripk1
Celsr2
Ptprs
Vsir
% Expressed
10
20
30
Avg Expression
1.0
0.5
0.0
-0.5
-1.0
-1.5
G
Ptenfl/fl
Ptenfl/fl cx
Ptenfl/fl;4ebp1M cx
Egfr:Nrg1
Egfr:Grn
Egfr:Tgfb1
Egfr:Mif
Egfr:Copa
Egfr:Hbegf
Egfr:Areg
Basal|Intermediate
Basal|Fibroblasts
Intermediate|Basal
Intermediate|Fibroblasts
Fibroblasts|Basal
Fibroblasts|Intermediate
-Log10(pvalue)
1.5
2.0
2.5
3.0
Log2 mean
0.6
0.5
0.4
0.3
0.2
H
Basal
Intermediate
Fibroblasts
Ptenfl/fl
Ptenfl/fl cx
Ptenfl/fl; 4ebp1M cx
Egfr
Nrg1
Grn
Tgfb1
Mif
Copa
Hbegf
Areg
% Expressed
25
50
75
Avg Expression
2
1
0
-1

Figure 2.3.6: 4EBP1^{M} Expression is Lethal in Epithelial Cells and Decreases EGFR and TNF ligands in Epithelial Cells and Fibroblasts

A) Simplified schematic of the eIF4F translation initiation complex and how the 4EBP1^{M} protein functions in the *Pten$^{fl/fl}$;*4ebp1^{M} mouse model when treated with doxycycline. **B)** UMAP visualization of epithelial cells in *Pten$^{fl/fl}$* cx and *Pten$^{fl/fl}$;*4ebp1^{M} cx prostates, colored by genotype. **C)** Violin plot of *rtTA-eGFP* transgene expression in epithelial cells in each *Pten$^{fl/fl}$* condition. Plot shows only cells expressing the transgene; each dot represents a cell. Percentages represent the proportion of transgene-positive cells in each condition. **D)** Dot plot of top GSEA results from DEG analysis of transgene-positive basal cells in *Pten$^{fl/fl}$;*4ebp1^{M} cx mice compared to *Pten$^{fl/fl}$* cx ventral prostates. All pathways are enriched with FDR < 0.05. **E)** Dot plot of *Tnf* signaling interactions between myeloid and epithelial/fibroblast cells in *Pten$^{fl/fl}$* cx and *Pten$^{fl/fl}$;*4ebp1^{M} cx mice. **F)** Dot plot of *Tnf* and *Tnf* ligand expression in myeloid cells, epithelial cells, and fibroblasts in *Pten$^{fl/fl}$* cx and *Pten$^{fl/fl}$;*4ebp1^{M} cx prostates. Red boxes highlight ligands with decreased expression in *Pten$^{fl/fl}$;*4ebp1^{M} cx mice. **G)** Plot of *Egfr* signaling interactions between epithelial cells and fibroblasts in *Pten$^{fl/fl}$* intact, *Pten$^{fl/fl}$* cx, and *Pten$^{fl/fl}$;*4ebp1^{M} cx prostates. **H)** Dot plot of *Egfr* and *Egfr* ligand expression in epithelial cells and fibroblasts in *Pten$^{fl/fl}$* intact, *Pten$^{fl/fl}$* cx, and *Pten$^{fl/fl}$;*4ebp1^{M} cx ventral prostates. Red boxes highlight ligands with decreased expression in *Pten$^{fl/fl}$;*4ebp1^{M} cx mice.

Tables

Cell Type		***Pten*$^{fl/fl}$**	***Pten*$^{fl/fl}$ cx**	***Pten*$^{fl/fl}$;4ebp1^{M}**
Basal	All	1795	2718	1565
	rtTA-eGFP+	255 *(14.2%)*	422 *(15.5%)*	41 *(2.6%)*
Intermediate	All	2391	8230	4760
	rtTA-eGFP+	438 *(18.3%)*	1073 *(13.0%)*	43 *(0.90%)*

Table 1: Transgene abundance in PTEN mouse epithelia

Basal Subset	**Hypo-proliferative**	**Hyper-proliferative**
***Pten*$^{fl/fl}$**	188 *(73.7%)*	60 *(23.5%)*
***Pten*$^{fl/fl}$ cx**	313 *(74.1%)*	98 *(23.2%)*
***Pten*$^{fl/fl}$;4ebp1^{M}**	38 *(97.4%)*	1 *(2.6%)*

Table 2: Basal proliferative subset proportions in *rtTA-eGFP+* cells

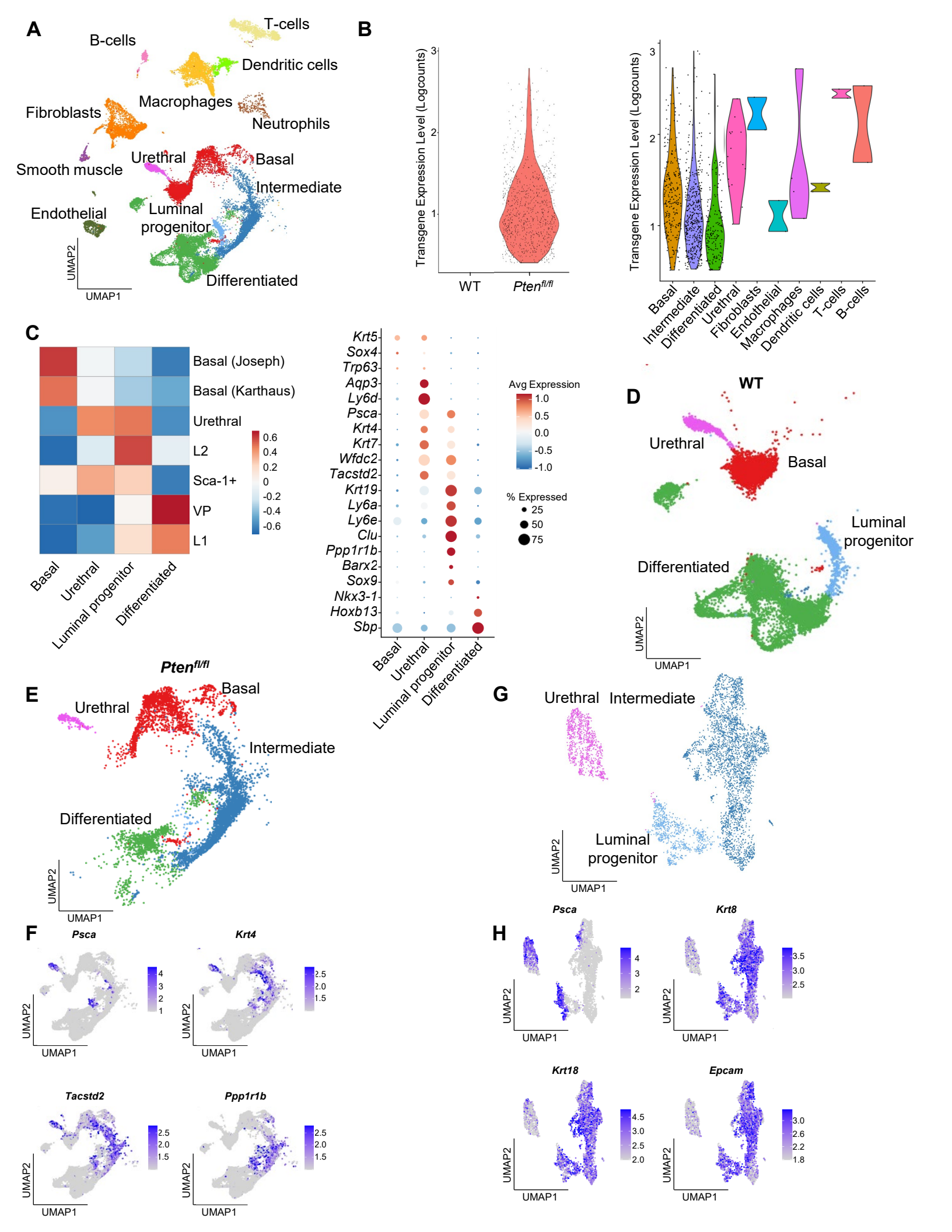
A
T-cells
B-cells
Dendritic cells
Macrophages
Fibroblasts
Neutrophils
Smooth muscle
Urethral
Basal
Intermediate
Endothelial
Luminal progenitor
Differentiated
UMAP2
UMAP1
B
Transgene Expression Level (Logcounts)
WT
Pten fl/fl
Basal
Intermediate
Differentiated
Urethral
Fibroblasts
Endothelial
Macrophages
Dendritic cells
T-cells
B-cells
C
Basal (Joseph)
Basal (Karthaus)
Urethral
L2
Sca-1+
VP
L1
Basal
Urethral
Luminal progenitor
Differentiated
Krt5
Sox4
Trp63
Aqp3
Ly6d
Psca
Krt4
Krt7
Wfdc2
Tacstd2
Krt19
Ly6a
Ly6e
Clu
Ppp1r1b
Barx2
Sox9
Nkx3-1
Hoxb13
Sbp
Avg Expression
% Expressed
D
WT
Urethral
Basal
Luminal progenitor
Differentiated
E
Pten fl/fl
Urethral
Basal
Intermediate
Differentiated
F
Psca
Krt4
Tacstd2
Ppp1r1b
G
Urethral
Intermediate
Luminal progenitor
H
Psca
Krt8
Krt18
Epcam

Figure 2.3.S1: Epithelial Cells Contain Published Subtypes and Urethral Cells

A) UMAP visualization of all cells in WT and *Pten*$^{fl/fl}$ ventral prostates, colored and labeled by cell ID. **B)** Violin plots of *rtTA-eGFP* transgene expression. Left, transgene expression in WT and *Pten*$^{fl/fl}$ mice. Right, expression in *Pten*$^{fl/fl}$ cell types. **C)** Heatmap of composite scores of published prostate epithelial subtype signatures in basal, urethral, luminal progenitor, and differentiated cells in WT mice (left). Dot plot of epithelial biomarker gene expression in WT mice (right). **D)** UMAP visualization of epithelial cells in WT prostates, colored and labeled by cell ID. **E)** UMAP visualization of epithelial cells in *Pten*$^{fl/fl}$ prostates, colored and labeled by cell ID. **F)** UMAP visualization of published intermediate cell biomarkers in WT and *Pten*$^{fl/fl}$ mice. **G)** UMAP visualization of urethral, luminal progenitor, and intermediate cells in WT and *Pten*$^{fl/fl}$ mice, colored and labeled by cell ID. **H)** UMAP visualization of *Psca*, pan-epithelial and luminal biomarkers in urethral, luminal progenitor, and intermediate cells in WT and *Pten*$^{fl/fl}$ mice.

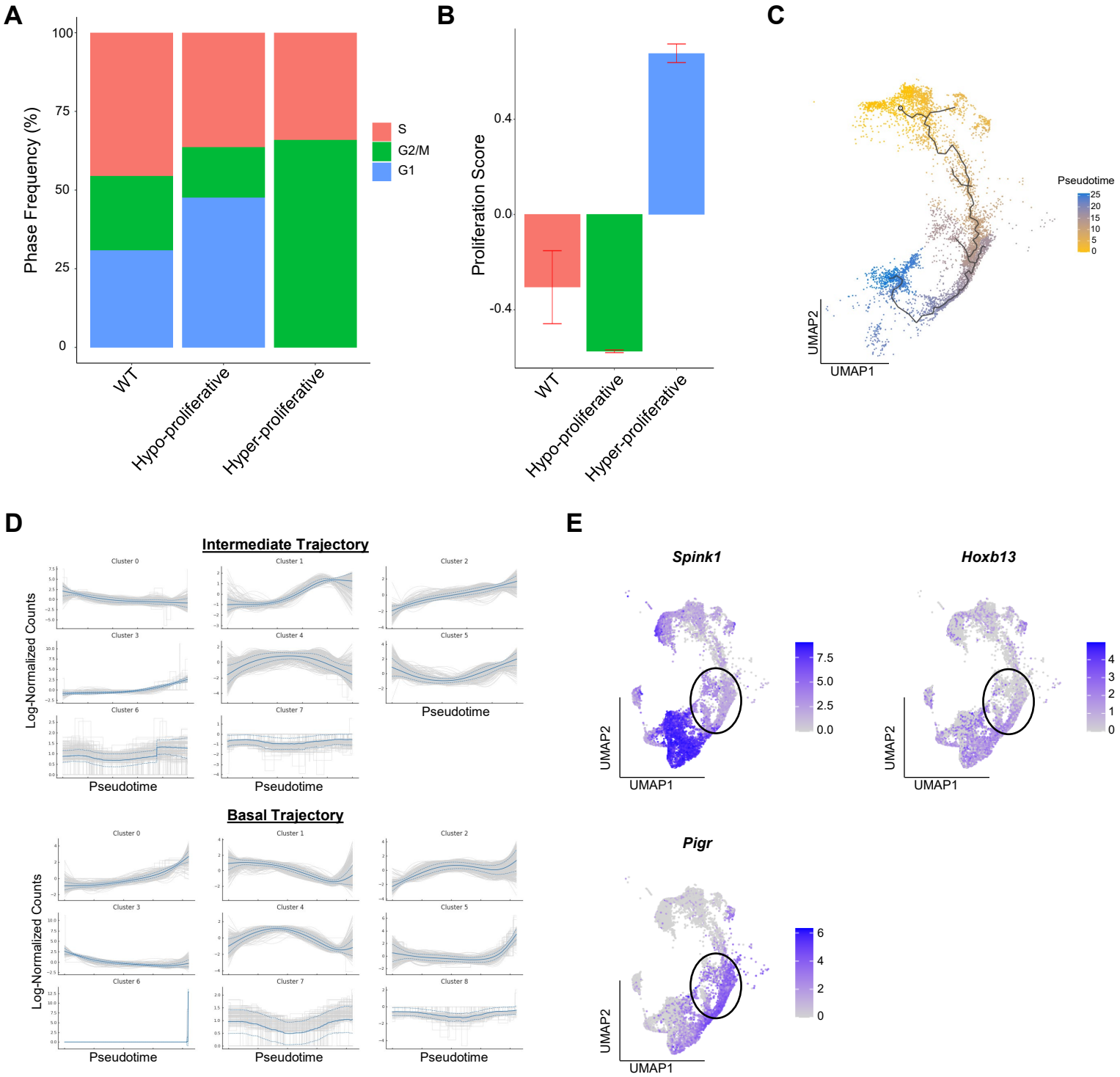
A
Phase Frequency (%)
100
75
50
25
0
S
G2/M
G1
WT
Hypo-proliferative
Hyper-proliferative
B
Proliferation Score
0.4
0.0
-0.4
WT
Hypo-proliferative
Hyper-proliferative
C
Pseudotime
25
20
15
10
5
0
UMAP2
UMAP1
D
Intermediate Trajectory
Log-Normalized Counts
Cluster 0
Cluster 1
Cluster 2
Cluster 3
Cluster 4
Cluster 5
Cluster 6
Cluster 7
Pseudotime
Basal Trajectory
Log-Normalized Counts
Cluster 0
Cluster 1
Cluster 2
Cluster 3
Cluster 4
Cluster 5
Cluster 6
Cluster 7
Cluster 8
Pseudotime
E
Spink1
7.5
5.0
2.5
0.0
UMAP2
UMAP1
Hoxb13
4
3
2
1
0
UMAP2
UMAP1
Pigr
6
4
2
0
UMAP2
UMAP1

Figure 2.3.S2: Basal Proliferation is Subset-Specific and Intermediate Cells Express Luminal Markers

A) Bar plot of cell cycle phase assignments in WT basal cells and *Pten*$^{fl/fl}$ hyper- and hypo-proliferative basal cells. **B)** Bar plot of CCP signature composite score in WT basal cells and *Pten*$^{fl/fl}$ hyper- and hypo-proliferative basal cells (Data presented as +/- SD). **C)** Trajectory analysis of *Pten*$^{fl/fl}$ epithelial cells. **D)** Top 3000 highly variable genes in *Pten*$^{fl/fl}$ basal and intermediate cells, clustered by expression pattern along the basal-intermediate (top) or hypo-proliferative basal-hyper-proliferative basal (bottom) trajectories drawn via Palantir (Figure **1I**). **E)** UMAP visualization of luminal biomarkers in epithelial cells in WT and *Pten*$^{fl/fl}$ mice. Black circles indicate luminal-intermediate transition zone.

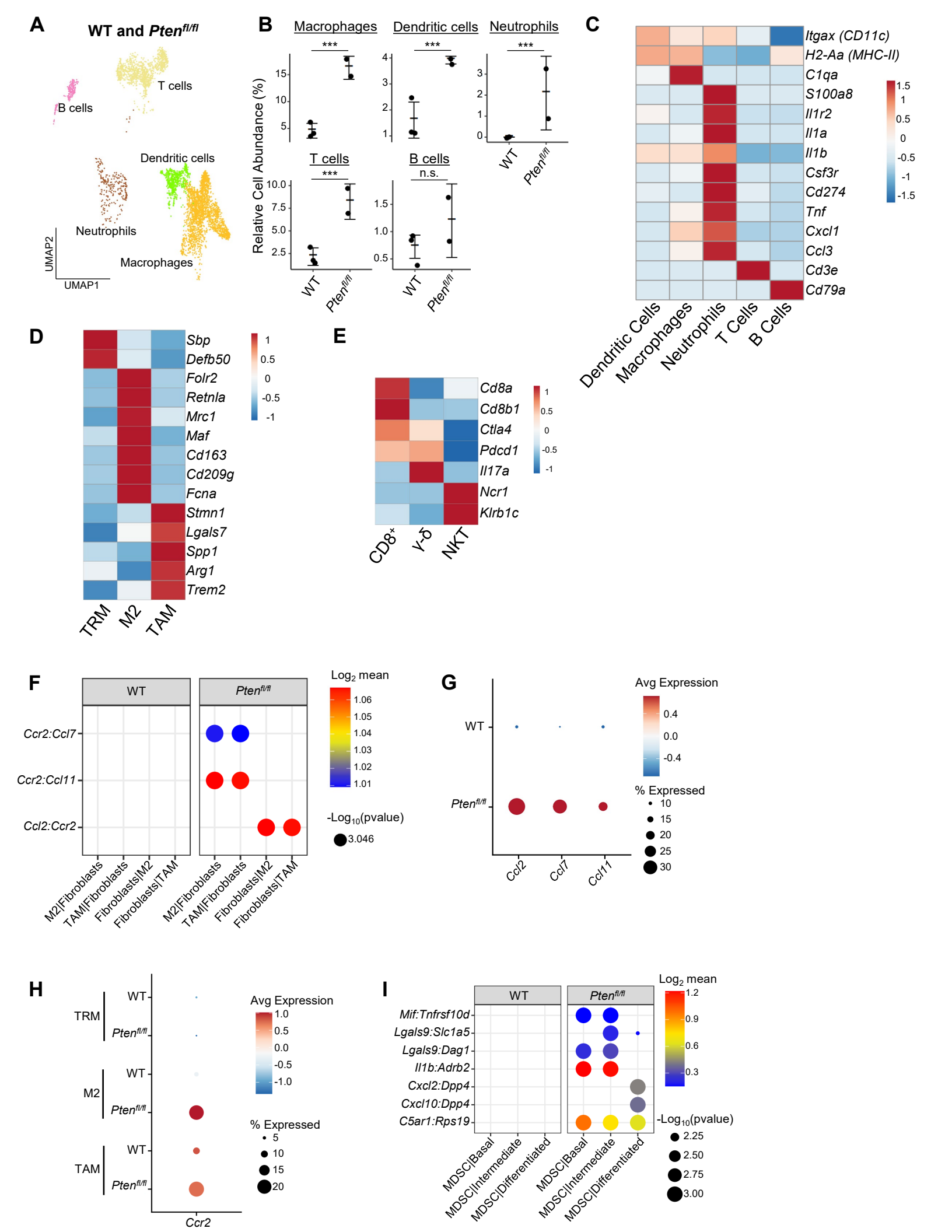
A
WT and Ptenfl/fl
T cells
B cells
Dendritic cells
Neutrophils
Macrophages
UMAP2
UMAP1
B
Macrophages
Dendritic cells
Neutrophils
T cells
B cells
Relative Cell Abundance (%)
***
n.s.
WT
Ptenfl/fl
C
Itgax (CD11c)
H2-Aa (MHC-II)
C1qa
S100a8
Il1r2
Il1a
Il1b
Csf3r
Cd274
Tnf
Cxcl1
Ccl3
Cd3e
Cd79a
Dendritic Cells
Macrophages
Neutrophils
T Cells
B Cells
D
Sbp
Defb50
Folr2
Retnla
Mrc1
Maf
Cd163
Cd209g
Fcna
Stmn1
Lgals7
Spp1
Arg1
Trem2
TRM
M2
TAM
E
Cd8a
Cd8b1
Ctla4
Pdcd1
Il17a
Ncr1
Klrb1c
CD8+
γ-δ
NKT
F
WT
Ptenfl/fl
Ccr2:Ccl7
Ccr2:Ccl11
Ccl2:Ccr2
M2|Fibroblasts
TAM|Fibroblasts
Fibroblasts|M2
Fibroblasts|TAM
Log2 mean
-Log10(pvalue)
3.046
G
WT
Ptenfl/fl
Ccl2
Ccl7
Ccl11
Avg Expression
% Expressed
H
TRM
M2
TAM
WT
Ptenfl/fl
Ccr2
Avg Expression
% Expressed
I
WT
Ptenfl/fl
Mif:Tnfrsf10d
Lgals9:Slc1a5
Lgals9:Dag1
Il1b:Adrb2
Cxcl2:Dpp4
Cxcl10:Dpp4
C5ar1:Rps19
MDSC|Basal
MDSC|Intermediate
MDSC|Differentiated
Log2 mean
-Log10(pvalue)

Figure 2.3.S3: Immune Cells Contain Pro-Tumorigenic Subtypes and Macrophages are Recruited by Fibroblast Signaling

A) UMAP of immune cells in WT and *Pten*$^{fl/fl}$ prostates, labeled by cell types. **B)** Relative abundance of immune cell types in WT and *Pten*$^{fl/fl}$ mice (***p<0.001, n.s. = not significant, negative binomial regression test). **C)** Heatmap of immune cell type biomarker expression in WT and *Pten*$^{fl/fl}$ mice; neutrophil cells express MDSC markers. Log-transformed read counts. **D)** Heatmap of marker expression in macrophage cell subtypes. Log-transformed read counts. **E)** Heatmap of marker expression in T cell subtypes. Log-transformed read counts. **F)** Plot of ligand-receptor interactions between fibroblast and macrophage subtypes. **G)** Dot plot of *Ccr2* ligand expression in fibroblasts in WT and *Pten*$^{fl/fl}$ ventral prostates. **H)** Dot plot of *Ccr2* expression in macrophage subtypes in WT and *Pten*$^{fl/fl}$ ventral prostates. **I)** Dot plot of signaling interactions between epithelial cells and MDSCs.

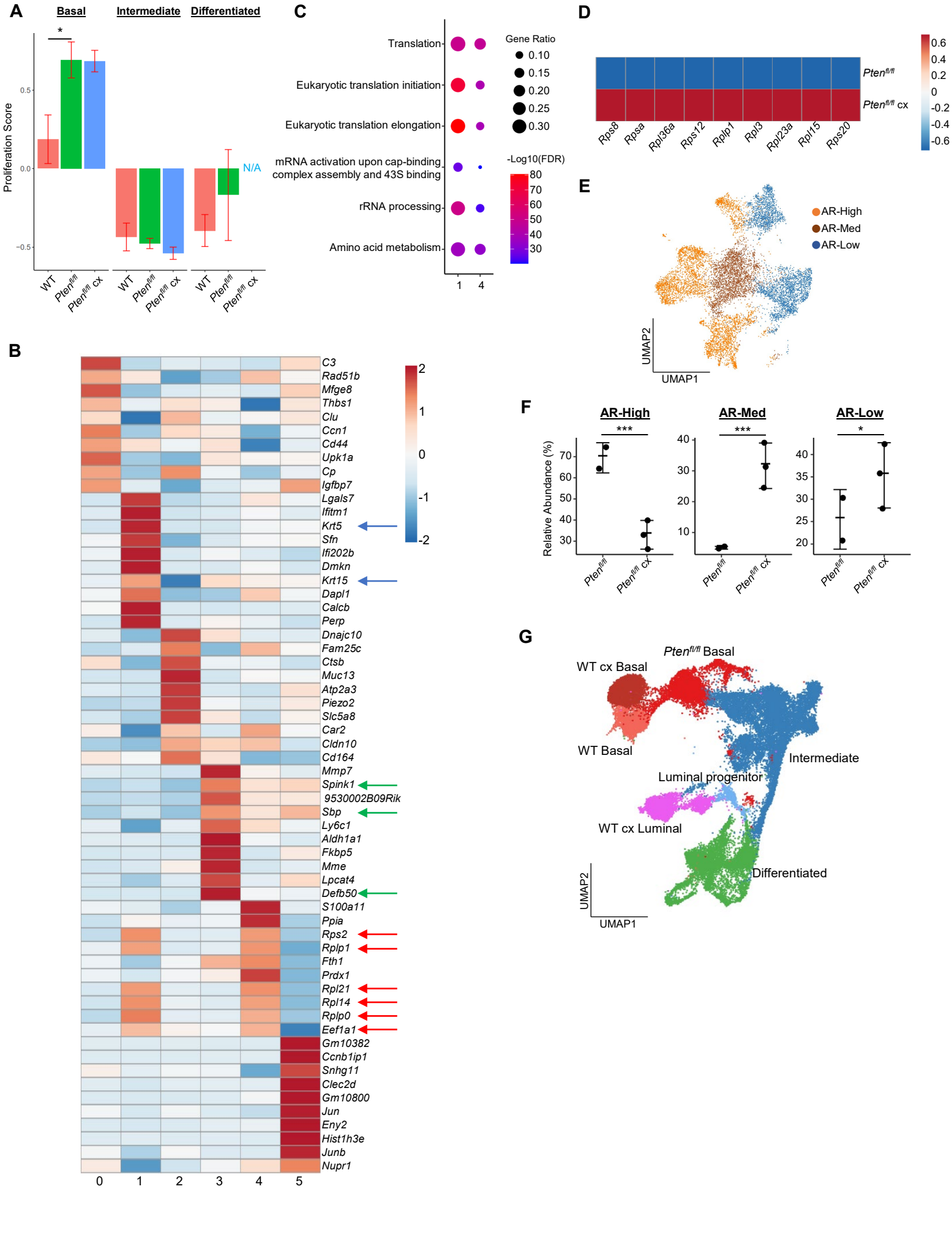
A
Basal
Intermediate
Differentiated
Proliferation Score
N/A
WT
Pten fl/fl
Pten fl/fl cx
B
C3
Rad51b
Mfge8
Thbs1
Clu
Ccn1
Cd44
Upk1a
Cp
Igfbp7
Lgals7
Ifitm1
Krt5
Sfn
Ifi202b
Dmkn
Krt15
Dapl1
Calcb
Perp
Dnajc10
Fam25c
Ctsb
Muc13
Atp2a3
Piezo2
Slc5a8
Car2
Cldn10
Cd164
Mmp7
Spink1
9530002B09Rik
Sbp
Ly6c1
Aldh1a1
Fkbp5
Mme
Lpcat4
Defb50
S100a11
Ppia
Rps2
Rplp1
Fth1
Prdx1
Rpl21
Rpl14
Rplp0
Eef1a1
Gm10382
Ccnb1ip1
Snhg11
Clec2d
Gm10800
Jun
Eny2
Hist1h3e
Junb
Nupr1
0 1 2 3 4 5
C
Translation
Eukaryotic translation initiation
Eukaryotic translation elongation
mRNA activation upon cap-binding complex assembly and 43S binding
rRNA processing
Amino acid metabolism
Gene Ratio
0.10
0.15
0.20
0.25
0.30
-Log10(FDR)
1 4
D
Pten fl/fl
Pten fl/fl cx
Rps8
Rpsa
Rpl36a
Rps12
Rplp1
Rpl3
Rpl23a
Rpl15
Rps20
E
AR-High
AR-Med
AR-Low
UMAP2
UMAP1
F
AR-High
AR-Med
AR-Low
Relative Abundance (%)
G
Pten fl/fl Basal
WT cx Basal
WT Basal
Intermediate
Luminal progenitor
WT cx Luminal
Differentiated
UMAP2
UMAP1

Figure 2.3.S4: Castration-Resistant Intermediate Cells are Phenotypically Diverse

A) Composite score of CCP signature in WT, *Pten*$^{fl/fl}$ intact, and *Pten*$^{fl/fl}$ cx epithelial cells (Data presented as +/- SD, *p<0.05, permutation test) **B)** Heatmap of top differentially expressed genes across intermediate clusters 0-5. Blue arrows, basal markers; green arrows, AR-dependent genes; red arrows, ribosomal or translation machinery genes. **C)** Top GSEA results for genes upregulated in intermediate clusters 1 and 4. All pathways are enriched with FDR < 0.05. **D)** Heatmap of ribosomal gene expression in basal cells in *Pten*$^{fl/fl}$ intact and *Pten*$^{fl/fl}$ cx mice. **E)** UMAP visualization of AR signaling status in intermediate cells in *Pten*$^{fl/fl}$ intact and *Pten*$^{fl/fl}$ cx mice. **F)** Relative abundance of intermediate cells with high, medium, or low AR signaling in *Pten*$^{fl/fl}$ intact and *Pten*$^{fl/fl}$ cx mice (Data presented as +/- SD, *p<0.05, ***p<0.001, negative binomial regression test). **G)** UMAP visualization of epithelial cells in WT intact, WT cx, *Pten*$^{fl/fl}$ intact, and *Pten*$^{fl/fl}$ cx mice, colored and labeled by cell ID.

A

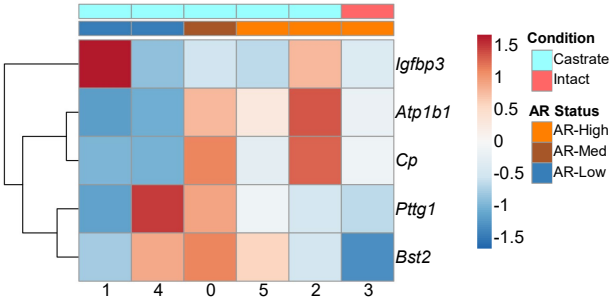
Igfbp3
Atp1b1
Cp
Pttg1
Bst2
1 4 0 5 2 3
1.5
1
0.5
0
-0.5
-1
-1.5
Condition
Castrate
Intact
AR Status
AR-High
AR-Med
AR-Low

B

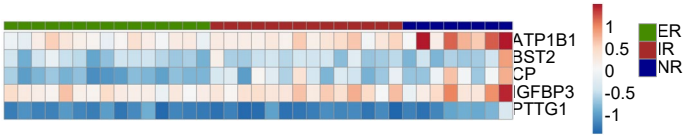
ATP1B1
BST2
CP
IGFBP3
PTTG1
1
0.5
0
-0.5
-1
ER
IR
NR

C

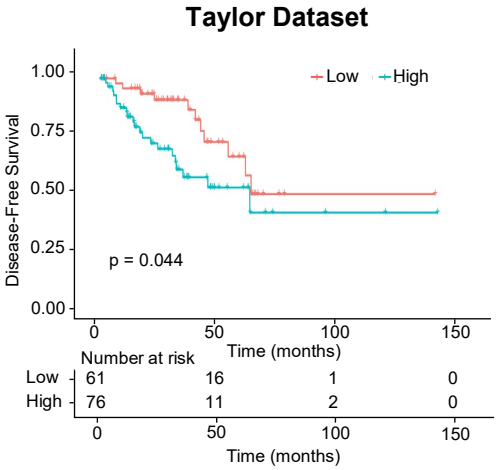
Taylor Dataset
Low
High
Disease-Free Survival
1.00
0.75
0.50
0.25
0.00
p = 0.044
0
50
100
150
Time (months)
Number at risk
Low 61 16 1 0
High 76 11 2 0
Time (months)

D

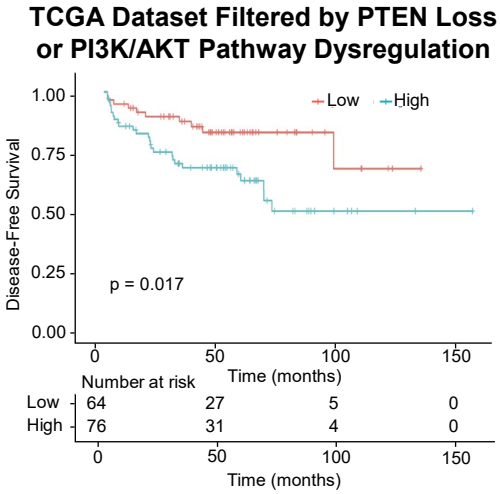
TCGA Dataset Filtered by PTEN Loss or PI3K/AKT Pathway Dysregulation
Low
High
Disease-Free Survival
1.00
0.75
0.50
0.25
0.00
p = 0.017
0
50
100
150
Time (months)
Number at risk
Low 64 27 5 0
High 76 31 4 0
Time (months)

Figure 2.3.S5: 5 Genes Expressed in Intermediate Cells Correlate with Poor Disease outcomes in Human Patients

A) Heatmap of top 5 resistance genes in intermediate clusters, labeled by AR status and condition (intact or castrate). **B)** Heatmap of the top 5 genes enriched in castrated intermediate cells (Fig. 4B) and their expression in ADT non-responder (NR), intermediate responder (IR), and excellent responder (ER) patients. **C)** Kaplan-Meier curve of disease-free survival of patients in the Taylor et al. (2010) cohort, separated by expression of the top 5 resistance genes in castrated intermediate cells. Red line, normal expression of top 5 genes; blue line, patients with expression of at least 1 gene with TPM in the 80^{th} percentile or above. **D)** Kaplan-Meier curve of disease-free survival of patients in the TCGA database, filtered for PTEN loss or PI3K/AKT pathway dysregulation, separated by expression of the top 5 resistance genes in castrated intermediate cells. Red line, normal expression of top 5 genes; blue line, patients with expression of at least 1 gene with TPM (transcripts per million) in the 80^{th} percentile or above.

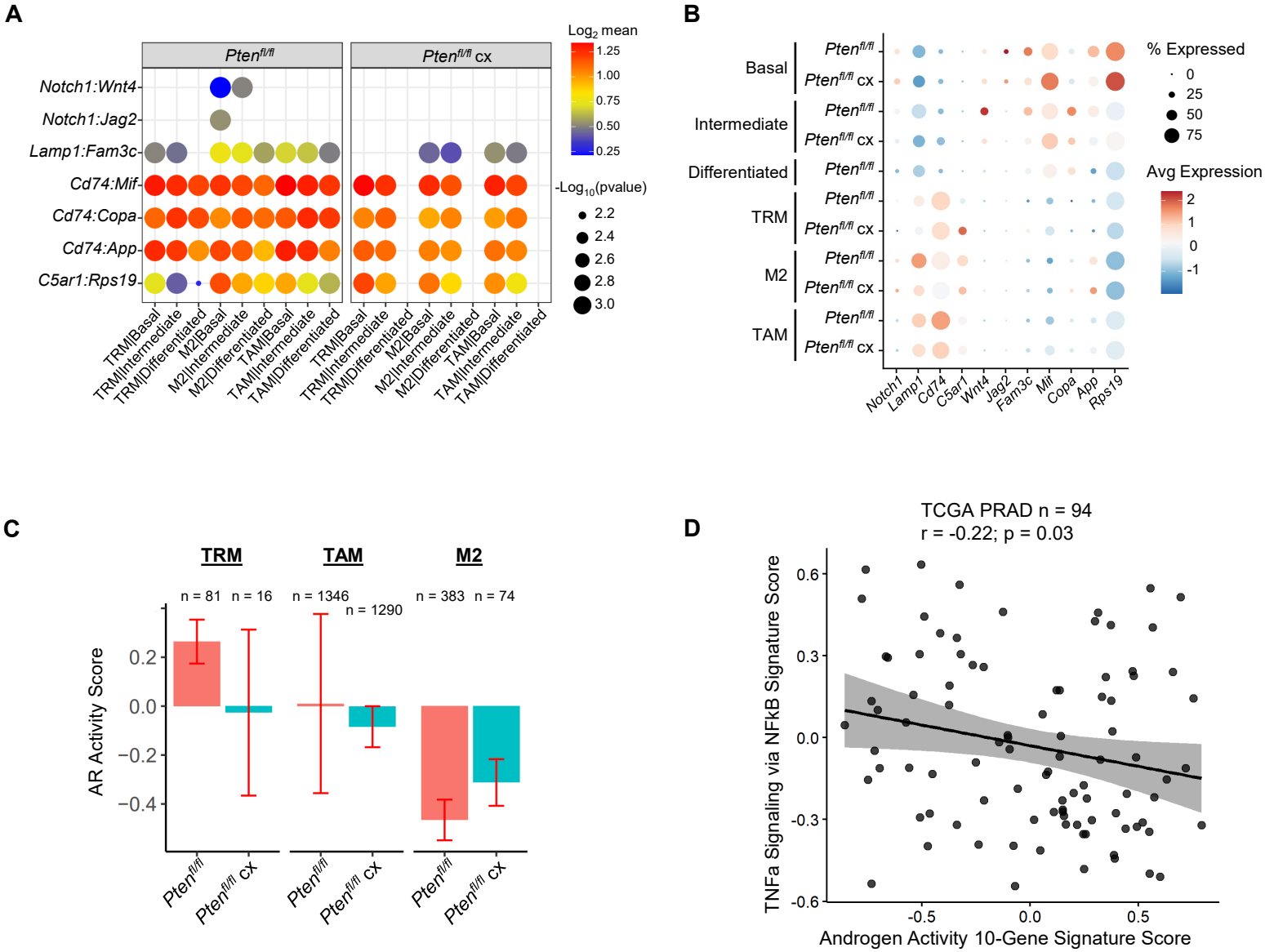
A
Pten fl/fl
Pten fl/fl cx
Notch1:Wnt4
Notch1:Jag2
Lamp1:Fam3c
Cd74:Mif
Cd74:Copa
Cd74:App
C5ar1:Rps19
Log2 mean
1.25
1.00
0.75
0.50
0.25
-Log10(pvalue)
2.2
2.4
2.6
2.8
3.0
TRM|Basal
TRM|Intermediate
TRM|Differentiated
M2|Basal
M2|Intermediate
M2|Differentiated
TAM|Basal
TAM|Intermediate
TAM|Differentiated
B
Basal
Intermediate
Differentiated
TRM
M2
TAM
% Expressed
0
25
50
75
Avg Expression
2
1
0
-1
Notch1
Lamp1
Cd74
C5ar1
Wnt4
Jag2
Fam3c
Mif
Copa
App
Rps19
C
TRM
TAM
M2
n = 81
n = 16
n = 1346
n = 1290
n = 383
n = 74
AR Activity Score
0.2
0.0
−0.2
−0.4
D
TCGA PRAD n = 94
r = -0.22; p = 0.03
TNFa Signaling via NFkB Signature Score
0.6
0.3
0.0
-0.3
-0.6
-0.5
0.0
0.5
Androgen Activity 10-Gene Signature Score

Figure 2.3.S6: Epithelial-Mediated Macrophage Recruitment is not Interrupted by Castration

A) Plot of signaling interactions between macrophage subtypes and epithelial cells in *Pten*$^{fl/fl}$ intact and *Pten*$^{fl/fl}$ cx prostates. **B)** Dot plot of epithelial ligand and macrophage receptor gene expression in *Pten*$^{fl/fl}$ intact and *Pten*$^{fl/fl}$ cx ventral prostates. **C)** Composite score of AR signaling signature in macrophage subtypes in *Pten*$^{fl/fl}$ intact and *Pten*$^{fl/fl}$ cx prostates (Data presented as +/- SD). **D)** Scatter plot of TCGA PRAD study patient signature composite scores, filtered for patients harboring PTEN mutations. Y-axis, TNF signaling signature score; X-axis, AR signaling signature score (Pearson's correlation).

FRED HUTCH
CURES START HERE™

Defining cellular population dynamics at single cell resolution during prostate cancer progression

Advanced prostate cancer is a leading cause of malignancy-related deaths in men, in large part due to our poor understanding of advanced castration-resistant prostate cancer (CRPC). Of particular interest is CRPC lacking androgen receptor (AR) activity, or AR-low CRPC, which is uniformly lethal. While many studies have identified a complex cellular architecture in the prostate, we still lack a unified view of the cellular interactions and phenotypes that facilitate advanced prostate cancer initiation, maintenance, and survival, particularly without AR signaling. To better understand the cellular changes that drive CRPC, we have generated single-cell RNA sequencing data from mouse ventral prostates under multiple normal and cancer conditions (Pten loss [$Pten^{fl/fl}$]), and Pten loss with castration [$Pten^{fl/fl}$ cx]), resulting in 50,780 cells from 10 mice. We identified 12 cell types and 16 cellular activation states in our dataset and were able to delineate the influence of tumorigenesis and androgen deprivation on these populations. Our findings reveal a subset of the epithelial compartment that is primed for AR-low survival during tumorigenesis, as well as a complex picture of lineage plasticity to facilitate expansion of this subtype. Castration confirms this cell type's role in conferring resistance to androgen deprivation and adverse clinical outcomes and broadly remodels the epithelial compartment. In addition, we observe a dramatic increase in immune cell population upon transformation. We identify this immune influx as pro-tumorigenic and employ a novel ligand-receptor database and prediction software to pinpoint unique signaling phenotypes from individual epithelial subtypes, demonstrating a multifaceted process of immune recruitment and remodeling by the tumor. Androgen signaling is crucial for maintaining immune populations; castration dramatically remodels the tumor environment and activates major pro-tumorigenic signaling pathways. Finally, we uncover the importance of protein synthesis regulation in maintaining these complex mechanisms via the $Pten^{fl/fl}$ cx mouse model, in which we can toggle a genetic inhibitor of translation ($Pten^{fl/fl}$;4ebp1M). These findings shed new light on the cellular dynamics of prostate cancer evolution and highlight the importance of employing high-throughput technologies to provide a complete picture of tumors and their microenvironments. Here, we provide access to our dataset through an interactive portal enabling gene- and cell-specific comparisons between all conditions tested in Germanos et al. In revision.

Read Paper on BioRxiv

Compare Wild Type Vs Pten Intact In Basal Cells

Relative Basal Cell Abundance (%)

Differentially Expressed Genes in Basal Cells (Wild Type Vs PTEN Intact)

FILTERS COLUMNS DENSITY EXPORT

Gene	Log2 FC	P-Value	P-Value Adj	FDR	PC1	PC2
Tacstd2	1.1077	0.0000	0.0000	0.0000	0.5250	0.0810
Ifi202b	1.8286	0.0000	0.0000	0.0000	0.3090	0.0010
Serinc2	0.8756	0.0000	0.0000	0.0000	0.4170	0.0380
Tbc1d1	0.9929	0.0000	0.0000	0.0000	0.3630	0.0200
4930523C07Rik	1.0471	0.0000	0.0000	0.0000	0.5140	0.0810
Col17a1	0.9519	0.0000	0.0000	0.0000	0.4450	0.0500
Psmb8	1.0175	0.0000	0.0000	0.0000	0.3780	0.0270
Prelid1	0.9271	0.0000	0.0000	0.0000	0.6950	0.1680
Fth1	-0.9070	0.0000	0.0000	0.0000	0.9730	0.9640
Pdlim1	0.8384	0.0000	0.0000	0.0000	0.4860	0.0760

Rows per page: 100 1–100 of 1307

Click on Row Above To Color UMAP Based On Gene Expression

Wild Type (Left) Vs PTEN Intact (Right)

Color by Gene Expression | CELL STATES | CELL TYPES | PHASE

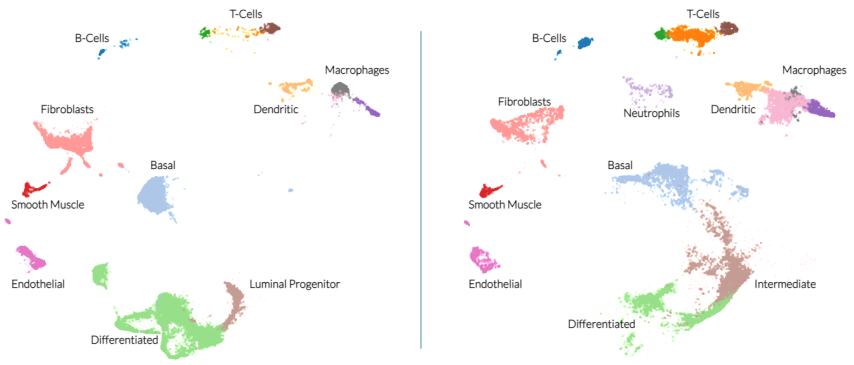

Basal CD8 Dendritic Gamma-Delta Differentiated Smooth Muscle Fibroblast M2 Neutrophils NKT Luminal Progenitor / Intermediate Endothelial TAM

Figure 2.3.S7: Interactive Portal, Enabling Gene- and Cell- Specific Comparisons Across the Spectrum of Prostate Cancer Initiation and Progression *in vivo*.

Interactive website can be found at https://atlas.fredhutch.org/hsieh-prostate/

2.6 Methods

2.6.1 Mice

PB-Cre4 mice which express a *Cre* recombinase transgene under the control of the rat *Pbsn* (probasin) promoter in the prostate epithelium were obtained from the Mouse Models of Human Cancer Consortium (now Jax #026662). *Pten*$^{fl/fl}$ (Jax #006440) and *Rosa-LSL-rtTA* (Jax #005670) mice were obtained from the Jackson Laboratory. *TetO*-4ebp1^{M} mice which express an inducible mutant *Eif4ebp1* transgene were generated as previously described (Hsieh et al., 2010). All mice were maintained in the C57BL/6 background under specific pathogen–free conditions, and experiments conformed to the guidelines as approved by the Institutional Animal Care and Use Committee of Fred Hutchinson Cancer Research Center.

2.6.2 Surgical castration and activation of the 4EBP1^{M} transgene

Surgical castrations were performed in 4- to 5-month-old mice under isoflurane anesthesia. Postoperatively, mice were monitored daily for 5 days. To activate the 4EBP1^{M} transgene, doxycycline (Sigma-Aldrich) was administered in the drinking water at 2 g/liter immediately after castration, and euthanasia was performed 8 weeks after castration.

2.6.3 Tissue dissociation for single-cell RNA sequencing

Ventral prostate lobes from C57BL/6 J WT, *Pten*$^{fl/fl}$*, Pten*$^{fl/fl}$*;*4ebp1^{M} mice were dissected, washed with chilled 1 X PBS, and then minced with a scalpel into small pieces (~1 mm) in a petri dish. Paired lobes from a single mouse were collected and dissociated into one sample for scRNA-seq. The tissue was digested with DMEM/F12/Collagenase/Hyaluronidase/FBS (StemCell technologies, Vancouver, Canada) for 1 hr at 37 °C on a slowly shaking/rotating platform. The tissue was further digested in 0.25% Trypsin-EDTA (Invitrogen, Carlsbad, CA) on ice for 30 minutes, and followed by suspension in Dispase (Invitrogen, Carlsbad, CA, 5 mg/mL) and DNase I (Roche Applied Science, Indianapolis, IN, 1 mg/mL). Any cell clumps were dissociated by gently pipetting up and down. The dissociated cells were then passed through 70 μm cell strainers (BD Biosciences, San Jose, CA) to achieve single cell suspension. The suspension was resuspended with 3 ml PBS (Life Technologies) with 2% fetal calf serum (FCS) (Gemini Bioproducts, West Sacramento, CA) and immediately placed on ice. Viable cells were counted by Vi-Cell XR Cell Viability Analyzer (Beckman Coulter, Brea, CA) and then diluted accordingly to reach the targeted cell concentration.

2.6.4 Single-cell RNA sequencing library preparation

3’ single-cell RNA libraries were generated according to the protocol outlined in Single Cell 3’ Reagent Kits v2 User Guide 10 X Genomics. Briefly, cells and reverse transcription reagents were

partitioned into oil-based Gel Beads in Emulsion (GEMs), with each GEM containing a unique 10 x barcode. Cells were then lysed and underwent reverse transcription resulting in barcoded cDNA. The cDNA was then collected and amplified prior to undergoing library construction in which P5, P7, and a unique sample index were added.

At least two mouse prostates were prepared and sequenced for each condition in order to obtain >10,000 cells/condition, resulting in n=3 for WT mice, n=2 for *Pten*$^{fl/fl}$ mice, n=3 for *Pten*$^{fl/fl}$ mice, and n=2 for *Pten*$^{fl/fl}$*;*4ebp1^{M} mice. Individual mouse prostates were considered biological replicates. The 10 libraries generated in this manner were pooled and sequencing was performed on an Illumina NovaSeq 6000 using the v1.5 S1-100 flow cell and reagent kit. Sequencing configuration was paired-end 26x8 × 96 and Illumina RTA version v3.3.5 was used. This generated a median of 58.7 million reads/sample with a median 54.60% saturation, median 90.70% Q30 fraction, 13,746 average reads/cell, and 6.2 reads/UMI.

2.6.5 Alignment and filtering of reads

Two transgene transcripts (*Cre*, *rtTA-eGFP*) were added to the mm10 transcriptome to detect transgenes expressed in the *Pten*$^{fl/fl}$ and *Pten*$^{fl/fl}$*;*4ebp1^{M} mice. Kallisto v0.45.1 (Bray et al., 2016) was used to demultiplex all samples into FASTQ files and align reads to the modified mm10 transcriptome. DropletUtils package (Lun et al., 2019; Griffiths et al., 2018) was used to filter out empty or duplexed cell droplets. Cells with fewer than 200 or greater than 5000 detected genes, fewer than 500 or greater than 25,000 detected UMIs and cells with >15% mitochondrial reads were filtered from subsequent analysis.

2.6.6 PCA, UMAP, and clustering

R package Seurat v4.0.4 (https://satijalab.org/seurat/) was used to construct a Principal Component Analysis (PCA) for the entire dataset using the 2000 most variable genes as features. The Uniform Manifold Approximation and Projection (UMAP) dimension reduction technique was used for visualization and the R function ‘FindClusters()’ with resolution = 0.2 was used to generate 43 clusters.

2.6.7 Cell type identification

The SingleR package v1.6.1 was used to assign initial cell type identities to each cluster. These IDs were verified and refined using expression patterns of published biomarkers. For epithelial cells, cell subtypes (basal, intermediate, differentiated) were assigned using published gene signatures from other single-cell RNA sequencing projects. For immune cells, broad cell types (T cells, macrophages) were divided into activation states via known biomarkers (e.g. *Cd8a* for CD8 T cells and *Mrc1* for M2-activated macrophages). Stromal cell types were also determined via biomarkers.

2.6.8 Relative cell abundance

To compare the abundance of specific cell populations while controlling for sample library size, the percentage composition of each sample was calculated by cell type. Statistical significance was generated via a negative binomial regression test to determine whether a given cell type was over- or under-represented between conditions.

2.6.9 Gene signature enrichment

The GSVA package v1.40.1 (Hänzelmann et al., 2013) was used to generate composite scores for gene signatures such as a 20-gene AR activity signature or the 30-gene CCP proliferation signature. Due to the sparse nature of single-cell transcriptomes, the data was pseudo-bulked by sample and cell type to generate more robust analyses. Statistical analysis was performed via permutation test with 10,000 permutations.

2.6.10 Differential expression and gene set enrichment analysis

Differential gene expression was computed using Seurat functions with a threshold log2 fold-change >0.25 or<–0.25 and FDR <0.05. Upregulated and downregulated genes were further filtered by setting a log2 fold-change threshold = log2(1.25) = ~0.32. Gene names were converted from mouse to human via the biomaRt package (Durinck et al., 2009) and GSEA was performed using the MsigDB database with the C2, C5, C6, C7, Hallmark, KEGG, BioCarta, and Reactome gene sets. Resulting enriched pathways were filtered via a threshold of FDR <0.05.

2.6.11 Trajectory, RNA velocity, and pseudotime

Monocle3 (Cao et al., 2019; Qiu et al., 2017; Trapnell et al., 2014) and velocyto (La Manno et al., 2018) were used to draw trajectory paths and RNA velocity maps, respectively, through the epithelial compartment of the *Pten*$^{fl/fl}$ intact mice. Palantir (Setty et al., 2019) was used to delineate gene expression dynamics across pseudotime in basal and intermediate cells in *Pten*$^{fl/fl}$ intact mice.

2.6.12 Ligand-receptor interactions

Ligand-receptor interactions between cell types were determined via the CellphoneDB package v2.0.0 (Efremova et al., 2020). Only interaction with p-value <0.05 were included in the final analysis.

2.6.13 Cell cycle assignment

Cell cycle phases for single cells were determined using the Seurat cell cycle function, which includes gene lists denoting the G2M and S phases. Gene names were converted from human to mouse using the biomaRt package to match our data, then the CellCycleScoring function was used to

assign each cell either S, G2M, or G1 phase. Chi-squared test was used to determine whether the proportions of G1 cells were significantly different between clusters or conditions.

2.6.14 Human gene signature of ADT resistance and correlation to mouse data

Tumor samples were laser capture microdissected from prostate cancer biopsies prior to undergoing six months of neoadjuvant androgen deprivation therapy plus enzalutamide and ranked based on volume of residual tumor in each patient, as previously described (Karzai et al., 2021; Wilkinson et al., 2021; Ku et al., 2021). Separately, differentially expressed genes (DEGs) derived from the PTEN null intact and castrate basal or intermediate cells were converted from mouse to human gene symbols using getLDS function from the biomaRt package v2.48.3 for R/Bioconductor (Durinck et al., 2009). Gene set enrichment analysis (GSEA) was performed on the basal vs. intermediate DEGs set against the top 50 genes associated with treatment resistance, and the top five leading edge genes from GSEA were used to stratify samples. Survival analysis was performed using the *survival* package in R on the TCGA prostate adenocarcinoma (Network, 2015) (n=490) and MSKCC (Taylor et al., 2010) (n=140) datasets. A cancer sample was considered “altered” if the expression of at least one of the five leading edge genes was greater than the 80th percentile for the entire cohort (TCGA or MSKCC, respectively).

2.6.15 Integration of single-cell data from human patients

Sequencing data from human primary tumor samples was contributed by Dr. Franklin Huang. Data from human metastatic tumor samples was obtained from the GEO repository of Dong et al., 2020. All primary and metastatic samples were processed individually via the standard Seurat workflow. The primary sample object was filtered to only retain confirmed malignant cells. All objects were integrated into a Seurat object using a standard workflow (available here) and visualized via the UMAP dimension reduction method. The AddModuleScore function was used to compute the 5-gene signature score for every cell and was visualized via the FeaturePlot function.

2.6.16 Orthogonal mouse model

Data from individual *Pten*$^{-/-}$*/Rb1*$^{-/-}$ (PR) and *Pten*$^{-/-}$*/Rb1*$^{-/-}$*/Nmyc*$^{+}$ (PRN) mice were aggregated using the cellranger aggr pipeline and visualized using Loupe Cell Browser. Quantification of gene expression signatures was performed using the sum of log 2 -transformed normalized UMI counts across all genes in the signature. Cells were stratified into equal-sized tertiles (low, intermediate, high) based on the maximum value of the signature score. Cells with no detectable UMI counts of any signature genes were assigned to the zero category.

2.6.17 TCGA analysis of TNF activity

The Cancer Genome Atlas (TCGA) PRAD cohort containing 493 primary prostate tumor samples with RNA-seq expression values was utilized for analysis of signature scores. We used the RSEM values hosted by the cBioPortal (http://www.cbioportal.org, study: prad_tcga_pan_can_atlas_2018.) Single sample enrichment scores were calculated using GSVA (Hänzelmann et al., 2013) with default parameters using genome-wide log2 RSEM values as input. The pathways used were from MSigDBv7.4 (HALLMARK_TNFA_SIGNALING_VIA_NFKB) and the 10-gene androgen-regulated (AR) signature from Bluemn et al., 2017. In analyses restricted to samples with PTEN biallelic loss, 94 samples were used which had either 2 copy loss or 1 copy loss and a non-synonymous mutation annotated as a putative driver mutation in cBioPortal. Pearson's correlation coefficient was used to study the relationships between signature scores shown in scatterplots using the cor.test function in R.

2.6.18 Data and code availability

The single-cell RNA sequencing data files are available on the GEO database at GSE171336 and can be accessed using token: ijmfokccrhepvub. The code used to process and analyze the data is available at https://github.com/sonali-bioc/GermanosProstatescRNASeq/, (copy archived at swh:1:rev:5a376d7b77d034e9bd09ce4787337ee33fda8448; Arora, 2022). All other data associated with this study are present in supplementary materials and tables.

2.6.19 Interactive website

The web-based data Atlas was developed utilizing open-source technologies, including React for the application framework, Material UI for interface components, and Apache EChart for visualizations. All data were extracted from Seurat HDF5 files into web-optimized CSV, Arrow, and Binary files. All site data and assets are stored in Amazon S3 and served through Amazon CloudFront, a global content delivery network (CDN) service built for high-speed, low-latency performance and security. The site is hosted at https://atlas.fredhutch.org/hsieh-prostate/.

2.7 Acknowledgments

We are grateful to the patients who participated in this study and their families. We thank members of the ACH laboratory for helpful advice and discussions. We thank the Seattle RNA Metabolism group for critical discussion of the work. We thank L Xin for sharing RNA-seq data and critical reading of the manuscript. This work was supported by NIH award R37 CA230617, R01 GM135362, the Pacific Northwest Prostate Cancer SPORE DRP (P50 CA097186), Burroughs Welcome Fund, Career Award for Medicine Scientists (1012314.02), and grants from the Emerson Collective (691630), and the Robert J Kleberg Jr. and Helen C Kleberg Foundation to ACH. AAG

received funding through an NIH T32 grant (T32 CA080416) and ETG reviewed funding from the DoD BCRP Breakthrough Fellowship Award (W81XWH-19-1-0076). This research was also supported by P01 CA163227 and R01 CA234715 to PSN, the Prostate Cancer Foundation, the Genomics and Bioinformatics Shared Resource of the Fred Hutch/University of Washington Cancer Consortium (P30 CA015704) and the Scientific Computing Infrastructure at Fred Hutch funded by ORIP grant S10 OD028685.

Chapter 3. A G-Rich Sequence Motif in 5’ UTRs Sensitizes mRNAs to eIF4F-Mediated Regulation of Translation Initiation

3.1 Introduction

Prostate cancer is the second leading cause of cancer-related death in men (Siegel et al., 2021), thus improving treatment options remains a primary concern for the field. While ADT is highly effective in decreasing tumor burden in advanced prostate cancer patients, resistance and recurrence are inevitable over the long term and lead to incurable castration-resistant prostate cancer (CRPC) (Watson et al., 2015; Labrecque et al., 2019). The relatively recent adoption of AR inhibitors (ARIs) in the clinic has improved therapeutic suppression of the androgen signaling pathway and has proven effective in extending patient survival (de Bono et al., 2011; Scher et al., 2012). However, this has coincided with a rising incidence of cancers that eschew androgen signaling altogether, possibly due to evolutionary pressure applied by more comprehensive inhibition of AR signaling and function over the past decade (Bluemn et al., 2017). Androgen hormone signaling is considered essential for prostate development and homeostasis, as well as prostate cancer progression (Dai et al., 2017). Thus, these AR-low or AR-null cancer subtypes, which are entirely resistant to ADT and ARI approaches, offer a puzzling and concerning problem for the field.

In particular, there is an urgent need to characterize how AR-low prostate cancer can survive and progress without androgen hormone signaling. Understanding whether alternate molecular pathways are activated to compensate for this loss is crucial question that may uncover new therapeutic vulnerabilities. Recent studies have found that one such pathway may be translation initiation, as AR loss leads to eIF4F hyperactivity in a mouse model of prostate cancer (Liu et al., 2019). Other work has described a role for high translation rates in castration-resistant epithelial cell states that may contribute to disease aggressiveness and treatment outcomes and confirms that AR-low prostate cancer is dependent on high eIF4F activity (Germanos et al., 2022).

Aberrant protein synthesis is a hallmark of many diseases (Tahmasebi et al., 2018; Hsieh et al., 2010; Cai et al., 2020; Lim et al., 2021). Translation initiation, canonically modulated by the eIF4F translation initiation complex, controls this crucial aspect of cellular function and is frequently dysregulated in cancer and other diseases (Schuster et al., 2019; Hsieh et al., 2012; Hsieh et al., 2015). While previous studies have shed light on the requirement for high translation initiation to maintain aggressive AR-low prostate cancer, questions remain around the precise factors regulated by this phenotype, and the molecular mechanisms by which given genes are targeted. In this work, we show that a specific subset of the translatome is upregulated in AR-low prostate cancer in mice, and that a G-rich motif is enriched in the 5’ UTRs of these mRNAs. We validate the functionality of this

motif, establish its relevance in another mouse model of cancer, and show that it is conserved and functional in humans. Finally, we propose that the motif regulates translation by generating specific RNA structures that may serve as binding sites for RNA-binding proteins, and thus facilitate interactions with the eIF4F complex. Finally, we generate stable reporter lines as a tool for future mechanistic experiments.

3.2 Results

To investigate the effects of eIF4F hyperactivity in AR-low prostate cancer, we performed ribosome profiling on intact and castrate *Pten*$^{fl/fl}$ mice. We found that 697 mRNAs were translationally upregulated in the prostates of castrate mice, suggesting that increased translation initiation driven by loss of 4EBP1 specifically targets a subset of the transcriptome (Fig. 3.4.1A) (Liu et al., 2019).

We hypothesized this may be due to a shared sequence motif that could mediate interactions between the mRNA and the eIF4F complex. 5' UTRs are a major source of regulatory sequences important for translation (Schuster et al., 2019). As a result, we conducted a *de novo* motif search on the 5' UTR sequences of upregulated genes (Fig. 3.4.1B). Strikingly, we found exactly one motif enriched in upregulated 5' UTRs compared to all 5' UTRs in the mouse genome (Fig. 3.4.1C). We named this motif Guanine-Rich Translational Element (GRTE). To validate whether this sequence motif was functional and whether it is able to mediate translational regulation by eIF4F, we generated an inducible 4EBP1 mutant (4EBP1^{M}) transgene in PC3 prostate cancer cells (PC3-4EBP1^{M}). These cells are derived from metastatic CRPC and are AR-low, recreating the molecular conditions of the castrate *Pten*$^{fl/fl}$ mouse (Liu et al., 2019). The 4EBP1^{M} transgene is a doxycycline-inducible 4EBP1 allele with mutated phosphosites, making it insensitive to inactivation via mTORC1-mediated phosphorylation (Fig. 3.4.1.D). 4EBP1 expression inhibits eIF4F activity, allowing us to modulate translation initiation rates in this system.

We used this cell line to perform reporter assays to test whether 5' UTRs of upregulated genes containing GRTE motifs functionally regulated translation in an eIF4F-dependent manner. We chose *Klf5* and *Denr* as candidate genes. *Klf5* is a transcription factor implicated in breast and other cancers and proliferation (Chen et al., 2006; Nandan et al., 2008; Jia et al., 2016), and contains three GRTE motifs in its 5' UTR, whereas *Denr* is a translation reinitiation factor also associated with multiple cancers (Schleich et a., 2014) and contains one GRTE motif. Both genes were found to be translationally upregulated in AR-low *Pten*$^{fl/fl}$ mice. We inserted the 5' UTRs of both *Klf5* and *Denr* into a pGL3 reporter plasmid. This plasmid expresses the Firefly luciferase (*Fluc*) gene behind the SV40 viral promoter. We generated two reporter constructs for each gene: one construct contained the WT 5' UTR inserted between the SV40 promoter and the *Fluc* gene, and one with all GRTE motifs deleted from the

5’ UTR. We transfected these constructs into PC3-4EBP1^{M} cells with or without doxycycline, measured *Fluc* output via luminescence intensity, and normalized to RNA level via qPCR to examine differences in translation efficiency. We found that for both *Klf5* and *Denr*, the WT 5’ UTR construct resulted in much higher translation than the control vector with no inserted 5’ UTR. In addition, both WT constructs were highly sensitive to eIF4F activity, as inducing 4EBP1^{M} expression significantly decreased translation of these reporter constructs. Finally, deleting the GRTE motifs from both 5’ UTRs resulted in a striking decrease of both translation level and eIF4F sensitivity (Fig. 3.4.1E-F). These results confirmed that the GRTE is functional and mediates translation regulation by eIF4F in *Klf5* and *Denr*.

Translation regulation is dysregulated in multiple disease contexts, and initiation is a crucial regulatory step in proper translation. Finding that a G-rich motif may mediate AR-low prostate cancer-driven translation initiation phenotypes, we asked whether such motifs could be found in other cancer contexts. A mouse model of epidermis examining how this tissue balances progenitor self-renewal and proliferation to inhibit tumorigenesis found that the oncogenic variant HRAS^{G12V} drives a decrease in renewal by increasing translation (Fig. 3.4.2A-B). This is mediated via increased levels of the translation initiation factor eIF2B5, which drives high translation of a set of mRNAs including the ubiquitin ligase FBXO32. These mRNAs inhibit renewal and drive oncogenic hyperproliferation (Fig. 3.4.2C) (Cai et al., 2014). We performed the same *de novo* motif search in the 5’ UTRs of HRAS^{G12V}- and eIF2B5-dependent translationally upregulated genes and found that a G-rich motif highly similar to the GRTE is enriched in both gene sets (Fig. 3.4.2D). Using FBXO32 as a candidate gene, reporter assays revealed that the GRTE-like motif was required for HRAS^{G12V}-mediated translation in mouse epidermis (Fig. 3.4.2E). This finding suggests that G-rich motifs may be widely required to mediate pro-tumorigenic translation initiation dysregulation in multiple cancer contexts.

While GRTE and GRTE-like motifs are enriched in translationally upregulated genes in mouse prostate and skin cancer models, we found that overall about 40% of 5’ UTRs in the mouse genome contain at least one GRTE motif, which means that many non-upregulated genes also contain these motifs. To investigate whether GRTE motifs in non-upregulated genes are also functional, we generated reporter constructs using *Tcea1*, as this gene was not upregulated in AR-low *Pten*$^{fl/fl}$ mice but its 5’ UTR does contain a GRTE motif. Interestingly, we found that deleting the GRTE in the *Tcea1* 5’ UTR did not result in decreased translation of *Fluc*, implying that this motif is not functional (Fig. 3.4.3A). This result suggests that not all GRTE motifs are functional, and that GRTE motifs in non-upregulated genes specifically might not mediate translation initiation phenotypes.

Many noncoding elements are conserved, implying regulatory function (Turner et al., 2014; Polychronopoulos et al., 2017). To further investigate the distinctions between functional and nonfunctional GRTE motifs, we measured their conservation across 100 vertebrate species via two

independent scoring algorithms (Siepel et al., 2005; Pollard et al., 2010). Strikingly, all three GRTE motifs in *Klf5* and the single GRTE in *Denr* are highly conserved, while the non-functional GRTE in *Tcea1* is not (Fig. 3.4.3B). Given this suggested correlation between conservation and function, we asked whether GRTE motifs could be found in human 5' UTRs. We tested the human *KLF5* 5' UTR and found three GRTE motifs. Two of these motifs were conserved and one was not conserved (Fig. 3.4.3B). To understand whether conservation implies function and vice versa for motifs within the same 5' UTR, we generated one WT and three mutant reporter constructs with the human *KLF5* 5' UTR, scrambling the sequence of each GRTE separately The sequences were scrambled systematically via transition mutation, which consists of interchanging purines with each other and pyrimidines with each other (A-G, C-T). We found that while the two highly conserved motifs were required to maintain high translation of the *Fluc* reporter, mutating the unconserved motif did not have a significant effect on translation compared to the WT (Fig. 3.4.3C). In addition, we observed that inducing $4EBP1^{M}$ expression in PC3 cells decreased endogenous KLF5 at the protein level, confirming that the human KLF5 gene remains eIF4F-dependent (Fig. 3.4.3D). Having observed a direct link between conservation and function for every GRTE motif we tested, we next asked if GRTEs in eIF4F-sensitive genes were more highly conserved than those in non-upregulated genes. We performed a genome-wide conservation analysis of GRTE motifs in the human genome and found that GRTEs in translationally upregulated genes were longer and more highly conserved relative to all human 5' UTRs (Fig. 3.4.3E-F). This finding suggests that conservation may be an important clue to indicate the relevance and function of regulatory sequence motifs.

The finding that not all GRTE motifs are functional highlights the importance of understanding the molecular mechanisms by which these motifs interact with eIF4F or 4EBP1 to drive translation initiation. 5' UTR regulatory sequences commonly function by forming structural elements or binding sites (Wang et al., 2021). We used the RNA fold online software (Lorenz et al., 2011) to generate a predicted structure of the KLF5 5' UTR, finding it to be a highly structured sequence with stable base pairing. Interestingly, the first functional GRTE motif facilitates branching and base pairing near the 5' cap, while the second functional GRTE forms a double stem loop in the middle of the structure (Fig. 3.4.4A). To understand the degree to which these motifs contribute to the structure of this 5' UTR, we generated predicted structures with either GRTE scrambled via transition mutation, reproducing the mutations induced in the earlier reporter assay (Fig. 3.4.3C). The mutations caused significant changes to the local structure and relatively minor distal changes. For instance, mutating the first GRTE created a larger branching near the 5' cap but maintained the stem loops formed by the second GRTE, while scrambling the second GRTE eliminated the stem loop without affecting the branch point (Fig. 3.4.4B). Scrambling both motifs together recapitulated the individual changes, resulting in a complex branching structure with no central stem loops (Fig. 3.4.4C). These results suggest that both functional GRTE

motifs in the KLF5 5' UTR are required to form specific local structures but do not significantly affect distal structures in the rest of the UTR.

To test whether GRTE motifs could serve as binding sites for RNA-binding proteins (RBPs), we predicted binding affinities for the sequences of the two GRTEs in the KLF5 5' UTR. Using the CISBP-RNA software (Ray et al., 2013), we found multiple candidate RBPs predicted to bind to one or both sequences. We then validated these candidates using eCLIP data on the ENCODE database (Nostrand et al., 2020; Luo et al., 2020) and confirmed that three RBPs (FUS, TAF15, and SRSF1) bind to the second GRTE in KLF5 (Fig 3.4.4D). FUS and TAF15 both belong to the FET protein family and are known to bind stem-loop RNA structures (Andersson et al., 2008; Hoell et al., 2011; Kashyap et al., 2015). As the second GRTE forms a double stem loop, these findings strongly suggest that this motif can indeed serve as a binding site for RBPs that may affect translation rates and interact with the eIF4F complex. It is unclear whether the first GRTE is not a binding site, as the lack of RBP hits may be due to incomplete eCLIP data. However, the difference in local RNA structure may mean the two motifs do not function through the same molecular mechanism.

Finally, in order to facilitate further study of the GRTE, we generated reporter cell lines expressing the mCherry and eYFP fluorescent reporters. We inserted both the WT KLF5 5' UTR and a double mutant with both functional GRTEs scrambled via transition mutation between eYFP and its doxycycline-inducible TetO promoter, with mCherry as an internal control (Fig. 3.4.4E). We stably integrated these reporter constructs into a safe harbor locus in HEK293T cells to generate isogenic WT and mutant reporter lines (see Methods). We then confirmed by flow cytometry that the KLF5 mutant line yielded two-fold less eYFP signal, with no change in mCherry, recapitulating the strong influence of the GRTE motifs in this context (Fig. 3.4.4F). This system will enable future work delineating the precise mechanisms of these motifs, including comparative RNA structure experiments as well as screens to uncover additional RBP candidates. Specifically, we plan to perform a CRISPR screen to detect RBPs that modulate eYFP intensity in the WT but not mutant line, demonstrating they function through the GRTE motifs.

3.3 Discussion

Here, we demonstrated that a specific subset of mRNAs is translationally upregulated in AR-low prostate cancer in mice due to eIF4F hyperactivity. Further, we uncover a novel sequence element enriched in the 5' UTRs of these mRNAs that is required for maintaining high eIF4F-mediated translation efficiency. We also find a similar motif in a murine model of skin cancer and confirm it mediates translation regulation by an HRAS oncogenic variant. This suggests that G-rich motifs may have a conserved role in modulating translation initiation in multiple cancer contexts. We corroborate

this idea by showing that functional GRTE motifs are highly conserved across vertebrate species, including in humans, and that these motifs are more conserved in cancer-dysregulated mRNAs. As a result, we hypothesize that G-rich tracts in 5' UTRs have important roles in regulating translation initiation in disease contexts.

We also explore potential mechanisms by which the GRTE mediates translation initiation and find that both functional GRTEs in KLF5 significantly contribute to RNA structure. Importantly, these effects are highly local and do not influence distal structural features, suggesting that these motifs may form precise structural elements dedicated to specific functions, rather than constituting the structural backbone of the 5' UTR. RNA sequence and structural elements frequently generate binding sites for RBPs. We found that the second GRTE motif forms a double stem loop and used publicly available eCLIP data to confirm that two proteins (FUS and TAF15) known to bind RNA stem loops bind this motif (Hoell et al., 2011; Kashyap et al., 2015). This finding exemplifies the link between RNA structure and function, and strongly suggests that the second GRTE serves as an RBP binding site via the stem loop structure it creates. FUS and TAF15 are primarily splicing factors but have multiple roles in mRNA processing, including in transcription and mRNA transport (Andersson et al., 2008) Interestingly, FUS has been shown to co-localize with active RNPs to stress or stress-like granules, where it can both enhance or suppress translation (Yasuda et al., 2013; Kamelgarn et al., 2018; Sevigny et al., 2021). These findings imply FUS could recruit mRNAs with stem loops to granules containing RNP complexes, allowing for efficient translation. Whether FUS interacts directly with eIF4F via binding 5' UTR stem loop, or more generally helps recruit a suite of translation factors, is unclear and could be an area of further research to clarify its mechanism of action in the context of translation initiation. Future work includes RNA immunoprecipitation (RIP) assays to confirm that FUS and TAF15 bind to KLF5 via its second GRTE motif, knockdown by pooled shRNAs to validate their effect on KLF5 translation, and high-throughput experiments to characterize additional translation targets containing stem loop-forming GRTEs.

It is notable that the first GRTE does not form a stem loop and did not have any binding partners found in eCLIP datasets. This motif is also considerably shorter (20nt) than the second GRTE (32bp) which may affect its function. For instance, it is possible that GRTE motifs that form more complex structure are necessarily longer, while simpler base-pairing arrangements require fewer nucleotides to be functional. These striking differences between GRTE motifs demonstrate the diversity of these sequence elements and hints at different roles in regulating translation. One possibility is that the first GRTE motif, being only 3nt away from the 5' cap, directly interacts with the eIF4F complex. The G-rich nature of the motif may strengthen base-pairing around the cap, which could stabilize it for binding by eIF4E, or increase its dependence on helicase activity by eIF4A to unwind the RNA and permit

ribosome scanning. This function has previously been described for G-quadruplexes, another G-rich motif highly similar to the GRTE (Wolfe et al., 2014). Another hypothesis is that as not all RBPs have been examined by eCLIP, this GRTE has binding partners that remain unknown. Cap-binding assays to determine the importance of this motif in facilitating eIF4E binding to the KLF5 mRNA would elucidate the first proposed mechanism, while knockdown of eIF4A could reveal whether a scrambled GRTE mutant is more easily translated in the absence of helicase activity.

Finally, we used a WT and a double GRTE mutant version of the KLF5 5' UTR to generate isogenic stable fluorescent reporter lines. We validated that the double mutant decreases translation in these reporter lines and propose that this system will facilitate further investigation of the function of the GRTE. These reporter constructs offer a controlled platform to conduct RNA structure experiments using reagents such as DMS or SHAPE (Tijerina et al., 2007; Wilkinson et al., 2006), with no differences in the mRNA transcripts aside from the scrambled GRTE motifs. In addition, the dual reporter system allows for systematic CRISPR or shRNA screens to uncover additional RBPs that interact with one or both GRTEs. Interestingly, due to the different structures formed by the two motifs, we expect different RBPs to bind to each GRTE. We may be able to differentiate their binding partners via published data on the RNA-binding domains of each RBP. In addition, validating screen candidates through RNA footprinting experiments (Hafner et al., 2021), of simple knockdowns in the presence of reporter constructs with either GRTE mutated, can shed light on which motif is required for an RBP to affect KLF5 translation.

Overall, we have uncovered a novel conserved sequence motif that is active in multiple cancer contexts and may provide important binding sites by contributing specific RNA structural features to the 5' UTRs of key oncogenic regulators. Future work is still needed to understand precisely how these motifs function, and to characterize multiple possible mechanisms that may be dependent on the structure formed by the motif or its location within the 5' UTR.

3.4 Figures and Legends

A

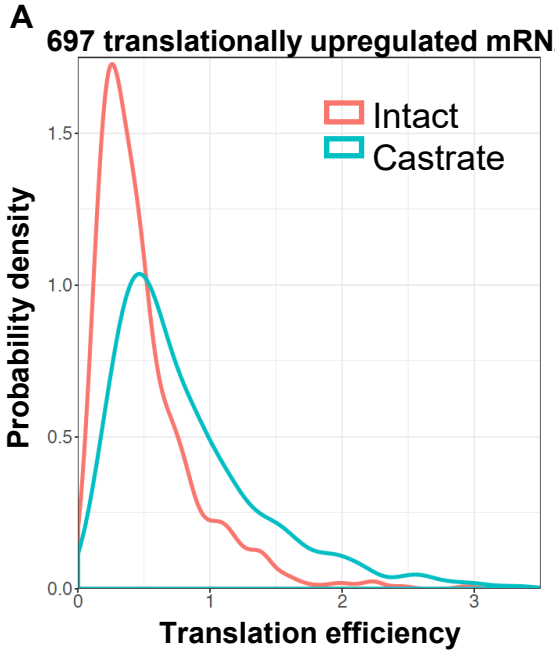
697 translationally upregulated mRNAs
Intact
Castrate
Probability density
Translation efficiency
0.0
0.5
1.0
1.5
0
1
2
3

B

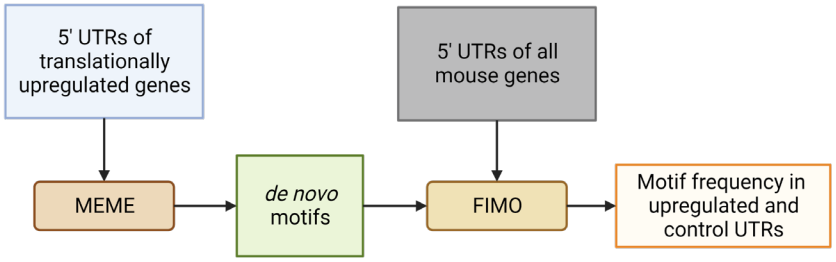
5' UTRs of translationally upregulated genes
5' UTRs of all mouse genes
MEME
de novo motifs
FIMO
Motif frequency in upregulated and control UTRs

C

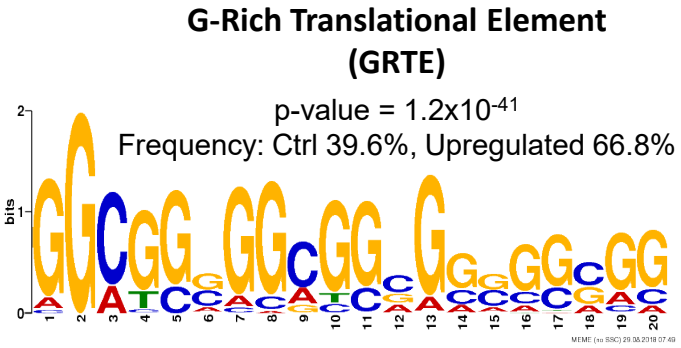
G-Rich Translational Element (GRTE)
p-value = 1.2x10-41
Frequency: Ctrl 39.6%, Upregulated 66.8%
bits

D

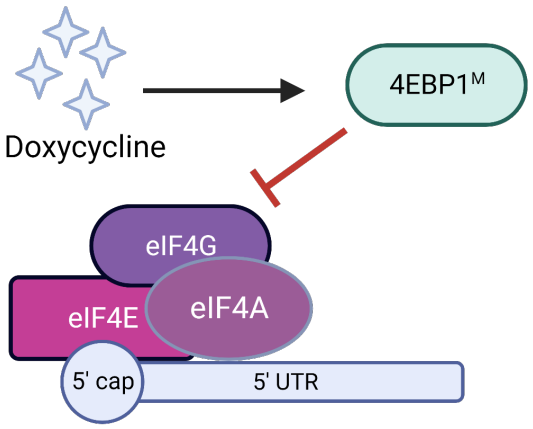
Doxycycline
4EBP1M
eIF4G
eIF4E
eIF4A
5' cap
5' UTR

E

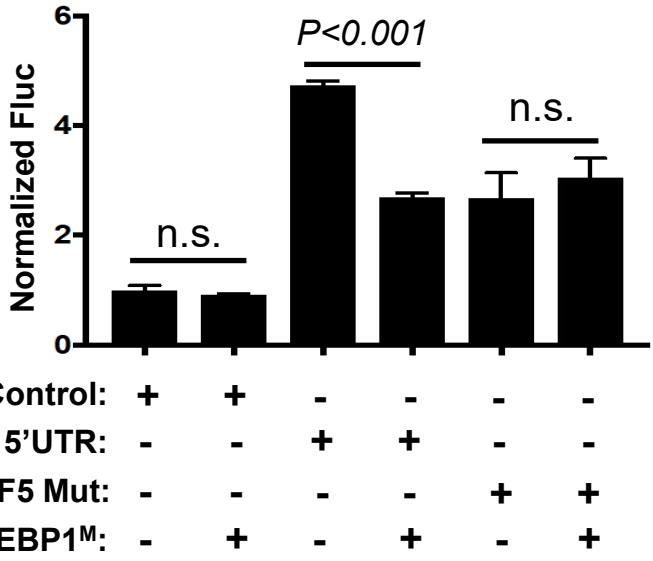
Normalized Fluc
P<0.001
n.s.
n.s.
0
2
4
6
Control: + + - - - -
KLF5 5'UTR: - - + + - -
KLF5 Mut: - - - - + +
4EBP1M: - + - + - +

F

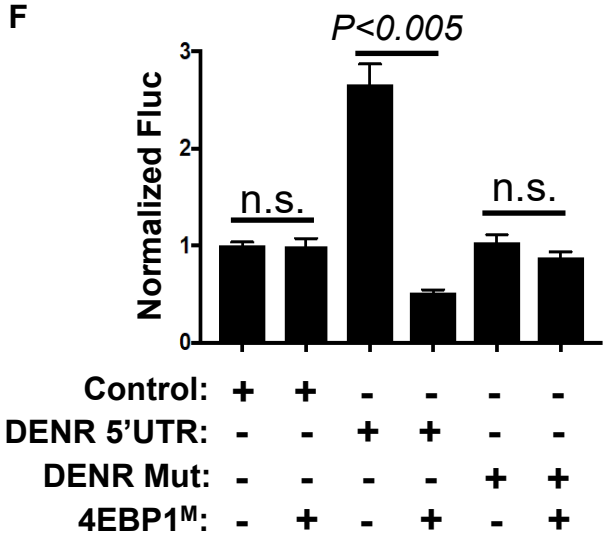
Normalized Fluc
P<0.005
n.s.
n.s.
0
1
2
3
Control: + + - - - -
DENR 5'UTR: - - + + - -
DENR Mut: - - - - + +
4EBP1M: - + - + - +

Figure 3.4.1: The GRTE is Enriched in Translationally Dysregulated mRNAs in AR-low Prostate Cancer

A) Probability density graph of 697 translationally up-regulated mRNAs between intact (n = 2) and castrate (n = 3) *Pten*$^{fl/fl}$ ventral prostates. Translation efficiency, ribosome-bound mRNA/total mRNA ($P < 2.2 \times 10^{-16}$, Kolmogorov-Smirnov test). **B)** Diagram of *de novo* motif search nusing the MEME software suite **C)** The guanine-rich translational element (GRTE) consensus sequence. FIMO analysis reveals that the GRTE is significantly enriched in 5'UTRs of mRNAs that are translationally upregulated in castrated *Pten*$^{fl/fl}$ mice, in comparison to the entire mouse genome (control). **D)** Diagram of inducible 4EBP1^{M} function in PC3 cells **E)** Luciferase assay of the control vector, wild-type *Klf5* 5′UTR luciferase construct, and its GRTE deletion mutant with or without 4EBP1^{M} induction. Luciferase assay was normalized to luc and RPS19 mRNA (n.s., not statistically significant; n > 3 biological replicates per condition, t test). **F)** Luciferase assay of the control vector, wild-type *Denr* 5′UTR luciferase construct, and its GRTE deletion mutant with or without 4EBP1^{M} induction. Luciferase assay was normalized to luc and RPS19 mRNA (n.s., not statistically significant; n > 3 biological replicates per condition, t test).

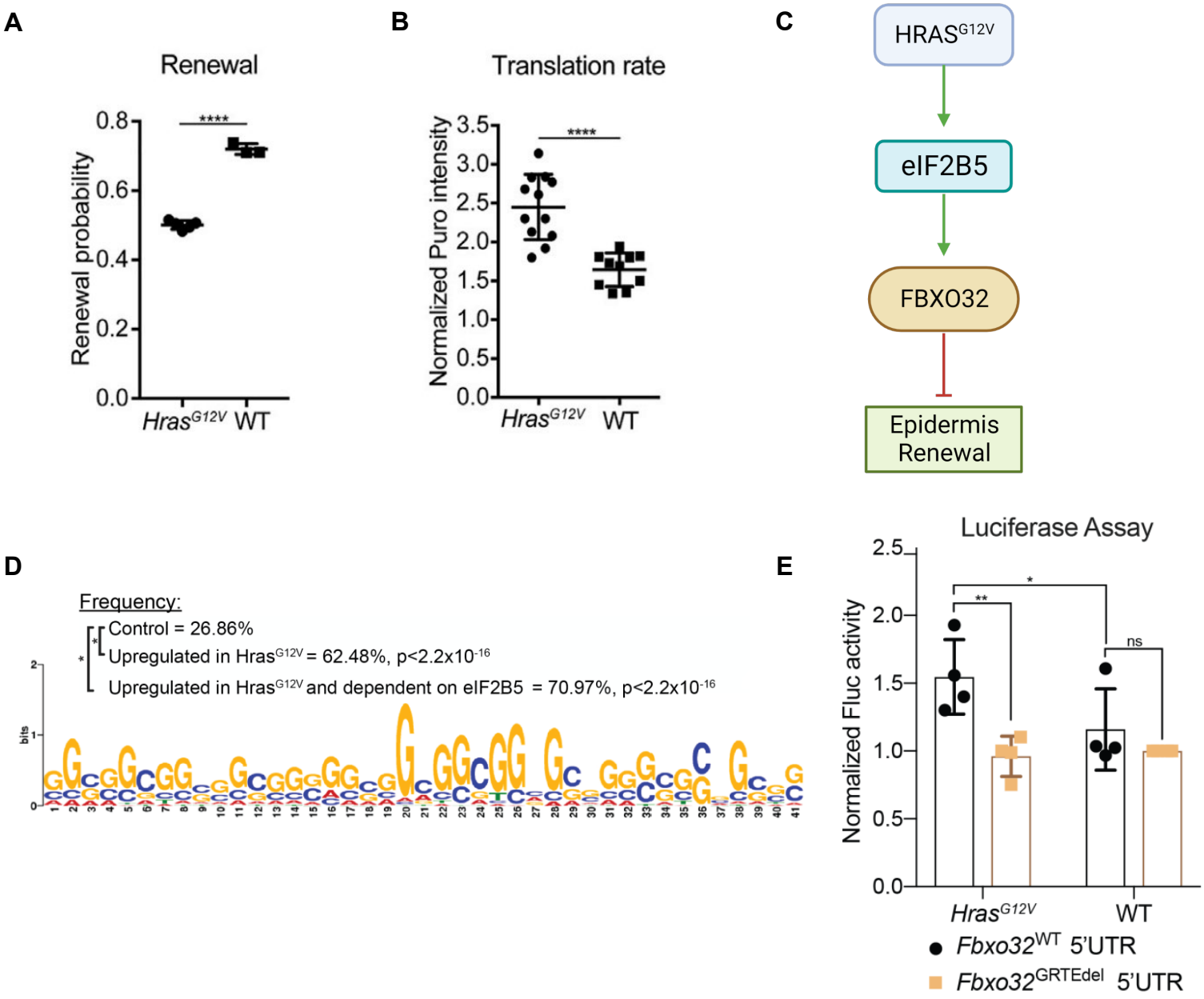
A
Renewal
Renewal probability
0.8
0.6
0.4
0.2
0.0
****
HrasG12V
WT
B
Translation rate
Normalized Puro intensity
3.5
3.0
2.5
2.0
1.5
1.0
0.5
0.0
****
HrasG12V
WT
C
HRASG12V
eIF2B5
FBXO32
Epidermis Renewal
D
Frequency:
Control = 26.86%
Upregulated in HrasG12V = 62.48%, p<2.2x10-16
Upregulated in HrasG12V and dependent on eIF2B5 = 70.97%, p<2.2x10-16
bits
E
Luciferase Assay
Normalized Fluc activity
2.5
2.0
1.5
1.0
0.5
0.0
*
**
ns
HrasG12V
WT
Fbxo32WT 5'UTR
Fbxo32GRTEdel 5'UTR

Figure 3.4.2: A GRTE-Like Motif Mediates HRAS^{G12V} Oncogenic Activity in Skin Cancer

A) Progenitor cell renewal probability in IFE basal cells transduced with control shRNA. n = 4 Hras^{G12V} and 3 WT animals. Approximately 100 cell divisions were scored per animal. **B)** Translation rate as measured by in vivo puromycin incorporation. Hras^{G12V} and WT epidermis were transduced with control shRNA. Puromycin intensity in transduced IFE basal cells was normalized to underlying dermal puromycin intensity. n = 12 Hras^{G12V} and 11 WT imaging fields containing epidermis and dermis. 3 animals per condition were assessed. **C)** Diagram of the effect of the HRAS^{G12V} oncogenic variant leading to renewal inhibition in mouse epidermis. **D)** The guanine-rich translational element (GRTE)-like consensus sequence. FIMO analysis reveals that the GRTE-like motif is significantly enriched in 5'UTRs of mRNAs that are translationally upregulated in Hras^{G12V} and dependent on eIF2B5, in comparison to the entire mouse genome (control). **E)** Luciferase reporter assay in primary keratinocytes to test translation initiation using the full length Fbxo32 5'UTR (Fbxo32^{WT}) or a GRTE deletion mutant (Fbxo32^{GRTEdel}). Translation level is quantified by normalizing luciferase RLU to mRNA level. n=4 biological replicates.

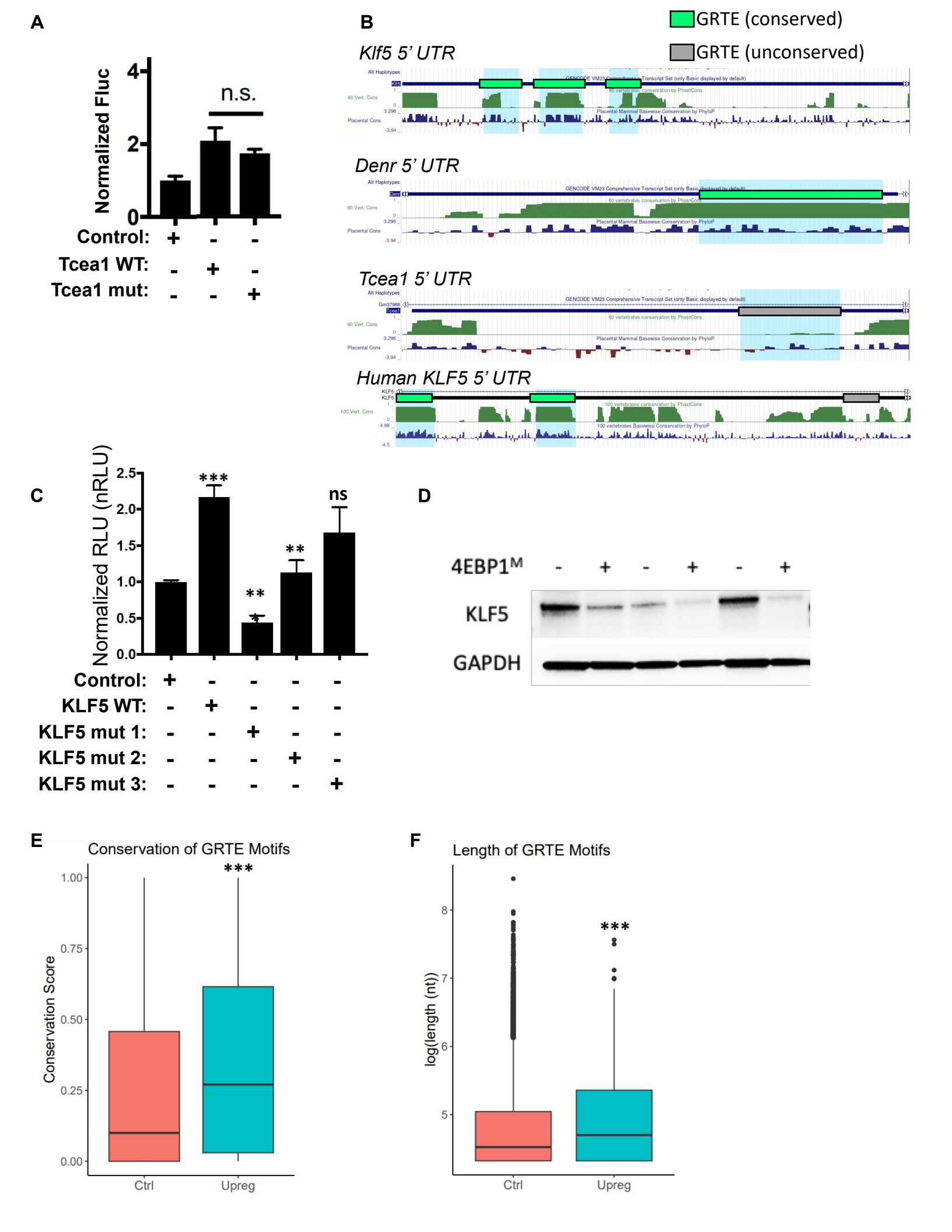
A
Normalized Fluc
n.s.
Control:
Tcea1 WT:
Tcea1 mut:
B
GRTE (conserved)
GRTE (unconserved)
Klf5 5' UTR
Denr 5' UTR
Tcea1 5' UTR
Human KLF5 5' UTR
C
Normalized RLU (nRLU)
***
**
**
ns
Control:
KLF5 WT:
KLF5 mut 1:
KLF5 mut 2:
KLF5 mut 3:
D
4EBP1M
KLF5
GAPDH
E
Conservation of GRTE Motifs
***
Conservation Score
Ctrl
Upreg
F
Length of GRTE Motifs
***
log(length (nt))
Ctrl
Upreg

Figure 3.4.3: Functional GRTEs are Conserved in Mice and Humans

A) Luciferase assay of the control vector, wild-type *Tcea1* 5′UTR luciferase construct, and its GRTE deletion mutant. Luciferase assay was normalized to luc and RPS19 mRNA (n.s., not statistically significant; n > 3 biological replicates per condition, t test). **B)** Extracts from UCSC Genome Browser showing conservation of GRTE motifs in the mouse *Klf5, Denr,* and *Tcea1* 5' UTRs, and the human *KLF5* 5' UTR. Green track shows PhastCons score. Blue track shows PhyloP score. Green rectangles and light blue highlights show conserved GRTE motifs. Gray rectangles show nonconserved GRTE motifs. **C)** Luciferase assay of the control vector, wild-type human *KLF5* 5′UTR luciferase construct, and its three GRTE transition mutants. Luciferase assay was normalized to luc and RPS19 mRNA (n.s., not statistically significant; n > 3 biological replicates per condition, t test). **D)** Western blot showing endogenous KLF5 protein levels in PC3-4EBP1^{M} cells with or without 4EBP!1^{M} induction. GAPDH is used as a loading control. **E)** Box plot of GRTE motif conservation in the human genome compared to genes upregulated in castrated *Pten*$^{fl/fl}$ mice (***p<0.001, Chi-square test). **F)** Box plot of GRTE motif length in the human genome compared to genes upregulated in castrated *Pten*$^{fl/fl}$ mice (***p<0.001, Chi-square test).

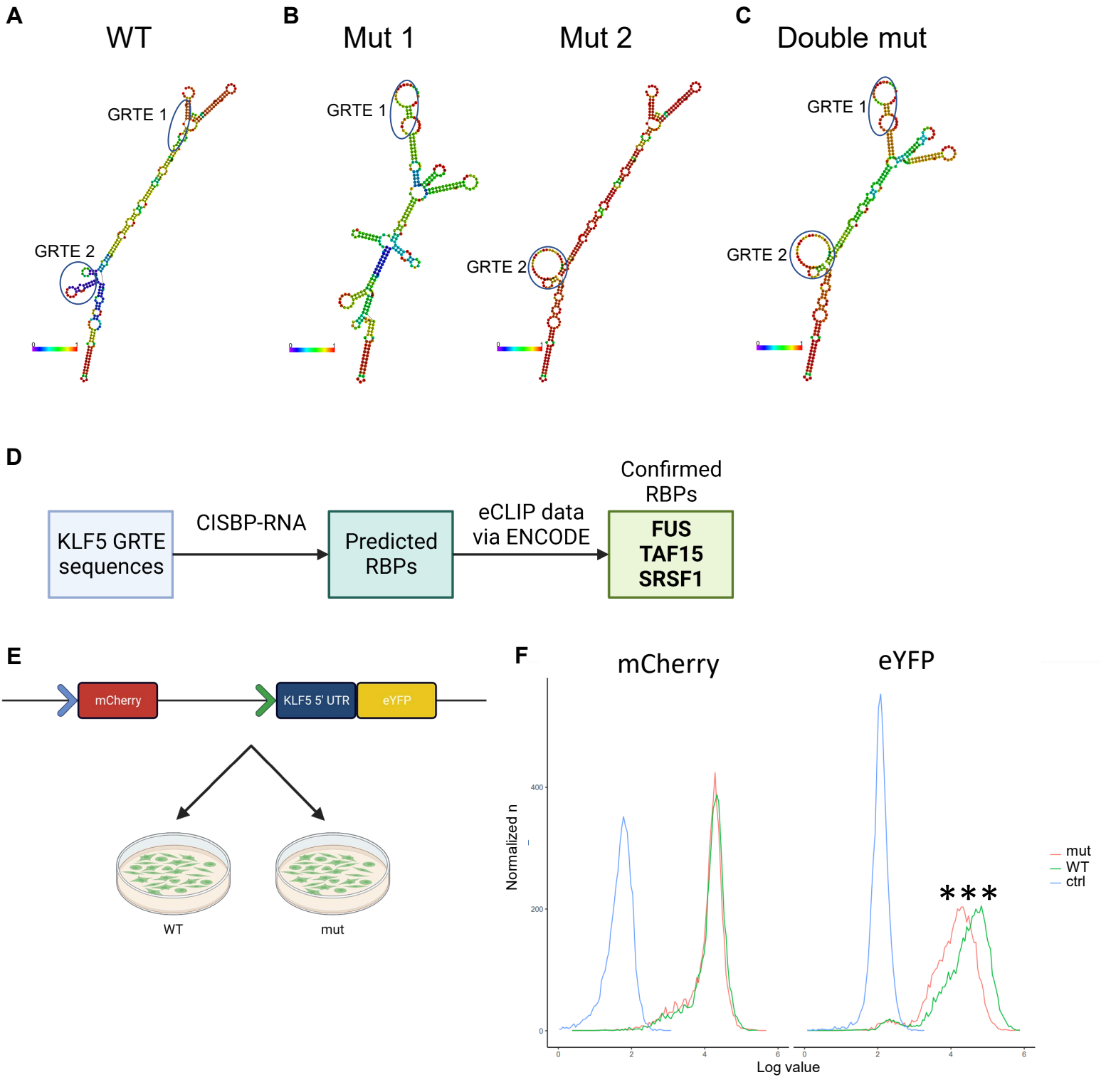
A
WT
GRTE 1
GRTE 2
B
Mut 1
GRTE 1
Mut 2
GRTE 2
C
Double mut
GRTE 1
GRTE 2
D
KLF5 GRTE sequences
CISBP-RNA
Predicted RBPs
eCLIP data via ENCODE
Confirmed RBPs
FUS
TAF15
SRSF1
E
mCherry
KLF5 5' UTR
eYFP
WT
mut
F
mCherry
eYFP
Normalized n
Log value
mut
WT
ctrl
***

Figure 3.4.4: GRTEs in KLF5 Contribute to RNA Structure and Form Binding Sites for RBPs

A) Predicted structure of the WT human *KLF5* 5' UTR. Color scale shows base-pairing probability. GRTE #1 and #2 are circled in blue and labeled. **B)** Predicted structure of human *KLF5* 5' UTR with scrambled GRTE #1 (left) or GRTE #2 (right) mutants. Color scale shows base-pairing probability. **C)** Predicted structure of the human *KLF5* 5' UTR with scramble mutations of both GRTE motifs. Color scale shows base-pairing probability. **D)** Diagram of RBP prediction and validation via eCLIP data. **E)** Diagram of stable reporter lines. **F)** Line plot of mCherry and eYFP expression in *KLF5* WT and mutant reporter cell lines. Data collected via flow cytometry (***$p<0.001$, student's t-test)

3.5 Methods

3.5.1 Ribosome profiling

Flash frozen intact and castrate PtenL/L ventral prostates dissected from each animal were manually pulverized using liquid nitrogen and a biopulverizer and lysed in 1 ml mammalian lysis buffer according to the TruSeq Ribo Profile (Mammalian) protocol (Illumina). To impede post-lysis translation, the lysis buffer was supplemented with cycloheximide (Sigma) dissolved in EtOH, at a final concentration of 0.1 mg/ml. For complete tissue lysis, the samples were further mechanically dissociated using a gentleMACS Dissociator (Miltenyi Biotec). Lysates were centrifuged, and the supernatant was used to isolate both total RNA and ribosome-bound fractions using the TruSeq Ribo Profile (Mammalian) kit (Illumina) in accordance with the manufacturer's protocol. Ribosome footprints were generated by treating part of the lysate with the TruSeq Ribo Profile nuclease for 45 min at room temperature. Resulting monosomes were purified using S400 columns (GE Healthcare), from which ribosome-protected mRNA fragments were isolated and used to prepare ribosome footprint libraries per the manufacturer's protocol (Illumina). Barcodes were used to generate pooled libraries. The pools were sequenced on a HiSeq 2500 platform using the SR50 protocol.

3.5.2 Ribosome profiling analysis

Raw sequence data were uncompressed, followed by clipping the 3' adaptor sequence (AGATCGGAAGAGCACACGTCT). Next, the trimmed sequence reads were aligned to mouse rRNA reference using Bowtie. The unaligned reads were collected while the rRNA alignments were discarded to reduce rRNA contamination. TopHat2 was used to align the non-rRNA sequencing reads to hg19 and counted for gene associations against the UCSC gene database with HTSeq. R/Bioconductor package Xtail was used to find differentially expressed genes at the translational level using both ribosome-bound and mRNA samples (47). For each of the statistical analyses, a statistical cutoff of FDR< or > 0.75 was used (minimum read count of 5). Alkaline-digested total mRNA reads were aligned to the UCSC mm10 assembly using Tophat2 and counted for gene associations against the UCSC genes database with HTSeq. Differential expression analysis was performed using R/Bioconductor package DESeq2. R/Bioconductor package, riboseqR was used to calculate triplet periodicity in all samples. GSEA analysis was done using the Broad website for GSEA (http://software.broadinstitute.org/gsea/index.jsp).

3.5.3 De novo motif search

The MEME suite was used for motif discovery and analysis in the 187 genes found to be upregulated in ribosome profiling (FDR0.75) (45). 5' UTRs for each gene were obtained from the UCSC

Genome Browser (mm10) and inputted into the MEME pipeline (default settings, output of 15 motifs) to discover the GRTE. We entered the GRTE position weighted map into FIMO to determine the prevalence of the GRTE in translationally upregulated mRNAs (46). A list of all 5' UTRs from the mouse genome (n=19009) was also obtained from UCSC and used as a control dataset. Enrichment was calculated using Pearson's c2 -test, counting genes with at least one occurrence of the GRTE as successes.

3.5.4 Transgenic cell line generation

Lentiviruses were packaged by co-transfection of an envelope plasmid and a packaging plasmid along with the 4EBP1^{M} plasmid in 293T cells. PC3 cells were transduced with these lentiviruses and selected with puromycin for 5 days. PC3- 4EBP1^{M} cells were cultured in RPMI-1640 with 10% FBS

3.5.5 Quantitative PCR

Total RNA was isolated using RNeasy Plus Mini Kit (Qiagen) and reverse-transcribed with iScript Reverse Transcription Supermix (Bio-Rad). cDNA was diluted 1:1 with water. Quantitative PCR was performed with 1 µl cDNA using SsoAdvanced SYBR Supermix (Bio-Rad) with primer sets specific for luciferase, YFP, mCherry, and RPS19. Normalized mRNA expression was calculated using the comparative Ct method.

3.5.6 Cloning of GRTE-containing 5' UTRs into luciferase reporter plasmid

The 5' UTRs of Klf5, Denr, and Tcea1 were obtained through PCR of C57BL/6 mouse cDNA using oligonucleotides which contain extensions complementary to the pGL3 reporter plasmid (see table S3). The 5' UTR PCR products were subsequently isolated by gel purification. The pGL3 vector was digested with NcoI, which cuts immediately upstream of the luciferase translation start site. The Klf5, Denr, and Tcea1 5' UTRs were cloned into the linearized pGL3 vector using the Gibson Assembly Master Mix (NEB). The GRTE motif(s) in each of the 5' UTRs were deleted using the Q5 Site-Directed Mutagenesis Kit (NEB).

3.5.7 Luciferase reporter assays

6-well plates were seeded with PC3-4EBP1M (2x105 cells/well) in RPMI medium. After 24 hours, medium was replaced with either normal RPMI medium or RPMI with 0.5 µg/ml doxycycline. 6 hours later, each plate was transfected with either empty pGL3 vector or test vectors. Cells were collected 18 hours after transfection. Half of each well was used for RNA extraction, and half for protein extraction. RNA was extracted using the Qiagen RNEasy kit and used for normalization by qPCR. Protein lysates were used to delineate luciferase activity with the ONE-Glo EX reagent (Promega). Luminescence was

detected on a Synergy 2 multi-detection Microplate Reader (Biotek) with an integration time of 2 s and sensitivity of 150.

3.5.8 Murine epidermal translation and renewal assays

Basal cell renewal probability was quantified based on nucleoside incorporation and differentiation marker expression as previously described (Ying et al., 2018). Since we can uniquely label a population of epidermal progenitor cells (EdU+ BrdU-) that have undergone division within the initial 2 hours as described above, we can also assess the differentiation state of their daughter cells based on expression of differentiation marker keratin 10 (K10). 50mg/kg EdU (Invitrogen) was administered intraperitoneally, followed by 100mg/kg BrdU (Invitrogen) injection 2 hours later, before assessing nucleoside incorporation by immunofluorescence 6 hours post-BrdU injection. We calculated the probability of progenitor cell renewal during the first 2 hours using the following equation:
Renewal probability = (number of EdU + BrdU- K10 - cells) / (total number of EdU + BrdU - cells).

Translation rate assay was adapted from previous protocol (Goodman and Hornberger, 2013). Animals were transduced at E9.5 by in utero injection of lentivirus. At E18.5, maternal mice were injected intraperitoneally with 50mg/kg puromycin (Thermo Fisher) and euthanized after 30 min to collect E18.5 embryos. Headskin was fixed in 4% paraformaldehyde and paraffin-embedded. Sections were de-waxed and stained using the immunofluorescence procedure described above with the following modifications: antigen retrieval was performed using citrate-based antigen unmasking solution (Vector) at 95C for 30 min. Sections were subjected to incubation with puromycin antibody (12D10, Millipore) followed by incubation with secondary antibody conjugated to Alexa Fluor 594 (Invitrogen). Puromycin intensity in transduced epidermal basal cells was quantified by (Alexa Fluor 594 total fluorescence intensity)/(surface area) in K5+GFP+ regions of tissue cross-sections using Imaris software (Bitplane). To normalize for potential differences in puromycin administration or incorporation between animals, we employed the following internal controls: 1) In partially transduced tissues, puromycin intensity in K5+GFP+ transduced basal cells was normalized to puromycin intensity in neighboring K5+ GFP- un-transduced WT basal cells in each tissue section; and 2) In fully transduced tissues, puromycin intensity in K5+ epidermal basal cells was normalized to puromycin intensity in the immediate underlying dermis in each tissue section.

3.5.9 Candidate gene conservation analysis

Conservation scores for the GRTE motifs in the mouse *Klf5, Denr,* and *Tcea1* 5’ UTRs as well as the human KLF5 5’ UTR were generated via the UCSC Genome Browser. For mouse genes, the m10 mouse genome assembly was used. For the human KLF5 gene, the hg38 genome was used. The

PhyloP and PhastCons (Siepel et al., 2005; Pollard et al., 2010) tracks were selected and genomic locations of the GRTE motifs were selected to evaluate conservation.

3.5.10 Genome-wide conservation analysis

5' UTR sequences for every gene in the human genome were obtained using the UCSC Table Browser utr5 table. Multiple isoforms existed for most genes; to simplify the analysis, the longest sequence was chosen. GRTEs were found using the MEME suite as described above. Genomic locations of the GRTEs were computed using the GenomicRanges package in R (Lawrence et al., 2013). Conservation scores for each GRTE were computed using the Phastcons algorithm via the phastCons100way.UCSC.hg38 package in R (Siepel et al., 2005).

3.5.11 Western blots

Cells were lysed for 30 min on ice in lysis buffer containing 150 mM NaCl, 50 mM Tris, 4 mM KCl, 1 mM MgCl2, 1 mM Na3VO4, 10% glycerol, 1% Nonidet P-40, supplemented with phosphatase and protease inhibitor cocktails (Roche). Lysates were cleared by centrifugation at 12000 rpm for 15 min at 4°C. Supernatants were removed and assayed for protein concentration using the Protein Assay Dye Reagent (Bio-Rad). Equal amounts of proteins were subjected to SDS-PAGE and transferred to PVDF membranes (Bio-Rad). Membranes were blocked with 5% non-fat milk in PBS-Tween and were subsequently incubated with the following antibodies at 4°C overnight: KLF5 and GAPDH. Membranes were washed in PBS-Tween and then incubated with HRP-tagged anti-rabbit or antimouse secondary antibodies (Thermo Fisher) for 1 hour at room temperature and developed using Pierce blotting substrates. Signal detection was performed using the ChemiDoc Touch Imaging System (Bio-Rad).

3.5.12 RNA structure prediction

Four RNA sequences were entered into the RNAfold web server (Lorenz et al., 2011) and the minimum free energy (MFE) model of each was calculated. The sequences consisted of the full human KLF5 mRNA with no changes, one of two GRTE motifs scrambled, or both motifs scrambled. The GRTE motifs were scrambled by transition mutation, where every purine is changed to the other purine and every pyrimidine is changed to the other pyrimidine. Changes to predicted RNA structure were assessed from visualization of the MFE.

3.5.13 RBP affinity prediction

Two functionally validated GRTE sequences from the human KLF5 5' UTR were entered into the CISBP-RNA online software (Ray et al., 2013) and predicted RBP gene names were collected. eCLIP data (Nostrand et al., 2020) was queried from the ENCODE dataset (Luo et al., 2020) for each predicted RBP. If eCLIP data was available, the genomic location of each GRTE was entered into the

field viewer and checked for peaks. The presence of peaks was interpreted as biological evidence that the RBP binds the motif.

3.5.14 Dual fluorescent reporter line generation and testing

Dual fluorescent mCherry-KLF5-eYFP reporter lines were generated by co-transfecting the reporter plasmid and an integrase plasmid in 293T cells containing a landing pad construct in the AAVS1 safe harbor locus. The landing pad contains attP and attB sites, allowing integration of the reporter system. Two reporter lines were made, with either the WT human KLF5 5' UTR or a mutant with both GRTE motifs scrambled inserted between eYFP and its promoter. The cells were selected with hygromycin for 10 days then sorted for mCherry+/YFP+ via flow cytometry on the Sony MA900 sorter. After verifying the cells were over 95% double positive for the reporters, flow cytometry analysis was conducted on the Celesta analyzer. mCherry and YFP expression in WT and mutant lines was calculated using the flowCore package in R (Hahne et al., 2009).

Chapter 4. Discussion

4.1 A castration-resistant epithelial cell state that expands in a murine prostate cancer model likely drives progression and treatment resistance in human disease

Here we describe the expansion of a *Krt4*+ epithelial subtype upon murine prostate cancer initiation and progression. This cell state has been extensively studied in normal prostate and is implicated in disease. Interestingly, it is central to cell plasticity in the prostate: while *Krt4*+ "luminal progenitors" constitute a distinct lineage within the prostate, canonically differentiated luminal cells can phenotype switch and take on a *Krt4*+ state to survive androgen deprivation, retaining the capacity to switch back to their original phenotype during regeneration (Kwon et al., 2020; Karthaus et al., 2020). These cells can also initiate tumorigenesis, although their role in cancer is not as fully characterized (Guo et al., 2020).

In this work we find that multiple prostate cell types likely converge to increase abundance of Krt4+ cells even absent increased luminal progenitor proliferation. Specifically, we observe transdifferentiation of basal cells into Krt4+ "intermediate" cells as well as depletion of differentiated luminal cells that is likely due to phenotype switching. Strikingly, unlike luminal cells, basal cell abundance is maintained by a highly proliferative subset of the compartment which does not exist in WT prostates. This implies that basal cell homeostasis is important for prostate cancer. Murine prostate cancer can originate in basal cells if these cells transform into luminal cells first, which corresponds well with our observed phenotype; however, compensatory basal hyperproliferation has never been described in the field. Understanding the molecular factors that trigger this proliferative split in the basal compartment could shed light on the process of tumorigenesis in basal cells.

We further confirm that basal and intermediate cells, but not luminal cells, are castration-resistant. Castration increases intermediate heterogeneity, which we characterize by showing a spectrum of residual AR expression inversely correlated with both translation and proliferation signatures. This recapitulates previous whole-tissue findings that hyperproliferation is driven by eIF4F hyperactivity in AR-low *Pten*$^{fl/fl}$ mice. Interestingly, intermediate cells with the lowest AR activity and highest proliferation and translation also express the basal markers *Krt5* and *Krt15*, which suggests basal-originating intermediate cells are chiefly responsible for driving hyperproliferative AR-low phenotypes. The same translation signature is also highly expressed in basal cells in the castrate mouse, validating the correlation between basal cell identity and high translation rates. We speculate that basal cells may be intrinsically more plastic than luminal cells and therefore may more easily transition to tumor-initiating phenotypes.

As previously expressed in Chapter 1, physiological, genomic, and technical differences between mouse models and human disease must advise caution in applying murine findings to clinical contexts. To understand the human significance of intermediate cells, we applied a patient-derived signature of ADT resistance to our scRNAseq data (Wilkinson et al., 2021) and found that it is specifically enriched in intermediate cells of castrate *Pten*$^{fl/fl}$ mice. Five genes from this signature were especially highly expressed in these cells, and their overexpression correlates with poor patient outcomes. In addition, we analyzed single-cell RNAseq data from human primary and metastatic prostate cancer samples. We found a striking enrichment of this 5-gene signature and of intermediate markers in a specific cluster of the metastatic samples, but not the primary. This suggests that intermediate-like cells exist in advanced human prostate cancer and may contribute to aggressive phenotypes and treatment resistance. Importantly, this metastatic cluster contained cells from five out of the 6 patients in the dataset, demonstrating that this may be a generalizable observation. We speculate that lineage plasticity caused by tumorigenesis may lead to phenotypic convergence towards a stemlike luminal phenotype able to proliferate rapidly and endure androgen-low environments in both human and mouse contexts.

Finally, we inhibit eIF4F activity in AR-low *Pten*$^{fl/fl}$ mice by expressing the 4EBP1^{M} transgene. We show that while overall cell abundance does not change, transgene-containing cells are depleted and express apoptotic and cell cycle arrest gene pathways, suggesting that high translation initiation is necessary for prostate cancer survival in androgen-low conditions. We therefore hypothesize a double-edged mechanism for the role of eIF4F hyperactivity in AR-low CRPC, which is able to promote proliferation and progression but may create an addiction to high translation of select mRNAs. Experiments in WT castrated mice show that androgen deprivation alone is sufficient to induce high translation rates, which is logical as AR loss depletes 4EBP1 levels. However, this high translation does not trigger hyperproliferation in a non-cancer context. One possibility to explain this discrepancy is that castration of WT mice causes rapid atrophy of the prostate. As a result, global transcription my be halted, decreasing the bioavailability of the mRNA transcripts necessary for protein synthesis and proliferation.

Overall, we observe complex cellular dynamics in the mouse prostate upon cancer and androgen loss, which result in a convergence towards an intermediate luminal cell state. This cell state is castration-resistant, highly heterogeneous and likely drives AR-independent progression and treatment resistance in both mice and humans. eIF4F hyperactivity is triggered upon androgen loss and is necessary for cancer proliferation and survival. Further studies should focus on the prognostic value of detecting intermediate-like cells in patients and the potential benefits of therapeutic inhibition of eIF4F.

4.2 Prostate cancer epithelial cells trigger a recruiting cascade to form an immunosuppressive tumor microenvironment

Evasion of the antitumor immune response is a requirement for tumorigenesis and progression (Hanahan and Weinberg, 2011). Prostate cancer is notoriously unresponsive to immunotherapy approaches, highlighting the need to characterize its tumor microenvironment more completely (Stultz and Fong, 2021). Here, we examined the changes in immune cell abundance and recruitment signaling in mouse prostates upon tumorigenesis and AR deprivation. We find that both lymphoid and myeloid cell types expand in the *Pten*$^{fl/fl}$ mouse compared to the WT; the myeloid cells consist of immunosuppressive cell states such as TAMs and MDSCs, while the lymphoid expansion is largely due to cytotoxic CD8+ T cells expressing exhaustion markers. We conclude that prostate cancer creates a pro-tumorigenic environment that inhibits anticancer activity by exhausting CD8+ T cells. Further, we use ligand-receptor analysis to characterize the signaling landscape of the tumor and find that epithelial cells express chemokines that recruit immunosuppressive macrophages and cytotoxic CD8+ T cells. We also observe targeted fibroblasts signaling towards immunosuppressive macrophages, suggesting that stromal cells contribute to building the TME. Interestingly, the recruited macrophages also contact T cells, but emit exhaustion signals. In addition, MDSCs seem to be recruited exclusively by macrophage-mediated signaling, with very few ligands expressed by epithelial cells. We therefore hypothesize that pro-tumorigenic macrophages are a lynchpin of immune recruitment by prostate cancer in the *Pten*$^{fl/fl}$ mouse model and help attract additional immunosuppressive factors while contributing to T cell exhaustion. The fact that fibroblasts specifically recruit macrophages but not other cell types supports their importance to the tumor homeostasis. While our dataset cannot account for temporal dynamic, we speculate that macrophages may be recruited early in tumorigenesis to assist the creation of a favorable tumor microenvironment. Further experiments will be needed to establish whether depleting macrophages from the prostate, or inhibiting chemokines expressed by epithelial cells, can restore anticancer CD8+ activity.

Interestingly, castrating the *Pten*$^{fl/fl}$ mouse decreases macrophage and CD8+ T cell abundance. We observed that fibroblast-mediated chemokine signaling was interrupted by androgen deprivation, likely causing the depletion of macrophages. Decreased signaling from macrophage may in turn decrease CD8+ T cell abundance. We hypothesized that androgen signaling may be deleterious for tissue-resident macrophages and validated this by showing that TRMs exhibit high AR activity in intact *Pten*$^{fl/fl}$ mice. This finding suggests that a large contingent of the pro-tumorigenic macrophage species present in the TME is derived from tissue-resident macrophages, instead of being recruited from outside of the tissue. We also found a dramatic increase in TNF signaling from both macrophages and MDSCs towards tumor cells. TNF signaling is pro-tumorigenic in AR-low prostate cancer (Mizokami et al., 2000; Sha et al., 2015). This may represent a compensatory mechanism to balance the decrease in immunosuppressive macrophages upon androgen loss. Overall, we describe large-scale changes in immune cell populations in the prostate likely leading to immunosuppressive phenotypes and a

favorable tumor microenvironment. Future work should include depletion of tissue-resident macrophages in pre-cancer models to determine the precise origin on immunosuppressive macrophage species, as well as TNF knockdown to characterize the roles of this signaling pathway in maintaining a favorable TME in AR-low prostate cancer. These experiments should also be attempted in human 3D tissue culture systems featuring co-culture of multiple cell types, to validate whether murine immune mechanisms can apply to human disease.

4.3 A G-rich motif mediates translation dysregulation of specific mRNAs by eIF4F hyperactivity in AR-low prostate cancer

We have shown here and in previous work that aberrant translation initiation mediated by eIF4F hyperactivity is an essential phenotype for AR-low CRPC proliferation and survival and regulates translation of a specific subset of mRNAs (Liu et al., 2019). In Chapter 3, I investigated the molecular mechanisms that enable this specificity. I discovered that a novel guanine-rich motif enriched in the 5' UTRs of these mRNAs. This GRTE motif is functional in multiple candidate genes including the transcription factor *Klf5* which contains three of these motifs. Deletion of the GRTEs in *Klf5* not only decrease protein synthesis but also render the 5' UTR insensitive to changes in eIF4F activity. In addition, two of these motifs are conserved and functional in the human KLF5 5' UTR. We find that overall, GRTE conservation correlates with function, and that these motifs are more highly conserved and longer in mRNAs dysregulated by eIF4F in AR-low prostate cancer in the $Pten^{fl/fl}$ mouse. These findings argue for a length-dependent conserved function of GRTE motifs in the 5' UTRs of eIF4F-dependent mRNAs.

The GRTE is highly diverse across genes and best described as a G-rich tract of variable length. Importantly, a similar, if longer, G-rich motif is found in translationally dysregulated mRNAs in a murine model of melanoma which also features high proliferation rates. This result showed potential interaction with the translation initiation factor eIF2B5, suggesting a functional role for G-rich sequences in regulating translation initiation of mRNAs relevant to malignant growth in multiple tissue types. It is intriguing to observe that multiple initiation factors may interact with these G-rich motifs. Considered alongside the diversity in length and sequence of these motifs, and the multiple cancer contexts in which they are found, these findings lead us to speculate that G-rich sequences may be a fundamental feature in mRNAs highly sensitive to regulation by initiation factors. G-rich tracts could be required for fine-tuning of protein synthesis for genes important in proliferation pathways, and their dysregulation may be a crucial aspect of malignant growth.

We investigated possible mechanisms by which the GRTE might function and found that the KLF5 5' UTR is highly structured. Mutating either functional GRTE motif heavily disrupts this structure albeit

in very different ways. One motif is positioned 3nt away from the transcription start site and contributes to stable base-pairing near the 5' cap, while the other forms a double stem loop in the middle of the 5' UTR structure. RNA structural features frequently serve as binding sites for RBPs, and we indeed found that three proteins bind to the stem loop created by the second GRTE. Two of these proteins, FUS and TAF15, are known to have stem loop-binding domains (Hoell et al., 2011; Kashyap et al., 2015), validating the hypothesis that the GRTEs generate functionally important structures. Given the known functions of FUS in mRNA transport, we speculate that it may function by sequestering the KLF5 mRNA to subcellular locations where it can associate with ribosomal complexes, thus promoting KLF5 protein synthesis (Yasuda et al., 2013). However, more work is necessary to understand how this mechanism might interact with the eIF4F complex. One possibility is that eIF4F co-localizes to the same subcellular locations and relies on FUS-mediated transport to bind the appropriate transcripts. This could be tested by expressing fluorescent protein-tagged eIF4E and FUS and observing whether they colocalize in the cell only with an intact stem loop structure. Pulldown of the KLF5 mRNA might also reveal co-binding of eIF4F and FUS.

Interestingly, we found no proteins that bound the first GRTE motif of KLF5. While it is possible that there exist such RBPs for which eCLIP data was not available, the lack of defined structural features beyond base-pairing and the proximity of this motif to the 5' cap suggests a different mechanism of action. Given its position, it is likely that this GRTE directly interacts with the eIF4F complex. It may stabilize the 5' cap to facilitate binding by eIF4F or increase dependence on eIF4A helicase activity, or even mediate interactions with another RBP or protein complex. Overall, we speculate that both GRTE position and the structures it forms are likely to influence its functions. This also leads to the question of how the GRTE-like motif in murine melanoma (Cai et al., 2020) might function. We hypothesize that this motif will also form specific RNA structures that contribute to translation regulation by initiation factors and that its specific mechanisms may be just as varied as the prostate GRTE across different genes and positional contexts. In sum, we speculate that 20-40nt G-rich tracts may contribute important structural features to specific mRNAs and thereby help fine-tune translation initiation rates. Dysregulated or mutated initiation factors in cancer contexts may rely on these structure to drive aberrant growth. Further work will be necessary to confirm this hypothesis and will necessarily include experiments to define and mutate RNA structure to understand precisely how these sequences interact with translation machinery.

Finally, we generate stable reporter lines using the candidate 5' UTR KLF5. We show that scrambling both GRTE motifs decreases fluorescent reporter expression twofold without changing expression of the internal control, setting the stage for future high-throughput experiments. Specifically, a CRISPR-based knockout screen will reveal additional binding partners of the GRTE. This will set the

stage for experiments featuring other candidate genes that contain GRTEs such as DENR, as we will be able to test candidate RBPs and validate whether they interact with GRTEs in a genome-wide manner, thus potentially elucidating a general mechanism. Further, these isogenic lines containing WT and scrambled GRTE motifs are an ideal model for comparative RNA structure experiments, allowing experimental validation of the predicted structure of the KLF5 5’ UTR and the contributions of the GRTEs to this structure.

Overall, in this work we have demonstrated that G-rich sequences are crucial to maintain high translation rates via dysregulation of initiation factor and may represent a general mechanism wherein RNA structure modulates gene expression in proliferation pathways. We identify likely protein cofactors and provide experimental tools to further interrogate these mechanisms.

References

Alexandra S, Vladimir M, Taha M, Jianda Y, M. ZJ, Alexis D, A. WL, A. PM, Phillip W, S. HT, J. HT, Cameron B, Kasthuri K, Yanyun L, Ceyhan E, Cailian L, T. HC, Lisu W, Antoni R, D. WJ, A. CT. 2014. Genetic Basis for Clinical Response to CTLA-4 Blockade in Melanoma. *New Engl J Med* 371:2189–2199. doi:10.1056/nejmoa1406498

Allott EH, Masko EM, Freedland AR, Macias E, Pelton K, Solomon KR, Mostaghel EA, Thomas GV, Pizzo SV, Freeman MR, Freedland SJ. 2018. Serum cholesterol levels and tumor growth in a PTEN-null transgenic mouse model of prostate cancer. *Prostate Cancer P D* 21:196–203. doi:10.1038/s41391-018-0045-x

Alshetaiwi H, Pervolarakis N, McIntyre LL, Ma D, Nguyen Q, Rath JA, Nee K, Hernandez G, Evans K, Torosian L, Silva A, Walsh C, Kessenbrock K. 2020. Defining the emergence of myeloid-derived suppressor cells in breast cancer using single-cell transcriptomics. *Sci Immunol* 5:eaay6017. doi:10.1126/sciimmunol.aay6017

Andersson MK, Ståhlberg A, Arvidsson Y, Olofsson A, Semb H, Stenman G, Nilsson O, Åman P. 2008. The multifunctional FUS, EWS and TAF15 proto-oncoproteins show cell type-specific expression patterns and involvement in cell spreading and stress response. *Bmc Cell Biol* 9:37. doi:10.1186/1471-2121-9-37

Antoch MP, Wrobel M, Gillard B, Kuropatwinski KK, Toshkov I, Gleiberman AS, Karasik E, Moser MT, Foster BA, Andrianova EL, Chernova OV, Gudkov AV. 2020. Superior cancer preventive efficacy of low versus high dose of mTOR inhibitor in a mouse model of prostate cancer. *Oncotarget* 11:1373–1387. doi:10.18632/oncotarget.27550

Aran D, Looney AP, Liu L, Wu E, Fong V, Hsu A, Chak S, Naikawadi RP, Wolters PJ, Abate AR, Butte AJ, Bhattacharya M. 2019. Reference-based analysis of lung single-cell sequencing reveals a transitional profibrotic macrophage. *Nat Immunol* 20:163–172. doi:10.1038/s41590-018-0276-y

Becerra-Diaz M, Song M, Heller N. 2020. Androgen and Androgen Receptors as Regulators of Monocyte and Macrophage Biology in the Healthy and Diseased Lung. *Front Immunol* 11:1698. doi:10.3389/fimmu.2020.01698

Beltran H, Beer TM, Carducci MA, Bono J de, Gleave M, Hussain M, Kelly WK, Saad F, Sternberg C, Tagawa ST, Tannock IF. 2011. New Therapies for Castration-Resistant Prostate Cancer: Efficacy and Safety. *Eur Urol* 60:279–290. doi:10.1016/j.eururo.2011.04.038

Biffo S, Manfrini N, Ricciardi S. 2018. Crosstalks between translation and metabolism in cancer. *Curr Opin Genet Dev* 48:75–81. doi:10.1016/j.gde.2017.10.011

Bluemn EG, Coleman IM, Lucas JM, Coleman RT, Hernandez-Lopez S, Tharakan R, Bianchi-Frias D, Dumpit RF, Kaipainen A, Corella AN, Yang YC, Nyquist MD, Mostaghel E, Hsieh AC, Zhang X, Corey E, Brown LG, Nguyen HM, Pienta K, Ittmann M, Schweizer M, True LD, Wise D, Rennie PS, Vessella RL, Morrissey C, Nelson PS. 2017. Androgen Receptor Pathway-Independent Prostate Cancer Is Sustained through FGF Signaling. *Cancer Cell* 32:474-489.e6. doi:10.1016/j.ccell.2017.09.003

Boesteanu AC, Katsikis PD. 2009. Memory T cells need CD28 costimulation to remember. *Semin Immunol* 21:69–77. doi:10.1016/j.smim.2009.02.005

Brady NJ, Bagadion AM, Singh R, Conteduca V, Emmenis LV, Arceci E, Pakula H, Carelli R, Khani F, Bakht M, Sigouros M, Bareja R, Sboner A, Elemento O, Tagawa S, Nanus DM, Loda M, Beltran H, Robinson B, Rickman DS. 2021. Temporal evolution of cellular heterogeneity during the progression to advanced AR-negative prostate cancer. *Nat Commun* 12:3372. doi:10.1038/s41467-021-23780-y

Bray NL, Pimentel H, Melsted P, Pachter L. 2016. Near-optimal probabilistic RNA-seq quantification. *Nat Biotechnol* 34:525–527. doi:10.1038/nbt.3519

Buszczak M, Signer RAJ, Morrison SJ. 2014. Cellular Differences in Protein Synthesis Regulate Tissue Homeostasis. *Cell* 159:242–251. doi:10.1016/j.cell.2014.09.016

Cai EY, Kufeld MN, Schuster S, Arora S, Larkin M, Germanos AA, Hsieh AC, Beronja S. 2020. Selective Translation of Cell Fate Regulators Mediates Tolerance to Broad Oncogenic Stress. *Cell Stem Cell* 27:270-283.e7. doi:10.1016/j.stem.2020.05.007

Cao J, Spielmann M, Qiu X, Huang X, Ibrahim DM, Hill AJ, Zhang F, Mundlos S, Christiansen L, Steemers FJ, Trapnell C, Shendure J. 2019. The single cell transcriptional landscape of mammalian organogenesis. *Nature* 566:496–502. doi:10.1038/s41586-019-0969-x

Cham J, Zhang L, Kwek S, Paciorek A, He T, Fong G, Oh DY, Fong L. 2020. Combination immunotherapy induces distinct T-cell repertoire responses when administered to patients with different malignancies. *J Immunother Cancer* 8:e000368. doi:10.1136/jitc-2019-000368

Chang K, Dai B, Kong Y, Qu Y, Wu J, Ye D, Yao X, Zhang S, Zhang H, Zhu Y, Yao W. 2013. Basal cell carcinoma of the prostate: clinicopathologic analysis of three cases and a review of the literature. *World J Surg Oncol* 11:193. doi:10.1186/1477-7819-11-193

Chanmee T, Ontong P, Konno K, Itano N. 2014. Tumor-Associated Macrophages as Major Players in the Tumor Microenvironment. *Cancers* 6:1670–1690. doi:10.3390/cancers6031670

Che M, Chaturvedi A, Munro SA, Pitzen SP, Ling A, Zhang W, Mentzer J, Ku S-Y, Puca L, Zhu Y, Bergman AM, Severson TM, Forster C, Liu Y, Hildebrand J, Daniel M, Wang T-Y, Selth LA, Hickey T, Zoubeidi A, Gleave M, Bareja R, Sboner A, Tilley W, Carroll JS, Tan W, Kohli M, Yang R, Hsieh AC, Murugan P, Zwart W, Beltran H, Huang RS, Dehm SM. 2021. Opposing transcriptional programs of KLF5 and AR emerge during therapy for advanced prostate cancer. *Nat Commun* 12:6377. doi:10.1038/s41467-021-26612-1

Choi J, Chen W, Minkina A, Chardon FM, Suiter CC, Regalado SG, Domcke S, Hamazaki N, Lee C, Martin B, Daza RM, Shendure J. 2022. A time-resolved, multi-symbol molecular recorder via sequential genome editing. *Nature* 608:98–107. doi:10.1038/s41586-022-04922-8

Choi N, Zhang B, Zhang L, Ittmann M, Xin L. 2012. Adult Murine Prostate Basal and Luminal Cells Are Self-Sustained Lineages that Can Both Serve as Targets for Prostate Cancer Initiation. *Cancer Cell* 21:253–265. doi:10.1016/j.ccr.2012.01.005

Cieśla M, Ngoc PCT, Cordero E, Martinez ÁS, Morsing M, Muthukumar S, Beneventi G, Madej M, Munita R, Jönsson T, Lövgren K, Ebbesson A, Nodin B, Hedenfalk I, Jirström K, Vallon-Christersson J, Honeth G, Staaf J, Incarnato D, Pietras K, Bosch A, Bellodi C. 2021. Oncogenic translation directs

spliceosome dynamics revealing an integral role for SF3A3 in breast cancer. *Mol Cell* 81:1453-1468.e12. doi:10.1016/j.molcel.2021.01.034

Cioni B, Zaalberg A, Beijnum JR van, Melis MHM, Burgsteden J van, Muraro MJ, Hooijberg E, Peters D, Hofland I, Lubeck Y, Jong J de, Sanders J, Vivié J, Poel HG van der, Boer JP de, Griffioen AW, Zwart W, Bergman AM. 2020. Androgen receptor signalling in macrophages promotes TREM-1-mediated prostate cancer cell line migration and invasion. *Nat Commun* 11:4498. doi:10.1038/s41467-020-18313-y

Coussens LM, Zitvogel L, Palucka AK. 2013. Neutralizing Tumor-Promoting Chronic Inflammation: A Magic Bullet? *Science* 339:286–291. doi:10.1126/science.1232227

Crowley L, Cambuli F, Aparicio L, Shibata M, Robinson BD, Xuan S, Li W, Hibshoosh H, Loda M, Rabadan R, Shen MM. 2020. A single-cell atlas of the mouse and human prostate reveals heterogeneity and conservation of epithelial progenitors. *Elife* 9:e59465. doi:10.7554/elife.59465

Cuzick J, Swanson GP, Fisher G, Brothman AR, Berney DM, Reid JE, Mesher D, Speights V, Stankiewicz E, Foster CS, Møller H, Scardino P, Warren JD, Park J, Younus A, Flake DD, Wagner S, Gutin A, Lanchbury JS, Stone S, Group on behalf of the TP. 2011. Prognostic value of an RNA expression signature derived from cell cycle proliferation genes in patients with prostate cancer: a retrospective study. *Lancet Oncol* 12:245–255. doi:10.1016/s1470-2045(10)70295-3

Dai C, Heemers H, Sharifi N. 2017. Androgen Signaling in Prostate Cancer. *Csh Perspect Med* 7:a030452. doi:10.1101/cshperspect.a030452

Dassi E. 2017. Handshakes and Fights: The Regulatory Interplay of RNA-Binding Proteins. *Frontiers Mol Biosci* 4:67. doi:10.3389/fmolb.2017.00067

Davey RA, Grossmann M. 2016. Androgen Receptor Structure, Function and Biology: From Bench to Bedside. *Clin Biochem Rev* 37:3–15.

Ding Z, Wu C-J, Chu GC, Xiao Y, Ho D, Zhang J, Perry SR, Labrot ES, Wu X, Lis R, Hoshida Y, Hiller D, Hu B, Jiang S, Zheng H, Stegh AH, Scott KL, Signoretti S, Bardeesy N, Wang YA, Hill DE, Golub TR, Stampfer MJ, Wong WH, Loda M, Mucci L, Chin L, DePinho RA. 2011. SMAD4-dependent barrier constrains prostate cancer growth and metastatic progression. *Nature* 470:269–273. doi:10.1038/nature09677

Djuranovic S, Nahvi A, Green R. 2023. miRNA-Mediated Gene Silencing by Translational Repression Followed by mRNA Deadenylation and Decay. *Science* 336:237–240. doi:10.1126/science.1215691

Dong B, Miao J, Wang Y, Luo W, Ji Z, Lai H, Zhang M, Cheng X, Wang Jinming, Fang Y, Zhu HH, Chua CW, Fan L, Zhu Y, Pan J, Wang Jia, Xue W, Gao W-Q. 2020. Single-cell analysis supports a luminal-neuroendocrine transdifferentiation in human prostate cancer. *Commun Biology* 3:778. doi:10.1038/s42003-020-01476-1

Dong Y, Zhou L, Xia W, Zhao X-Y, Zhang Q, Jian J-M, Gao X, Wang W-P. 2020. Preoperative Prediction of Microvascular Invasion in Hepatocellular Carcinoma: Initial Application of a Radiomic Algorithm Based on Grayscale Ultrasound Images. *Frontiers Oncol* 10:353. doi:10.3389/fonc.2020.00353

Durinck S, Spellman PT, Birney E, Huber W. 2009. Mapping identifiers for the integration of genomic datasets with the R/Bioconductor package biomaRt. *Nat Protoc* 4:1184–1191. doi:10.1038/nprot.2009.97

Efremova M, Vento-Tormo M, Teichmann SA, Vento-Tormo R. 2020. CellPhoneDB: inferring cell–cell communication from combined expression of multi-subunit ligand–receptor complexes. *Nat Protoc* 15:1484–1506. doi:10.1038/s41596-020-0292-x

Etzioni R, Tsodikov A, Mariotto A, Szabo A, Falcon S, Wegelin J, diTommaso D, Karnofski K, Gulati R, Penson DF, Feuer E. 2008. Quantifying the role of PSA screening in the US prostate cancer mortality decline. *Cancer Cause Control* 19:175–181. doi:10.1007/s10552-007-9083-8

Fabbri L, Chakraborty A, Robert C, Vagner S. 2021. The plasticity of mRNA translation during cancer progression and therapy resistance. *Nat Rev Cancer* 558–577.

Floor SN, Doudna JA. 2016. Tunable protein synthesis by transcript isoforms in human cells. *Elife* 5:e10921. doi:10.7554/elife.10921

Franck P, Anne B, Matthieu C, Fatima S-C, Anne C, Robert M, Bernhard M, Amos K, Malin N, Diane D, Tchao M, Patrick B, Paul-Henri C, Zlatko T, Wolf-Herman F, Jérôme G. 2005. Effector Memory T Cells, Early Metastasis, and Survival in Colorectal Cancer. *New Engl J Med* 353:2654–2666. doi:10.1056/nejmoa051424

Franks A, Airoldi E, Slavov N. 2017. Post-transcriptional regulation across human tissues. *Plos Comput Biol* 13:e1005535. doi:10.1371/journal.pcbi.1005535

Frick J, Aulitzky W. 1991. Physiology of the prostate. *Pathophysiology* S115–S118.

Gajewski TF. 2007. Failure at the Effector Phase: Immune Barriers at the Level of the Melanoma Tumor Microenvironment. *Clin Cancer Res* 13:5256–5261. doi:10.1158/1078-0432.ccr-07-0892

Gajewski TF, Schreiber H, Fu Y-X. 2013. Innate and adaptive immune cells in the tumor microenvironment. *Nat Immunol* 14:1014–1022. doi:10.1038/ni.2703

Galon J, Costes A, Sanchez-Cabo F, Kirilovsky A, Mlecnik B, Lagorce-Pages C, Tosolini M, Camus M, Berger A, Wind P, Zinzindohoue F, Bruneval P, Cugnenc P-H, Trajanoski Z, Fridman W-H, Pages F. 2006. Type, Density, and Location of Immune Cells Within Human Colorectal Tumors Predict Clinical Outcome. *Science* 313:1960–1964.

Garcia AJ, Ruscetti M, Arenzana TL, Tran LM, Bianci-Frias D, Sybert E, Priceman SJ, Wu L, Nelson PS, Smale ST, Wu H. 2014. Pten Null Prostate Epithelium Promotes Localized Myeloid-Derived Suppressor Cell Expansion and Immune Suppression during Tumor Initiation and Progression. *Mol Cell Biol* 34:2017–2028. doi:10.1128/mcb.00090-14

Germanos AA, Arora S, Zheng Y, Goddard ET, Coleman IM, Ku AT, Wilkinson S, Song H, Brady NJ, Amezquita RA, Zager M, Long A, Yang YC, Bielas JH, Gottardo R, Rickman DS, Huang FW, Ghajar CM, Nelson PS, Sowalsky AG, Setty M, Hsieh AC. 2022. Defining cellular population dynamics at single-cell resolution during prostate cancer progression. *Elife* 11. doi:10.7554/elife.79076

GMÜNDER H, LESSLAUER W. 1984. A 45-kDa human T-cell membrane glycoprotein functions in the regulation of cell proliferative responses. *Eur J Biochem* 142:153–160. doi:10.1111/j.1432-1033.1984.tb08263.x

Goldstein AS, Huang J, Guo C, Garraway IP, Witte ON. 2010. Identification of a Cell of Origin for Human Prostate Cancer. *Science* 329:568–571. doi:10.1126/science.1189992

Griffiths JA, Richard AC, Bach K, Lun ATL, Marioni JC. 2018. Detection and removal of barcode swapping in single-cell RNA-seq data. *Nat Commun* 9:2667. doi:10.1038/s41467-018-05083-x

Griss J, Viteri G, Sidiropoulos K, Nguyen V, Fabregat A, Hermjakob H. 2020. ReactomeGSA - Efficient Multi-Omics Comparative Pathway Analysis. *Mol Cell Proteom Mcp* 19:2115–2124. doi:10.1074/mcp.tir120.002155

Grossmann M, Cheung AS, Zajac JD. 2013. Androgens and prostate cancer; pathogenesis and deprivation therapy. *Best Pract Res Cl En* 27:603–616. doi:10.1016/j.beem.2013.05.001

Guérin O, Fischel JL, Ferrero J-M, Bozec A, Milano G. 2010. EGFR Targeting in Hormone-Refractory Prostate Cancer: Current Appraisal and Prospects for Treatment. *Pharm* 3:2238–2247. doi:10.3390/ph3072238

Guo W, Li L, He J, Liu Z, Han M, Li F, Xia X, Zhang X, Zhu Y, Wei Y, Li Y, Aji R, Dai H, Wei H, Li C, Chen Y, Chen L, Gao D. 2020. Single-cell transcriptomics identifies a distinct luminal progenitor cell type in distal prostate invagination tips. *Nat Genet* 52:908–918. doi:10.1038/s41588-020-0642-1

Hafner M, Katsantoni M, Köster T, Marks J, Mukherjee J, Staiger D, Ule J, Zavolan M. 2021. CLIP and complementary methods. *Nat Rev Methods Primers* 1:20. doi:10.1038/s43586-021-00018-1

Hahne F, LeMeur N, Brinkman RR, Ellis B, Haaland P, Sarkar D, Spidlen J, Strain E, Gentleman R. 2009. flowCore: a Bioconductor package for high throughput flow cytometry. *Bmc Bioinformatics* 10:106. doi:10.1186/1471-2105-10-106

Hanahan D, Weinberg RA. 2011. Hallmarks of Cancer: The Next Generation. *Cell* 144:646–674. doi:10.1016/j.cell.2011.02.013

Hänzelmann S, Castelo R, Guinney J. 2013. GSVA: gene set variation analysis for microarray and RNA-Seq data. *Bmc Bioinformatics* 14:7–7. doi:10.1186/1471-2105-14-7

Hao P, Yu J, Ward R, Liu Y, Hao Q, An S, Xu T. 2020. Eukaryotic translation initiation factors as promising targets in cancer therapy. *Cell Commun Signal* 18:175. doi:10.1186/s12964-020-00607-9

Harlin H, Meng Y, Peterson AC, Zha Y, Tretiakova M, Slingluff C, McKee M, Gajewski TF. 2009. Chemokine Expression in Melanoma Metastases Associated with CD8+ T-Cell Recruitment. *Cancer Res* 69:3077–3085. doi:10.1158/0008-5472.can-08-2281

Hentze MW, Castello A, Schwarzl T, Preiss T. 2018. A brave new world of RNA-binding proteins. *Nat Rev Mol Cell Bio* 19:327–341. doi:10.1038/nrm.2017.130

Hieronymus H, Lamb J, Ross KN, Peng XP, Clement C, Rodina A, Nieto M, Du J, Stegmaier K, Raj SM, Maloney KN, Clardy J, Hahn WC, Chiosis G, Golub TR. 2006. Gene expression signature-

based chemical genomic prediction identifies a novel class of HSP90 pathway modulators. *Cancer Cell* 10:321–330. doi:10.1016/j.ccr.2006.09.005

Ho JJD, Man JHS, Schatz JH, Marsden PA. 2021. Translational remodeling by RNA-binding proteins and noncoding RNAs. *Wiley Interdiscip Rev Rna* 12:e1647. doi:10.1002/wrna.1647

Hoell JI, Larsson E, Runge S, Nusbaum JD, Duggimpudi S, Farazi TA, Hafner M, Borkhardt A, Sander C, Tuschl T. 2011. RNA targets of wild-type and mutant FET family proteins. *Nat Struct Mol Biol* 18:1428–1431. doi:10.1038/nsmb.2163

Hsieh AC, Costa M, Zollo O, Davis C, Feldman ME, Testa JR, Meyuhas O, Shokat KM, Ruggero D. 2010. Genetic Dissection of the Oncogenic mTOR Pathway Reveals Druggable Addiction to Translational Control via 4EBP-eIF4E. *Cancer Cell* 17:249–261. doi:10.1016/j.ccr.2010.01.021

Hsieh AC, Liu Y, Edlind MP, Ingolia NT, Janes MR, Sher A, Shi EY, Stumpf CR, Christensen C, Bonham MJ, Wang S, Ren P, Martin M, Jessen K, Feldman ME, Weissman JS, Shokat KM, Rommel C, Ruggero D. 2012. The translational landscape of mTOR signalling steers cancer initiation and metastasis. *Nature* 485:55–61. doi:10.1038/nature10912

Hsieh AC, Nguyen HG, Wen L, Edlind MP, Carroll PR, Kim W, Ruggero D. 2015. Cell type–specific abundance of 4EBP1 primes prostate cancer sensitivity or resistance to PI3K pathway inhibitors. *Science Signaling* 8.

Hua Y, Bergers G. 2019. Tumors vs. Chronic Wounds: An Immune Cell's Perspective. *Front Immunol* 10:2178. doi:10.3389/fimmu.2019.02178

Huggins C, Hodges CV. 1972. Studies on prostatic cancer: I. The effect of castration, of estrogen and of androgen injection on serum phosphatases in metastatic carcinoma of the prostate. *Ca Cancer J Clin* 22:232–240. doi:10.3322/canjclin.22.4.232

Hutchinson L, Kirk R. 2011. High drug attrition rates—where are we going wrong? *Nat Rev Clin Oncol* 8:189–190. doi:10.1038/nrclinonc.2011.34

Ingolia NT, Ghaemmaghami S, Newman JRS, Weissman JS. 2009. Genome-Wide Analysis in Vivo of Translation with Nucleotide Resolution Using Ribosome Profiling. *Science* 324:218–223. doi:10.1126/science.1168978

Jackson RJ, Hellen CUT, Pestova TV. 2010. The mechanism of eukaryotic translation initiation and principles of its regulation. *Nat Reviews* 113–127. doi:10.1038/nrm2838

Jana S, Brahma S, Arora S, Wladyka CL, Hoang P, Blinka S, Hough R, Horn JL, Liu Y, Wang L-J, Depeille P, Smith E, Montgomery RB, Lee JK, Haffner MC, Vakar-Lopez F, Grivas P, Wright JL, Lam H-M, Black PC, Roose JP, Ryazanov AG, Subramaniam AR, Henikoff S, Hsieh AC. 2023. Transcriptional-translational conflict is a barrier to cellular transformation and cancer progression. *Cancer Cell* **41**:853-870.e13. doi:10.1016/j.ccell.2023.03.021

Jana S, Deo R, Hough RP, Liu Y, Horn JL, Wright JL, Lam H-M, Webster KR, Chiang GG, Sonenberg N, Hsieh AC. 2021. mRNA translation is a therapeutic vulnerability necessary for bladder epithelial transformation. *Jci Insight* **6**:e144920. doi:10.1172/jci.insight.144920

Joseph DB, Henry GH, Malewska A, Iqbal NS, Ruetten HM, Turco AE, Abler LL, Sandhu SK, Cadena MT, Malladi VS, Reese JC, Mauck RJ, Gahan JC, Hutchinson RC, Roehrborn CG, Baker LA, Vezina CM, Strand DW. 2020. Urethral luminal epithelia are castration-insensitive cells of the proximal prostate. *Prostate* 80:872–884. doi:10.1002/pros.24020

Joseph DB, Henry GH, Malewska A, Reese JC, Mauck RJ, Gahan JC, Hutchinson RC, Mohler JL, Roehrborn CG, Strand DW. 2022. 5-Alpha reductase inhibitors induce a prostate luminal to club cell transition in human benign prostatic hyperplasia. *J Pathology* 256:427–441. doi:10.1002/path.5857

Kamelgarn M, Chen J, Kuang L, Jin H, Kasarskis EJ, Zhu H. 2018. ALS mutations of FUS suppress protein translation and disrupt the regulation of nonsense-mediated decay. *Proc National Acad Sci* 115:E11904–E11913. doi:10.1073/pnas.1810413115

Kantoff PW, Higano CS, Shore ND, Berger ER, Small EJ, Penson DF, Redfern CH, Ferrari AC, Dreicer R, Sims RB, Xu Y, Frohlich MW, Schellhammer PF, Investigators IS. 2010. Sipuleucel-T Immunotherapy for Castration-Resistant Prostate Cancer. *New Engl J Medicine* 363:411–422. doi:10.1056/nejmoa1001294

Karthaus WR, Hofree M, Choi D, Linton EL, Turkekul M, Bejnood A, Carver B, Gopalan A, Abida W, Laudone V, Biton M, Chaudhary O, Xu T, Masilionis I, Manova K, Mazutis L, Pe'er D, Regev A, Sawyers CL. 2020. Regenerative potential of prostate luminal cells revealed by single-cell analysis. *Science* 368:497–505. doi:10.1126/science.aay0267

Karzai F, Walker SM, Wilkinson S, Madan RA, Shih JH, Merino MJ, Harmon SA, VanderWeele DJ, Cordes LM, Carrabba NV, Bright JR, Terrigino NT, Chun G, Bilusic M, Couvillon A, Hankin A, Williams MN, Lis RT, Ye H, Choyke PL, Gulley JL, Sowalsky AG, Turkbey B, Pinto PA, Dahut WL. 2021. Sequential Prostate Magnetic Resonance Imaging in Newly Diagnosed High-risk Prostate Cancer Treated with Neoadjuvant Enzalutamide is Predictive of Therapeutic Response. *Clin Cancer Res* 27:429–437. doi:10.1158/1078-0432.ccr-20-2344

Kashyap M, Ganguly AK, Bhavesh NS. 2015. Structural delineation of stem-loop RNA binding by human TAF15 protein. *Sci Rep-uk* 5:17298. doi:10.1038/srep17298

Kim J-H, Xu C, Keum Y-S, Reddy B, Conney A, Kong A-NT. 2006. Inhibition of EGFR signaling in human prostate cancer PC-3 cells by combination treatment with β-phenylethyl isothiocyanate and curcumin. *Carcinogenesis* 27:475–482. doi:10.1093/carcin/bgi272

Knudsen KE, Scher HI. 2009. Starving the Addiction: New Opportunities for Durable Suppression of AR Signaling in Prostate Cancer. *Clin Cancer Res* 15:4792–4798. doi:10.1158/1078-0432.ccr-08-2660

Korbecki J, Kojder K, Simińska D, Bohatyrewicz R, Gutowska I, Chlubek D, Baranowska-Bosiacka I. 2020. CC Chemokines in a Tumor: A Review of Pro-Cancer and Anti-Cancer Properties of the Ligands of Receptors CCR1, CCR2, CCR3, and CCR4. *Int J Mol Sci* 21:8412. doi:10.3390/ijms21218412

Korsten H, Made AZ der, Ma X, Kwast T van der, Trapman J. 2009. Accumulating Progenitor Cells in the Luminal Epithelial Cell Layer Are Candidate Tumor Initiating Cells in a Pten Knockout Mouse Prostate Cancer Model. *Plos One* 4:e5662. doi:10.1371/journal.pone.0005662

Ku AT, Sowalsky SW and AG, Sowalsky AG. 2021. Comparison of approaches to transcriptomic analysis in multi-sampled tumors. *Briefings in Bioinformatics* 6:1–12. doi:10.1093/bib/bbab337

Ku SY, Rosario S, Wang Y, Mu P, Seshadri M, Goodrich ZW, Goodrich MM, Labbé DP, Gomez EC, Wang J, Long HW, Xu B, Brown M, Loda M, Sawyers CL, Ellis L, Goodrich DW. 2017. Rb1 and Trp53 cooperate to suppress prostate cancer lineage plasticity, metastasis, and antiandrogen resistance. *Science* 355:78–83. doi:10.1126/science.aah4199

Kwon O, Choi JM, Zhang L, Jia D, Wei X, Li Z, Zhang Y, Jung SY, Creighton CJ, Xin L. 2020. The Sca-1+ and Sca-1− mouse prostatic luminal cell lineages are independently sustained. *Stem Cells* 38:1479–1491. doi:10.1002/stem.3253

Kwon O, Zhang L, Xin L. 2016. Stem Cell Antigen-1 Identifies a Distinct Androgen-Independent Murine Prostatic Luminal Cell Lineage with Bipotent Potential. *Stem Cells* 34:191–202. doi:10.1002/stem.2217

Kwon O-J, Zhang L, Jia D, Xin L. 2021. Sox2 is necessary for androgen ablation-induced neuroendocrine differentiation from Pten null Sca-1+ prostate luminal cells. *Oncogene* 40:203–214. doi:10.1038/s41388-020-01526-2

Labanieh L, Majzner RG, Mackall CL. 2018. Programming CAR-T cells to kill cancer. *Nat Biomed Eng* 2:377–391. doi:10.1038/s41551-018-0235-9

Labrecque MP, Coleman IM, Brown LG, True LD, Kollath L, Lakely B, Nguyen HM, Yang YC, Costa RMG da, Kaipainen A, Coleman R, Higano CS, Yu EY, Cheng HH, Mostaghel EA, Montgomery B, Schweizer MT, Hsieh AC, Lin DW, Corey E, Nelson PS, Morrissey C. 2019. Molecular profiling stratifies diverse phenotypes of treatment-refractory metastatic castration-resistant prostate cancer. *J Clin Invest* 129:4492–4505. doi:10.1172/jci128212

Lai J-J, Lai K-P, Chuang K-H, Chang P, Yu I-C, Lin W-J, Chang C. 2009. Monocyte/macrophage androgen receptor suppresses cutaneous wound healing in mice by enhancing local TNF-α expression. *J Clin Invest* 119:3739–3751. doi:10.1172/jci39335

Lawrence M, Huber W, Pagès H, Aboyoun P, Carlson M, Gentleman R, Morgan MT, Carey VJ. 2013. Software for Computing and Annotating Genomic Ranges. *Plos Comput Biol* 9:e1003118. doi:10.1371/journal.pcbi.1003118

Lim Y, Arora S, Schuster SL, Corey L, Fitzgibbon M, Wladyka CL, Wu X, Coleman IM, Delrow JJ, Corey E, True LD, Nelson PS, Ha G, Hsieh AC. 2021. Multiplexed functional genomic analysis of 5' untranslated region mutations across the spectrum of prostate cancer. *Nat Commun* 12:4217. doi:10.1038/s41467-021-24445-6

Lin H, Cheng J, Mu W, Zhou J, Zhu L. 2021. Advances in Universal CAR-T Cell Therapy. *Front Immunol* 12:744823. doi:10.3389/fimmu.2021.744823

Liu X, Grogan TR, Hieronymus H, Hashimoto T, Mottahedeh J, Cheng D, Zhang L, Huang K, Stoyanova T, Park JW, Shkhyan RO, Nowroozizadeh B, Rettig MB, Sawyers CL, Elashoff D, Horvath S, Huang J, Witte ON, Goldstein AS. 2016. Low CD38 Identifies Progenitor-like Inflammation-Associated Luminal Cells that Can Initiate Human Prostate Cancer and Predict Poor Outcome. *Cell Reports* 17:2596–2606. doi:10.1016/j.celrep.2016.11.010

Liu Y, Horn JL, Banda K, Goodman AZ, Lim Y, Jana S, Arora S, Germanos AA, Wen L, Hardin WR, Yang YC, Coleman IM, Tharakan RG, Cai EY, Uo T, Pillai SPS, Corey E, Morrissey C, Chen Y, Carver BS, Plymate SR, Beronja S, Nelson PS, Hsieh AC. 2019. The androgen receptor regulates a

druggable translational regulon in advanced prostate cancer. *Sci Transl Med* 11:eaaw4993. doi:10.1126/scitranslmed.aaw4993

Liu Y, Yang Q, Zhao F. 2021. Synonymous but Not Silent: The Codon Usage Code for Gene Expression and Protein Folding. *Annu Rev Biochem* 375–401. doi:10.1146/annurev-biochem-071320-112701

Lopez-Bujanda ZA, Haffner MC, Chaimowitz MG, Chowdhury N, Venturini NJ, Patel RA, Obradovic A, Hansen CS, Jacków J, Maynard JP, Sfanos KS, Abate-Shen C, Bieberich CJ, Hurley PJ, Selby MJ, Korman AJ, Christiano AM, Marzo AMD, Drake CG. 2021. Castration-mediated IL-8 promotes myeloid infiltration and prostate cancer progression. *Nat Cancer* 2:803–818. doi:10.1038/s43018-021-00227-3

Lorenz R, Bernhart SH, Siederdissen CH zu, Tafer H, Flamm C, Stadler PF, Hofacker IL. 2011. ViennaRNA Package 2.0. *Algorithm Mol Biol* 6:26. doi:10.1186/1748-7188-6-26

Lu T-L, Huang Y-F, You L-R, Chao N-C, Su F-Y, Chang J-L, Chen C-M. 2013. Conditionally Ablated Pten in Prostate Basal Cells Promotes Basal-to-Luminal Differentiation and Causes Invasive Prostate Cancer in Mice. *Am J Pathology* 182:975–991. doi:10.1016/j.ajpath.2012.11.025

Lun ATL, Riesenfeld S, Andrews T, Dao TP, Gomes T, Jamboree participants in the 1st HCA, Marioni JC. 2019. EmptyDrops: distinguishing cells from empty droplets in droplet-based single-cell RNA sequencing data. *Genome Biol* 20:63. doi:10.1186/s13059-019-1662-y

Luo Y, Hitz BC, Gabdank I, Hilton JA, Kagda MS, Lam B, Myers Z, Sud P, Jou J, Lin K, Baymuradov UK, Graham K, Litton C, Miyasato SR, Strattan JS, Jolanki O, Lee J-W, Tanaka FY, Adenekan P, O'Neill E, Cherry JM. 2019. New developments on the Encyclopedia of DNA Elements (ENCODE) data portal. *Nucleic Acids Res* 48:D882–D889. doi:10.1093/nar/gkz1062

Lv M, Chen M, Zhang R, Zhang W, Wang C, Zhang Y, Wei X, Guan Y, Liu J, Feng K, Jing M, Wang X, Liu Y-C, Mei Q, Han W, Jiang Z. 2020. Manganese is critical for antitumor immune responses via cGAS-STING and improves the efficacy of clinical immunotherapy. *Cell Res* 30:966–979. doi:10.1038/s41422-020-00395-4

Manno GL, Soldatov R, Zeisel A, Braun E, Hochgerner H, Petukhov V, Lidschreiber K, Kastriti ME, Lönnerberg P, Furlan A, Fan J, Borm LE, Liu Z, Bruggen D van, Guo J, He X, Barker R, Sundström E, Castelo-Branco G, Cramer P, Adameyko I, Linnarsson S, Kharchenko PV. 2018. RNA velocity of single cells. *Nature* 560:494–498. doi:10.1038/s41586-018-0414-6

McAuley E, Moline D, VanOpstall C, Lamperis S, Brown R, Griend DJV. 2019. Sox2 Expression Marks Castration-Resistant Progenitor Cells in the Adult Murine Prostate. *Stem Cells* 37:690–700. doi:10.1002/stem.2987

McGranahan N, Furness AJS, Rosenthal R, Ramskov S, Lyngaa R, Saini SK, Jamal-Hanjani M, Wilson GA, Birkbak NJ, Hiley CT, Watkins TBK, Shafi S, Murugaesu N, Mitter R, Akarca AU, Linares J, Marafioti T, Henry JY, Allen EMV, Miao D, Schilling B, Schadendorf D, Garraway LA, Makarov V, Rizvi NA, Snyder A, Hellmann MD, Merghoub T, Wolchok JD, Shukla SA, Wu CJ, Peggs KS, Chan TA, Hadrup SR, Quezada SA, Swanton C. 2016. McGranahan et al Science 2016.pdf. *Science* 351:1463–1469.

Meijer HA, Kong YW, Lu WT, Wilczynska A, Spriggs RV, Robinson SW, Godfrey JD, Willis AE, Bushell M. 2013. Translational Repression and eIF4A2 Activity Are Critical for MicroRNA-Mediated Gene Regulation. *Science* 340:82–85. doi:10.1126/science.1231197

Mevel R, Steiner I, Mason S, Galbraith LC, Patel R, Fadlullah MZ, Ahmad I, Leung HY, Oliveira P, Blyth K, Baena E, Lacaud G. 2020. RUNX1 marks a luminal castration-resistant lineage established at the onset of prostate development. *Elife* 9:e60225. doi:10.7554/elife.60225

Mizokami A, Gotoh A, Yamada H, Keller ET, Matsumoto T. 2000. Tumor Necrosis Factor-α represses androgen sensitivity in the LNCaP prostate cancer cell line. *J Urology* 164:800–805. doi:10.1097/00005392-200009010-00053

Morel KL, Sheahan AV, Burkhart DL, Baca SC, Boufaied N, Liu Y, Qiu X, Cañadas I, Roehle K, Heckler M, Calagua C, Ye H, Pantelidou C, Galbo P, Panja S, Mitrofanova A, Wilkinson S, Whitlock NC, Trostel SY, Hamid AA, Kibel AS, Barbie DA, Choudhury AD, Pomerantz MM, Sweeney CJ, Long HW, Einstein DJ, Shapiro GI, Dougan SK, Sowalsky AG, He HH, Freedman ML, Balk SP, Loda M, Labbé DP, Olson BM, Ellis L. 2021. EZH2 inhibition activates a dsRNA–STING–interferon stress axis that potentiates response to PD-1 checkpoint blockade in prostate cancer. *Nat Cancer* 2:444–456. doi:10.1038/s43018-021-00185-w

Mortarini R, Piris A, Maurichi A, Molla A, Bersani I, Bono A, Bartoli C, Santinami M, Lombardo C, Ravagnani F, Cascinelli N, Parmiani G, Anichini A. 2003. Lack of terminally differentiated tumor-specific CD8+ T cells at tumor site in spite of antitumor immunity to self-antigens in human metastatic melanoma. *Cancer Res* 63:2535–45.

Mukaida N, Sasaki S, Baba T. 2014. Chemokines in Cancer Development and Progression and Their Potential as Targeting Molecules for Cancer Treatment. *Mediat Inflamm* 2014:170381. doi:10.1155/2014/170381

Network TCGAR, Abeshouse A, Ahn J, Akbani R, Ally A, Amin S, Andry CD, Annala M, Aprikian A, Armenia J, Arora A, Auman JT, Balasundaram M, Balu S, Barbieri CE, Bauer T, Benz CC, Bergeron A, Beroukhim R, Berrios M, Bivol A, Bodenheimer T, Boice L, Bootwalla MS, Reis RB dos, Boutros PC, Bowen J, Bowlby R, Boyd J, Bradley RK, Breggia A, Brimo F, Bristow CA, Brooks D, Broom BM, Bryce AH, Bubley G, Burks E, Butterfield YSN, Button M, Canes D, Carlotti CG, Carlsen R, Carmel M, Carroll PR, Carter SL, Cartun R, Carver BS, Chan JM, Chang MT, Chen Y, Cherniack AD, Chevalier S, Chin L, Cho J, Chu A, Chuah E, Chudamani S, Cibulskis K, Ciriello G, Clarke A, Cooperberg MR, Corcoran NM, Costello AJ, Cowan J, Crain D, Curley E, David K, Demchok JA, Demichelis F, Dhalla N, Dhir R, Doueik A, Drake B, Dvinge H, Dyakova N, Felau I, Ferguson ML, Frazer S, Freedland S, Fu Y, Gabriel SB, Gao J, Gardner J, Gastier-Foster JM, Gehlenborg N, Gerken M, Gerstein MB, Getz G, Godwin AK, Gopalan A, Graefen M, Graim K, Gribbin T, Guin R, Gupta M, Hadjipanayis A, Haider S, Hamel L, Hayes DN, Heiman DI, Hess J, Hoadley KA, Holbrook AH, Holt RA, Holway A, Hovens CM, Hoyle AP, Huang M, Hutter CM, Ittmann M, Iype L, Jefferys SR, Jones CD, Jones SJM, Juhl H, Kahles A, Kane CJ, Kasaian K, Kerger M, Khurana E, Kim J, Klein RJ, Kucherlapati R, Lacombe L, Ladanyi M, Lai PH, Laird PW, Lander ES, Latour M, Lawrence MS, Lau K, LeBien T, Lee D, Lee S, Lehmann K-V, Leraas KM, Leshchiner I, Leung R, Libertino JA, Lichtenberg TM, Lin P, Linehan WM, Ling S, Lippman SM, Liu J, Liu W, Lochovsky L, Loda M, Logothetis C, Lolla L, Longacre T, Lu Y, Luo J, Ma Y, Mahadeshwar HS, Mallery D, Mariamidze A, Marra MA, Mayo M, McCall S, McKercher G, Meng S, Mes-Masson A-M, Merino MJ, Meyerson M, Mieczkowski PA, Mills GB, Shaw KRM, Minner S, Moinzadeh A, Moore RA, Morris S, Morrison C, Mose LE, Mungall AJ, Murray BA, Myers JB, Naresh R, Nelson J, Nelson MA, Nelson PS, Newton Y, Noble MS, Noushmehr H, Nykter M, Pantazi A, Parfenov M, Park PJ, Parker JS, Paulauskis J, Penny R, Perou CM, Piché A, Pihl T, Pinto PA, Prandi D, Protopopov A, Ramirez NC, Rao A,

Rathmell WK, Rätsch G, Ren X, Reuter VE, Reynolds SM, Rhie SK, Rieger-Christ K, Roach J, Robertson AG, Robinson B, Rubin MA, Saad F, Sadeghi S, Saksena G, Saller C, Salner A, Sanchez-Vega F, Sander C, Sandusky G, Sauter G, Sboner A, Scardino PT, Scarlata E, Schein JE, Schlomm T, Schmidt LS, Schultz N, Schumacher SE, Seidman J, Neder L, Seth S, Sharp A, Shelton C, Shelton T, Shen H, Shen R, Sherman M, Sheth M, Shi Y, Shih J, Shmulevich I, Simko J, Simon R, Simons JV, Sipahimalani P, Skelly T, Sofia HJ, Soloway MG, Song X, Sorcini A, Sougnez C, Stepa S, Stewart C, Stewart J, Stuart JM, Sullivan TB, Sun C, Sun H, Tam A, Tan D, Tang J, Tarnuzzer R, Tarvin K, Taylor BS, Teebagy P, Tenggara I, Têtu B, Tewari A, Thiessen N, Thompson T, Thorne LB, Tirapelli DP, Tomlins SA, Trevisan FA, Troncoso P, True LD, Tsourlakis MC, Tyekucheva S, Allen EV, Berg DJVD, Veluvolu U, Verhaak R, Vocke CD, Voet D, Wan Y, Wang Q, Wang W, Wang Z, Weinhold N, Weinstein JN, Weisenberger DJ, Wilkerson MD, Wise L, Witte J, Wu C-C, Wu J, Wu Y, Xu AW, Yadav SS, Yang Liming, Yang Lixing, Yau C, Ye H, Yena P, Zeng T, Zenklusen JC, Zhang H, Zhang Jianhua, Zhang Jiashan, Zhang W, Zhong Y, Zhu K, Zmuda E. 2015. The Molecular Taxonomy of Primary Prostate Cancer. *Cell* 163:1011–1025. doi:10.1016/j.cell.2015.10.025

Ninomiya S, Kawahara T, Iwashita H, Iwamoto G, Takamoto D, Mochizuki T, Kuroda S, Takeshima T, Izumi K, Teranishi J, Yumura Y, Miyoshi Y, Asai T, Uemura H. 2018. Prostate Basal Cell Carcinoma: A Case Report. *Case Reports Oncol* 11:138–142. doi:10.1159/000487389

Nostrand ELV, Freese P, Pratt GA, Wang X, Wei X, Xiao R, Blue SM, Chen J-Y, Cody NAL, Dominguez D, Olson S, Sundararaman B, Zhan L, Bazile C, Bouvrette LPB, Bergalet J, Duff MO, Garcia KE, Gelboin-Burkhart C, Hochman M, Lambert NJ, Li H, McGurk MP, Nguyen TB, Palden T, Rabano I, Sathe S, Stanton R, Su A, Wang R, Yee BA, Zhou B, Louie AL, Aigner S, Fu X-D, Lécuyer E, Burge CB, Graveley BR, Yeo GW. 2020. A large-scale binding and functional map of human RNA-binding proteins. *Nature* 583:711–719. doi:10.1038/s41586-020-2077-3

Oliveira DSM, Dzinic S, Bonfil AI, Saliganan AD, Sheng S, Bonfil RD. 2015. The mouse prostate: a basic anatomical and histological guideline. *Bosnian J Basic Med* 16:8–13. doi:10.17305/bjbms.2016.917

Ozga AJ, Chow MT, Luster AD. 2021. Chemokines and the immune response to cancer. *Immunity* 54:859–874. doi:10.1016/j.immuni.2021.01.012

Patrawala L, Calhoun T, Schneider-Broussard R, Li H, Bhatia B, Tang S, Reilly JG, Chandra D, Zhou J, Claypool K, Coghlan L, Tang DG. 2006. Highly purified CD44+ prostate cancer cells from xenograft human tumors are enriched in tumorigenic and metastatic progenitor cells. *Oncogene* 25:1696–1708. doi:10.1038/sj.onc.1209327

Peter D, Igreja C, Weber R, Wohlbold L, Weiler C, Ebertsch L, Weichenrieder O, Izaurralde E. 2015. Molecular Architecture of 4E-BP Translational Inhibitors Bound to eIF4E. *Mol Cell* 57:1074–1087. doi:10.1016/j.molcel.2015.01.017

Pollard KS, Hubisz MJ, Rosenbloom KR, Siepel A. 2010. Detection of nonneutral substitution rates on mammalian phylogenies. *Genome Res* 20:110–121. doi:10.1101/gr.097857.109

Polychronopoulos D, King JWD, Nash AJ, Tan G, Lenhard B. 2017. Conserved non-coding elements: developmental gene regulation meets genome organization. *Nucleic Acids Res* 45:gkx1074-. doi:10.1093/nar/gkx1074

Potosky AL, Miller BA, Albertsen PC, Kramer BS. 1995. The Role of Increasing Detection in the Rising Incidence of Prostate Cancer. *JAMA* 7:548–552. doi:10.1001/jama.1995.03520310046028

Puca L, Vlachostergios PJ, Beltran H. 2018. Neuroendocrine Differentiation in Prostate Cancer: Emerging Biology, Models, and Therapies. *Csh Perspect Med* 9:a030593. doi:10.1101/cshperspect.a030593

Qiu X, Mao Q, Tang Y, Wang L, Chawla R, Pliner HA, Trapnell C. 2017. Reversed graph embedding resolves complex single-cell trajectories. *Nat Methods* 14:979–982. doi:10.1038/nmeth.4402

Quaglia F, Krishn SR, Wang Y, Goodrich DW, McCue P, Kossenkov AV, Mandigo AC, Knudsen KE, Weinreb PH, Corey E, Kelly WK, Languino LR. 2021. Differential expression of αVβ3 and αVβ6 integrins in prostate cancer progression. *PLoS ONE*. doi:10.1371/journal.pone.0244985

Ray D, Kazan H, Cook KB, Weirauch MT, Najafabadi HS, Li X, Gueroussov S, Albu M, Zheng H, Yang A, Na H, Irimia M, Matzat LH, Dale RK, Smith SA, Yarosh CA, Kelly SM, Nabet B, Mecenas D, Li W, Laishram RS, Qiao M, Lipshitz HD, Piano F, Corbett AH, Carstens RP, Frey BJ, Anderson RA, Lynch KW, Penalva LOF, Lei EP, Fraser AG, Blencowe BJ, Morris QD, Hughes TR. 2013. A compendium of RNA-binding motifs for decoding gene regulation. *Nature* 499:172–177. doi:10.1038/nature12311

Rizvi NA, Hellmann MD, Snyder A, Kvistborg P, Makarov V, Havel JJ, Lee W, Yuan J, Wong P, Ho TS, Miller ML, Rekhtman N, Moreira AL, Ibrahim F, Bruggeman C, Gasmi B, Zappasodi R, Maeda Y, Sander C, Garon EB, Merghoub T, Wolchok edd D, Schumacher TN, Chan TA. 2015. Mutational landscape determines sensitivity to PD-1 blockade in non–small cell lung cancer. *Science* 348:124–128.

Sala LS, Boutillon F, Menara G, Goyon-Pélard AD, Leprévost M, Codzamanian J, Lister N, Pencik J, Clark A, Cagnard N, Bole-Feysot C, Moriggl R, Risbridger GP, Taylor RA, Kenner L, Guidotti J, Goffin V. 2017a. A rare castration-resistant progenitor cell population is highly enriched in Pten-null prostate tumours. *J Pathology* 243:51–64. doi:10.1002/path.4924

Sala LS, Boutillon F, Menara G, Goyon-Pélard AD, Leprévost M, Codzamanian J, Lister N, Pencik J, Clark A, Cagnard N, Bole-Feysot C, Moriggl R, Risbridger GP, Taylor RA, Kenner L, Guidotti J, Goffin V. 2017b. A rare castration-resistant progenitor cell population is highly enriched in Pten-null prostate tumours. *J Pathology* 243:51–64. doi:10.1002/path.4924

Salido M, Vilches J, López A. 2000. Neuropeptides bombesin and calcitonin induce resistance to etoposide induced apoptosis in prostate cancer cell lines. *Histol Histopathol* 15:729–38. doi:10.14670/hh-15.729

Salomon B, Bluestone JA. 2001. Complexities of CD28/B7: CTLA-4 Costimulatory Pathways in Autoimmunity and Transplantation. *Annual Review of Immunology* 225–252.

Schuster SL, Hsieh AC. 2019. The Untranslated Regions of mRNAs in Cancer. *Trends Cancer* 5:245–262. doi:10.1016/j.trecan.2019.02.011

Setty M, Kiseliovas V, Levine J, Gayoso A, Mazutis L, Pe'er D. 2019. Characterization of cell fate probabilities in single-cell data with Palantir. *Nat Biotechnol* 37:451–460. doi:10.1038/s41587-019-0068-4

Sévigny M, Julien IB, Venkatasubramani JP, Hui JB, Dutchak PA, Sephton CF. 2020. FUS contributes to mTOR-dependent inhibition of translation. *J Biol Chem* 295:18459–18473. doi:10.1074/jbc.ra120.013801

Sha K, Yeh S, Chang C, Nastiuk KL, Krolewski JJ. 2015. TNF signaling mediates an enzalutamide-induced metastatic phenotype of prostate cancer and microenvironment cell co-cultures. *Oncotarget* 6:25726–25740. doi:10.18632/oncotarget.4535

Shen MM, Abate-Shen C. 2010. Molecular genetics of prostate cancer: new prospects for old challenges. *Gene Dev* 24:1967–2000. doi:10.1101/gad.1965810

Shi Z, Fujii K, Kovary KM, Genuth NR, Röst HL, Teruel MN, Barna M. 2017. Heterogeneous Ribosomes Preferentially Translate Distinct Subpools of mRNAs Genome-wide. *Mol Cell* 67:71-83.e7. doi:10.1016/j.molcel.2017.05.021

Shibuya K, Homma S, Yoshida T, Ohno Y, Ichikawa N, Kawamura H, Imamoto T, Matsuno Y, Taketomi A. 2018. Carcinoma in the residual rectum of a long-standing Crohn's disease patient following subtotal colectomy: A case report. *Mol Clin Oncol* 9:50–53. doi:10.3892/mco.2018.1626

Siegel RL, Miller KD, Fuchs HE, Jemal A. 2021. Cancer Statistics, 2021. *Ca Cancer J Clin* 71:7–33. doi:10.3322/caac.21654

Siepel A, Bejerano G, Pedersen JS, Hinrichs AS, Hou M, Rosenbloom K, Clawson H, Spieth J, Hillier LW, Richards S, Weinstock GM, Wilson RK, Gibbs RA, Kent WJ, Miller W, Haussler D. 2005. Evolutionarily conserved elements in vertebrate, insect, worm, and yeast genomes. *Genome Res* 15:1034–1050. doi:10.1101/gr.3715005

Silvera D, Formenti SC, Schneider RJ. 2010. Translational control in cancer. *Nat Rev Cancer* 10:254–266. doi:10.1038/nrc2824

Simon RA, Sant'Agnese PA di, Huang L-S, Xu H, Yao JL, Yang Q, Liang S, Liu J, Yu R, Cheng L, Oh WK, Palapattu GS, Wei J, Huang J. 2009. CD44 expression is a feature of prostatic small cell Carcinoma and Distinguishes it from its Mimickers. *Hum Pathol* 40:252–258. doi:10.1016/j.humpath.2008.07.014

Smith RCL, Kanellos G, Vlahov N, Alexandrou C, Willis AE, Knight JRP, Sansom OJ. 2021. Translation initiation in cancer at a glance. *J Cell Sci* 134:jcs248476. doi:10.1242/jcs.248476

Song H, Weinstein HNW, Allegakoen P, Wadsworth MH, Xie J, Yang H, Castro EA, Lu KL, Stohr BA, Feng FY, Carroll PR, Wang B, Cooperberg MR, Shalek AK, Huang FW. 2022. Single-cell analysis of human primary prostate cancer reveals the heterogeneity of tumor-associated epithelial cell states. *Nat Commun* 13:141. doi:10.1038/s41467-021-27322-4

Song P, Yang F, Jin H, Wang X. 2021. The regulation of protein translation and its implications for cancer. *Signal Transduct Target Ther* 6:68. doi:10.1038/s41392-020-00444-9

Stephen HF, J. OS, F. MD, W. WR, A. SJ, B. HJ, Rene G, Caroline R, Dirk S, C. HJ, Wallace A, J.M. van den EA, Jose L, Paul L, M. VJ, P. LG, David H, H. OC, Celeste L, Christian P, Ian Q, I. CJ, D. WJ, S. WJ, Jason T, J. YM, M. NG, Axel H, J. UW. 2010. Improved Survival with Ipilimumab in Patients with Metastatic Melanoma. *New Engl J Med* 363:711–723. doi:10.1056/nejmoa1003466

Stultz J, Fong L. 2021. How to turn up the heat on the cold immune microenvironment of metastatic prostate cancer. *Prostate Cancer P D* 24:697–717. doi:10.1038/s41391-021-00340-5

Svensson RU, Haverkamp JM, Thedens DR, Cohen MB, Ratliff TL, Henry MD. 2011. Slow Disease Progression in a C57BL/6 Pten-Deficient Mouse Model of Prostate Cancer. *Am J Pathology* 179:502–512. doi:10.1016/j.ajpath.2011.03.014

Tahmasebi S, Khoutorsky A, Mathews MB, Sonenberg N. 2018. Translation deregulation in human disease. *Nat Rev Mol Cell Bio* 19:791–807. doi:10.1038/s41580-018-0034-x

Taylor BS, Schultz N, Hieronymus H, Gopalan A, Xiao Y, Carver BS, Arora 4 Vivek K., Kaushik 2 Poorvi, Cerami 1 Ethan, Reva 1 Boris, Antipin 1 Yevgeniy, Mitsiades 1 Nicholas, Landers 5 Thomas, Dolgalev 2 Igor, Major 2 John E., Wilson 6 Manda, Socci 6 Nicholas D., Lash 6 Alex E., Heguy 6 Adriana, Eastham 2 James A., Scher 4 Howard I., Reuter 5 Victor E., Scardino 3 Peter T., Sander 4 Chris, Sawyers 1 Charles L., Gerald WL. 2010. Integrative Genomic Profiling of Human Prostate Cancer. *Cancer Cell* 11–22. doi:10.1016/j.ccr.2010.05.026

Torrent M, Chalancon G, Groot NS de, Wuster A, Babu MM. 2018. Cells alter their tRNA abundance to selectively regulate protein synthesis during stress conditions. *Sci Signal* 11:eaat6409. doi:10.1126/scisignal.aat6409

Trapnell C, Cacchiarelli D, Grimsby J, Pokharel P, Li S, Morse M, Lennon NJ, Livak KJ, Mikkelsen TS, Rinn JL. 2014. Pseudo-temporal ordering of individual cells reveals dynamics and regulators of cell fate decisions. *Nat Biotechnol* 32:381–386. doi:10.1038/nbt.2859

Turner EE, Cox TC. 2014. Genetic evidence for conserved non-coding element function across species–the ears have it. *Front Physiol* 5:7. doi:10.3389/fphys.2014.00007

Uttam S, Wong C, Price TJ, Khoutorsky A. 2018. eIF4E-Dependent Translational Control: A Central Mechanism for Regulation of Pain Plasticity. *Frontiers Genetics* 9:470. doi:10.3389/fgene.2018.00470

Wang S, Gao J, Lei Q, Rozengurt N, Pritchard C, Jiao J, Thomas GV, Li G, Roy-Burman P, Nelson PS, Liu X, Wu H. 2003. Prostate-specific deletion of the murine Pten tumor suppressor gene leads to metastatic prostate cancer. *Cancer Cell* 4:209–221. doi:10.1016/s1535-6108(03)00215-0

Wang S, Garcia AJ, Wu M, Lawson DA, Witte ON, Wu H. 2006. Pten deletion leads to the expansion of a prostatic stem/progenitor cell subpopulation and tumor initiation. *P Natl Acad Sci Usa* 103:1480–1485. doi:10.1073/pnas.0510652103

Wang X-W, Liu C-X, Chen L-L, Zhang QC. 2021. RNA structure probing uncovers RNA structure-dependent biological functions. *Nat Chem Biol* 17:755–766. doi:10.1038/s41589-021-00805-7

Wang ZA, Mitrofanova A, Bergren SK, Abate-Shen C, Cardiff RD, Califano A, Shen MM. 2013. Lineage analysis of basal epithelial cells reveals their unexpected plasticity and supports a cell-of-origin model for prostate cancer heterogeneity. *Nat Cell Biol* 15:274–283. doi:10.1038/ncb2697

Watson PA, Arora VK, Sawyers CL. 2015. Emerging mechanisms of resistance to androgen receptor inhibitors in prostate cancer. *Nat Rev Cancer* 15:701–711. doi:10.1038/nrc4016

Wilkinson KA, Merino EJ, Weeks KM. 2006. Selective 2′-hydroxyl acylation analyzed by primer extension (SHAPE): quantitative RNA structure analysis at single nucleotide resolution. *Nat Protoc* 1:1610–1616. doi:10.1038/nprot.2006.249

Wilkinson S, Ye H, Karzai F, Harmon SA, Terrigino NT, VanderWeele DJ, Bright JR, Atway R, Trostel SY, Carrabba NV, Whitlock NC, Walker SM, Lis RT, Sater HA, Capaldo BJ, Madan RA, Gulley JL, Chun G, Merino MJ, Pinto PA, Salles DC, Kaur HB, Lotan TL, Venzon DJ, Choyke PL, Turkbey B, Dahut WL, Sowalsky AG. 2021. Nascent Prostate Cancer Heterogeneity Drives Evolution and Resistance to Intense Hormonal Therapy. *Eur Urol* 80:746–757. doi:10.1016/j.eururo.2021.03.009

Wolfe AL, Singh K, Zhong Y, Drewe P, Rajasekhar VK, Sanghvi VR, Mavrakis KJ, Jiang M, Roderick JE, Meulen JV der, Schatz JH, Rodrigo CM, Zhao C, Rondou P, Stanchina E de, Teruya-Feldstein J, Kelliher MA, Speleman F, Porco JA, Pelletier J, Rätsch G, Wendel H-G. 2014. RNA G-quadruplexes cause eIF4A-dependent oncogene translation in cancer. *Nature* 513:65–70. doi:10.1038/nature13485

Xin L, Lawson DA, Witte ON. 2005. The Sca-1 cell surface marker enriches for a prostate-regenerating cell subpopulation that can initiate prostate tumorigenesis. *PNAS* 102:6942–6947. doi:10.1073/pnas.0502320102

Xiong Y, Yuan L, Chen S, Xu H, Peng T, Ju L, Wang G, Xiao Y, Wang X. 2020. WFDC2 suppresses prostate cancer metastasis by modulating EGFR signaling inactivation. *Cell Death Dis* 11:537. doi:10.1038/s41419-020-02752-y

Yasuda K, Zhang H, Loiselle D, Haystead T, Macara IG, Mili S. 2013. The RNA-binding protein Fus directs translation of localized mRNAs in APC-RNP granules. *J Cell Biol* 203:737–746. doi:10.1083/jcb.201306058

Zaynagetdinov R, Sherrill TP, Polosukhin VV, Han W, Ausborn JA, McLoed AG, McMahon FB, Gleaves LA, Degryse AL, Stathopoulos GT, Yull FE, Blackwell TS. 2011. A Critical Role for Macrophages in Promotion of Urethane-Induced Lung Carcinogenesis. *J Immunol* 187:5703–5711. doi:10.4049/jimmunol.1100558

Zou W, Wolchok JD, Chen L. 2016. PD-L1 (B7-H1) and PD-1 pathway blockade for cancer therapy: Mechanisms, response biomarkers, and combinations. *STM* 8.